# Investigating Ultrafast Light-Matter Interactions via Dual-Comb Raman Spectroscopy and Electron Diffraction of Nanophotonic Waveforms

Kathrin Juliane Mohler

München, 2021

# Investigating Ultrafast Light-Matter Interactions via Dual-Comb Raman Spectroscopy and Electron Diffraction of Nanophotonic Waveforms

## Dissertation

zur Erlangung des Doktorgrades der Naturwissenschaften (Dr. rer. nat.)


an der Fakultät für Physik

der Ludwig-Maximilians-Universität München

vorgelegt von

Kathrin Juliane Mohler

aus Augsburg

München, den 15.Juni 2021

| | |
|---|---|
| Erstgutachter: | Prof. Dr. Ferenc Krausz |
| Zweitgutachter: | Prof. Dr. Thomas Udem |
| Tag der mündlichen Prüfung: | 14.Oktober 2021 |

*dedicated to my friends and family*

# Publications and Conference Contributions

## Scientific Publications Related to This Thesis

**K. J. Mohler**, D. Ehberger, I. Gronwald, C. Lange, R. Huber, and P. Baum. Ultrafast electron diffraction from nanophotonic waveforms via dynamical Aharonov-Bohm phases. *Science Advances*, 6: eabc8804, 2020.

**K. J. Mohler**, and P. Baum. Ultrafast electron diffraction of THz-excited nanostructures. *EPJ Web Conf.*, 205: 08004, 2019.

D. Ehberger, **K. J. Mohler**, T. Vasileiadis, R. Ernstorfer, L. Waldecker, and P. Baum. Terahertz compression of electron pulses at a planar mirror membrane. *Phys. Rev. Appl.*, 11: 024034, 2019.

**K. J. Mohler**, B. J. Bohn, M. Yan, G. Mélen, T. W. Hänsch, and N. Picqué. Dual-comb coherent Raman spectroscopy with lasers of 1-GHz pulse repetition frequency. *Opt. Lett.*, 42: 318-321, 2017.

## Additional Scientific Publications

J. Märtz, J. P. Kolb, T. Klein, **K. J. Mohler**, M. Eibl, W. Wieser, R. Huber, S. Priglinger, and A. Wolf. Combined in-depth, 3D, en face imaging of the optic disc, optic disc pits and optic disc pit maculopathy using swept-source megahertz OCT at 1050 nm. *Graefe's Archive for Clinical and Experimental Ophthalmology*, 256: 289–298, 2018.

J. Märtz, **K. J. Mohler**, J. P. Kolb, T. Klein, A. Neubauer, A. Kampik, S. Priglinger, W. Wieser, R. Huber, and A. Wolf. Intrapapillary proliferation in optic disk pits: Clinical findings and time-related changes. *Retina*, 37: 906-914, 2017.

M. Adhi, D. Ferrara, R. F. Mullins, C. R. Baumal, **K. J. Mohler**, M. F. Kraus, J. Liu, E. Badaro, T. Alasil, J. Hornegger, J. G. Fujimoto, J. S. Duker, and N. K. Waheed. Characterization of choroidal layers in normal aging eyes using enface swept-source optical coherence tomography, *PLoS ONE*, 10: e0133080, 2015.

**K. J. Mohler**, W. Draxinger, T. Klein, J. P. Kolb, W. Wieser, C. Haritoglou, A. Kampik, J. G. Fujimoto, A. S. Neubauer, R. Huber, and A. Wolf. Combined 60° wide-field choroidal thickness maps and high-definition en face vasculature visualization using swept-source megahertz OCT at 1050 nm. *Invest. Ophthalmol. Vis. Sci.*, 56: 6284-6293, 2015.

L. Reznicek, J. P. Kolb, T. Klein, **K. J. Mohler**, W. Wieser, R. Huber, M. Kernt, J. Märtz, and A. S. Neubauer. Wide-field megahertz OCT imaging of patients with diabetic retinopathy. *Journal of Diabetes Research*, 2015: 305084, 2015.

D. Ferrara, **K. J. Mohler**, N. Waheed, M. Adhi, J. J. Liu, I. Grulkowski, M. F. Kraus, C. Baumal, J. Hornegger, J. G. Fujimoto, and J. S. Duker. En face enhanced-depth swept-source optical coherence tomography features of chronic central serous chorioretinopathy. *Ophthalmology*, 121: 719-26, 2014.

M. Adhi, J. J. Liu, A. H. Qavi, I. Grulkowski, C. D. Lu, **K. J. Mohler**, D. Ferrara, M. F. Kraus, C. R. Baumal, A. J. Witkin, N. K. Waheed, J. Hornegger, J. G. Fujimoto, and J. S. Duker. Choroidal analysis in healthy eyes using swept-source optical coherence tomography compared to spectral domain optical coherence tomography, *American Journal of Ophthalmology*, 157: 1272-1281, 2014.

W. J. Choi, **K. J. Mohler**, B. Potsaid, C. D. Lu, J. J. Liu, V. Jayaraman, A. E. Cable, J. S. Duker, R. Huber, and J. G. Fujimoto. Choriocapillaris and choroidal microvasculature imaging with ultrahigh speed OCT angiography. *PLoS ONE*, 8: e81499, 2013.

## Conference Contributions and Workshop Participation as First Author

*XXI International Conference on Ultrafast Phenomena* (Talk)
Hamburg, Germany, July 2018.

*Nano and Ultrafast Surface Sciences (NUSS) workshop* (Poster)
Munich, Germany, September 2019.

*Annual Meeting of the Association for Research in Vision and Ophthalmology (ARVO)* (Poster)
Seattle, USA, May 2013.

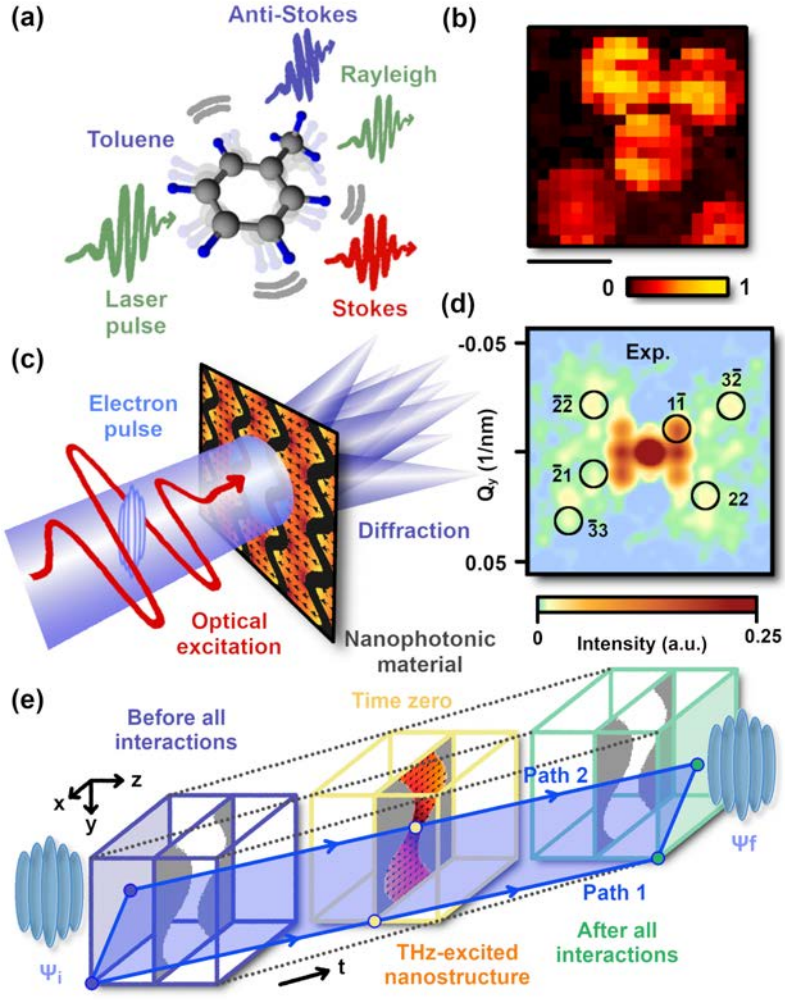


**Figure 1: Ultrafast light-matter interactions as investigated in this thesis.** **(a)** Elastic Rayleigh scattering and inelastic Raman scattering revealing laser-excited molecular vibrations. **(b)** Dual-comb Raman microscopy of microscale polystyrene beads. Scale bar equals 75 µm. **(c)** Electron diffraction as distortion-free probing technique for optically-excited nanophotonic materials. **(d)** Small-angle static electron diffraction of wavy nanostructures as obtained with femtosecond electron pulses. **(e)** Theoretical framework, based on space-time integration of electromagnetic potentials, for the prediction and interpretation of experimental results, which are obtained via ultrafast electron diffraction of optically-excited nanostructures. $\Psi_i$ and $\Psi_f$ represent the electron wave function before and after the interaction with the optically-initiated dynamics within the sample, respectively.

# Zusammenfassung

Ultraschnelle Phänomene, welche durch die Wechselwirkung von Licht mit den kleinen Bausteinen der Materie wie Elektronen, Atomen oder Molekülen entstehen, gehören zu den grundlegendsten Prozessen in der Natur. Daher sind optische Verfahren beispielsweise auch in der Lage, die chemische Zusammensetzung komplexer Materialien zu bestimmen, indem die spezifischen elektronischen Zustände oder Schwingungsmoden der Proben mittels optischer Anregung gezielt abgefragt werden. Neben den natürlich vorkommenden Phänomenen können neuartige optische Effekte wie negative Brechungsindizes über sogenannte Metamaterialien generiert werden. Diese künstlich designten Materialien erhalten ihre exotischen Eigenschaften durch eine ausgefeilte Strukturierung auf Längenskalen unterhalb der Wellenlänge des Anregungslichtes, weshalb deren detailgenaue Charakterisierung nur mittels hochauflösender Bildgebungstechniken erfolgen kann. All diese lichtinduzierten Prozesse eint dabei das Zusammenspiel von schnell oszillierenden elektromagnetischen Feldern und ultraschnellen primären Bewegungen von Atomen oder Elektronen, die typischerweise innerhalb von Femtosekunden oder schneller ablaufen. Die Detektion solch ultraschneller Prozesse mit genügend hoher Auflösung in Raum und Zeit bleibt eine große Herausforderung und daher weiterhin ein Gebiet aktiver Forschung.

Unter der übergeordneten Zielsetzung der **Entwicklung neuartiger Technologien zur Analyse von Licht-Materie-Wechselwirkungen** mit hoher Präzision in Raum und Zeit untersuchen die Schlüsselfragen der Hauptkapitel dieser Arbeit daher: (1) wie optische Frequenzkämme in der Raman-Spektroskopie die chemische Zusammensetzung einer Probe über die gezielte Anregung molekularer Schwingungen bestimmen, (2) wie Elektronenpulse in Folge der Interaktion mit Lichtzyklen für ultraschnelle Beugungsexperimente zeitlich komprimiert werden, (3) wie in nanophotonischen Materialien sowohl die Gestalt als auch die periodische Anordnung der nanoskaligen Bausteine mittels Elektronenbeugung analysiert werden können, (4) wie metallische Nanostrukturen durch ihre feine Strukturierung ein hohes Maß an Kontrolle über elektromagnetische Wellen bieten, welche durch ultraschnelle Elektronenbeugung charakterisiert werden kann, und (5) wie sich, auf Sub-Zyklen-Zeitskalen, die optisch induzierte Dynamik innerhalb der Einheitszellen der Proben als zeitabhängige Veränderungen in der ultraschnellen Elektronenbeugung manifestiert.

Die Anregungs-Abfrage-Experimente zur Untersuchung dieser Fragestellungen liefern dabei jeweils Serien an charakteristischen Momentaufnahmen von zeitlich eingefrorenen Zwischenzuständen optisch angeregter Proben. Diese Momentaufnahmen resultieren aus der zeitlich verzögerten Wechselwirkung der Probe mit wahlweise optischen Abfragepulsen oder Elektronenpulsen mit Dauern im Femtosekundenbereich. Aufgrund ihrer Ruhemasse und der damit verbundenen kurzen de Broglie Wellenlänge bieten Elektronen eine besonders gute räumliche Auflösung, wobei deren Elementarladung zudem als Sensor für elektromagnetische Felder und Potentiale fungieren kann. Die Erweiterung des Anwendungsspektrums von Anregungs-Abfrage-Experimenten durch die Verwendung von Abfragepulsen unterschiedlicher Art wird in dieser Arbeit anhand der Gegenüberstellung von rein optischer Raman-Spektroskopie und Elektronenbeugung an nanophotonischen Wellenformen illustriert.

Zunächst wurden in einem rein optischen Anregungs-Abfrage-Experiment zwei synchronisierte Frequenzkämme für breitbandige und hochaufgelöste spektroskopische Messungen eingesetzt. Als leistungsstarke, gepulste Lichtquellen mit hohen Spitzenintensitäten erhöhen die Frequenzkämme dabei die Effizienz des nichtlinearen Prozesses der kohärenten anti-Stokes Raman-Streuung (CARS):

**(1) CARS-Spektroskopie**: Die Technik der Raman-Spektroskopie mittels zweier Frequenzkämme wurde auf Repetitionsraten der Pulse von 1 GHz erweitert, was die serielle Aufnahme von breitbandigen und hochaufgelösten CARS-Spektren mit hohen Aktualisierungsraten im Bereich weniger kHz erlaubt.

**(2) CARS-Mikroskopie:** Der Anwendungsbereich von CARS mit zwei Frequenzkämmen wurde von Flüssigphasenspektroskopie auf die hyperspektrale Raman-Bildgebung von Feststoffen ausgeweitet.

Zudem werden in dieser Arbeit, im Hinblick auf geplante Experimente zur zeitaufgelösten Elektronenbildgebung und -beugung, die maßgeblich notwendigen Techniken zur Charakterisierung und zeitlichen Komprimierung der Elektronenpulse auf Dauern von unter 100 fs vorgestellt und erfolgreich angewendet. Die gemeinsame Basis dieser Techniken bilden dabei maßgeschneiderte Wechselwirkungen zwischen Elektronenpulsen und dem Sub-Zyklus synchronisierter Terahertzstrahlung, welche wahlweise durch Metallfolien oder mikroskopische Resonatoren ermöglicht werden:

**(3) Terahertzkomprimierte Elektronenpulse:** Unsere Elektronenpulse mit Dauern von unter 100 fs und einer zeitlichen Stabilität im Bereich einiger Femtosekunden bieten eine klare Perspektive für die Untersuchung von Licht-Materie-Wechselwirkungen mittels ultraschneller Elektronenbeugung.

Insbesondere wurden durch Terahertzstrahlung zeitkomprimierte Einzelelektronenpulse als geeignete Sensoren für die nichtinvasive Untersuchung optisch angeregter, nanostrukturierter Materialien etabliert. In der ultraschnellen Elektronenbeugung tritt diese auf Sub-Zyklen-Zeitskalen induzierte Elektrodynamik als charakteristische Änderungen der zeitaufgelösten Beugungsbilder in Erscheinung. Diese strukturabhängigen Änderungen folgen dabei den Oszillationen der elektromagnetischen Nahfelder und Potentiale und können zu einer vorübergehenden Verletzung der typischen Punktsymmetrie von statischen Beugungsbildern führen. Numerische Simulationen reproduzieren diese experimentellen Ergebnisse und dienen dazu, die beobachtete Verletzung der Punktsymmetrie mit der durch die optische Anregung induzierten Elektrodynamik zu verknüpfen, welche in der Probe zum Zeitpunkt der Interaktion mit den Elektronen vorherrschte. Unser experimentelles und theoretisches Konzept zur Untersuchung nanophotonischer Wellenformen mittels ultraschneller Elektronenbeugung umfasst dabei mehrere interessante Aspekte:

**(4) Ultraschnelle Elektronenbeugung (UED):** Mit den untersuchten elektrodynamischen Effekten der Nanophotonik wurde ein neues Anwendungsgebiet der UED auf Sub-Zyklen-Zeitskalen erschlossen, welches nun Studien von atomaren Bewegungen im Femtosekunden-Bereich ergänzt.

**(5) Nanophotonik:** Die Funktionsweise nanophotonischer Materialien kann nun durch Elektronenbeugung und -holographie auf Grundlage der optischen Zyklen untersucht werden, indem nanoskalige Abtastsonden durch zeitkomprimierte Elektronenpulse ersetzt werden.

**(6) Simulationen:** Die präsentierten vierdimensionalen Raum-Zeit-Phasenintegrale bilden einen einfachen, aber dennoch umfassenden theoretischen Überbau, mit dessen Hilfe eine Vielzahl an elektronenholographischer Effekte vorhergesagt werden können, welche durch die Wechselwirkung von Licht mit nahezu jeglicher Art von Nanostrukturen verursacht werden.

**(7) Quantenmechanik:** Die beobachteten elektroneninterferometrischen Phasenverschiebungen, die mit elektromagnetischen Potentialen im Terahertz-Frequenzbereich assoziiert werden, stellen faszinierende Studien zum Aharonov-Bohm-Effekt in hochdynamischen Systemen mittels terahertzkomprimierter Elektronenpulse in Aussicht.

Somit wird die zeitaufgelöste Elektroneninterferometrie und -mikroskopie in Zukunft eine wertvolle Ergänzung zu optischer Spektroskopie und Mikroskopie darstellen können, um die mikroskopischen, nanoskaligen und atomaren Eigenschaften sowohl natürlicher als auch künstlich designter Materialien samt ihren dynamischen Prozessen umfassend abbilden und analysieren zu können.

# Abstract

Ultrafast phenomena, originating from the interaction of light with the tiny constituents of matter such as electrons, atoms and molecules, represent some of the most fundamental processes occurring in nature. This is the reason why optical methods are, for example, capable of unraveling the chemical composition of complex materials by tuning an optical probe to specific electronic or vibrational transitions of the specimen under investigation. In addition to naturally occurring phenomena, novel optical effects such as negative refractive indices can be generated using so-called metamaterials. These artificially-engineered materials obtain their exotic properties from a sophisticated structuring on length scales below the wavelength of the optical excitation, which renders high-resolution imaging techniques indispensable for investigating the functionality of such metamaterials. Here, the targeted realm of light-induced dynamics in natural and artificial materials is united by the interplay of rapidly-oscillating electromagnetic fields with the primary atomic or electronic motions, typically occurring on femtosecond time scales or even below. Capturing such ultrafast dynamics with sufficiently high resolution in both space and time is far from trivial and therefore remains an area of active research.

Within the overarching objective of developing **novel technologies for analyzing ultrafast light-matter interactions** with high precision in space and time, the key questions addressed in the main chapters of this thesis explore: (1) how optical frequency combs excite molecular vibrations to uncover a sample's chemical composition via Raman spectroscopy, (2) how optical cycles are harnessed to time-compress electron pulses for ultrafast diffractive imaging applications, (3) how small-angle electron diffraction examines the shape and periodic arrangement of the nanoscale building blocks composing nanophotonic materials, (4) how the sub-wavelength-scale architecture of metallic nanostructures execute an advanced level of control on interacting electromagnetic waves, which can be probed via ultrafast electron diffraction, and (5) how optically-induced sub-unit-cell dynamics in nanostructured arrays relate to sub-excitation-cycle Bragg spot dynamics in time-resolved electron diffraction.

The respective pump-probe experiments, applied for these outlined investigations, deliver series of characteristic snapshots capturing time-frozen transient states of the optically-excited samples under examination. These snapshots are generated via the delayed interaction of the sample with either optical or electron probe pulses of femtosecond duration. Resulting from their rest mass and the associated ultrashort de Broglie wavelength, electrons offer particularly high spatial resolution, whereby their elementary charge can additionally serve as a valuable probe for electromagnetic fields and potentials. In this way, probing pulses of different nature enrich the regimes of application of pump-probe experiments, as illustrated in this thesis at the examples of all-optical Raman spectroscopy and electron diffraction of nanophotonic waveforms.

First, two synchronized frequency combs in an all-optical pump-probe scheme are demonstrated to serve as powerful light sources for broadband spectroscopic measurements at highest precision by efficiently driving the nonlinear process involved in coherent anti-Stokes Raman scattering (CARS):

**(1) Dual-comb CARS:** Dual-comb Raman spectroscopy is advanced to laser pulse repetition rates of 1 GHz, yielding broadband and high-precision CARS spectra at high refresh rates in the few kHz-range.

**(2) Dual-comb Raman microscopy:** The application regime of dual-comb CARS is extended from liquid phase spectroscopy to 2D hyperspectral Raman imaging of solid samples.

Next, the decisive techniques for reliably characterizing and time-compressing electron pulses to durations below 100 fs are introduced and successfully applied in this thesis, with special focus on the desired experiments in time-resolved electron imaging and diffraction settings. The common basis of these approaches is represented by the precisely tailored interaction of electron pulses with a sub-cycle of synchronized terahertz radiation, whereby the interactions underlying electron pulse compression and characterization are mediated alternatively by metal foils or microscopic resonators:

**(3) Terahertz-compressed electron pulses:** Our electron pulses of sub-100-fs duration and with a timing stability on the level of a few femtoseconds provide a clear perspective for ultrafast diffraction experiments to study light-matter interactions.

In particular, terahertz-compressed single-electron pulses are established as suitable probes for non-invasively investigating nanostructured materials together with their optical properties. Here, the initiated sub-cycle electromagnetic dynamics become evident in our electron diffraction setting from the observation of structure-specific centrosymmetry-violating Bragg spot dynamics in synchrony to the oscillations of the electromagnetic near fields and potentials. Numerical simulations reproduce our experimental results and serve for linking the observed violation of centrosymmetry back to the excitation-induced electrodynamics, existing in the sample at the time of electron transit. Our experimental and theoretical concept for investigating nanophotonic waveforms via ultrafast electron diffraction addresses several intriguing aspects:

**(4) Ultrafast electron diffraction (UED):** The application regime of UED is advanced from studies of femtosecond atomic motions to investigations of sub-light-cycle electrodynamics.

**(5) Nanophotonics:** The functionality of nanophotonic materials can now be revealed via diffractive imaging and holography on the basis of the optical cycles by replacing nanoscale scanning probes with time-compressed electron pulses at sub-atomic de Broglie wavelength.

**(6) Simulations:** Reported space-time phase integrals in 4D provide a simple yet all-embracing framework for predicting electron-holographic effects of almost any light-nanostructure interaction.

**(7) Quantum mechanics:** The observed electron-interferometric phase shifts, associated with electromagnetic potentials at terahertz (THz) frequencies, illustrate the intriguing prospect of studying the Aharonov-Bohm effect in highly dynamical settings with THz-compressed electron pulses.

Thus, ultrafast electron interferometry and electron microscopy can complement optical spectroscopy and microscopy on their venture towards capturing a conclusive picture of the microscale, nanoscale and atomic world of natural and artificially-designed materials including their characteristic dynamics.

# Table of Contents

# 1 Introduction

*"If a picture is worth a thousand words, then a one-minute video is worth 1.8 million words."*

*– quote by James L. McQuivey*

This quote does not only perfectly describe the spirit of today's society, in which photography and filming have both found their way into the daily routines of so many people, but it also nicely illustrates the on-going motivation and quest of scientists around the world for the development of novel imaging modalities with superior capabilities. By stretching the limits for both spatial resolution and acquisition times, imaging does not only provide scientists with a valuable tool for detailed documentation purposes but it further invokes the capability to visualize structures being too small or to reveal processes occurring on time scales too fast to be captured by bare eye [1–3].

Highly appreciated for their remarkable performance in static high-resolution matter characterization, state-of-the-art instruments for electron microscopy and diffraction can nowadays achieve sub-ångstrom spatial resolution [4, 5]. In addition to the mere structure of matter from macroscopic down to atomic scales, the dynamic behavior of a material regarding interactions and transitions further determines its properties. While stationary physical properties of various materials can often be directly examined, the interplay with electromagnetic radiation represents an indispensable tool for analyzing dynamics in matter, whereby temporal resolutions in the attosecond regime have become accessible in extreme-ultraviolet photonics with intense ultrashort laser pulses [6]. In general, the relevant time scales associated with the most characteristic transformations and pathways of light-matter interactions strongly depend on the explicit processes and systems under investigation. However, the electromagnetic field cycles and the ultrafast primary atomic and electronic motions, occurring on femtosecond and attosecond time scales, constitute a common basis of the rich range of macroscopic dynamics that may evolve on longer time scales [7].

Consequently, the ultimate technique in the wide-ranging arsenal of imaging tools would unite atomic spatial precision as previously demonstrated by electron microscopy and diffraction [4, 5] with the femtosecond or even attosecond time resolution known from optical methods [6]. However, the development of such an imaging modality, merging ultrahigh-resolution imaging with the shortest possible acquisition times, still remains a challenge up to now. For this reason, the following paragraphs briefly outline some of the most promising experimental tools accompanying today's researchers on their journey towards femtosecond or even attosecond high-resolution "photography".

## 1.1 Pump-Probe Approach for Highest Temporal Resolution

As a video consists of a sequence of images, time-resolved measurements for visualizing dynamic processes in matter rely on the acquisition of time-frozen snapshots, capturing specific transient states

of the specimen under investigation [2, 3, 8]. While our human perception is limited to time scales longer than tens of milliseconds [9], optical high-speed cameras can realize acquisition times as short as a few nanoseconds [10]. In light-matter interactions (see Fig. 1.1), however, serving for unraveling and characterizing the properties of various materials through their response to an applied electromagnetic field, the time scales involved with optical frequencies and motions of atoms and electrons are on the order of femtoseconds or even attoseconds [7] and therefore far beyond the realm of direct inquiry by any currently available detectors. For this reason, more sophisticated detection schemes are required. For example, balanced heterodyne detection, as employed in rapid swept-source optical coherence tomography [3] or dual-comb Fourier transform spectroscopy [11], harnesses optical interference while field-resolved infrared spectroscopy additionally relies on electro-optic sampling [12].

A special category of repetitive techniques, which enable ultrafast measurements while dispensing with the need for a detector of equally high acquisition speed, is represented by pump-probe approaches [2, 13–17]. First, the dynamics under investigation are initialized by an ultrafast interaction, the pump pulse, which drives the system out of equilibrium. The impulsively initiated course of the following relaxation dynamics and its transient non-equilibrium states can then be monitored for a selected point in time by the delayed interaction of the sample with a second pulse, the probe pulse, and might manifest itself in a change in intensity, spectrum or polarization. To acquire a distortion-free snapshot of the processes triggered in the specimen, modifications of the dynamics should be avoided by a careful choice of probe pulse while sufficiently short pulse durations ensure to sharply define the time of initialization and to capture the sample's transient states in a time-frozen way [2, 15, 16]. Targeting highly reversible processes, a series of snapshots for various pump-probe time delays can be acquired, whereby the minimum waiting time between consecutive pump-probe cycles is restricted by the relaxation time of the sample back to its original state [18]. The recorded sequence of delay-dependent images can then be concatenated to generate a video of the entire initiated dynamics, whereby it is sometimes beneficial to analyze the observed changes with respect to an appropriate reference measurement instead of providing a complex encompassing characterization of the entire system under investigation [7]. As the key advantage of the pump-probe technique, the achievable time resolution is now ultimately limited only by the durations of the pulses and the precision in controlling the time delay. The shorter the pulses and the more accurate the time synchronization between probe and pump pulses, the higher is the maximum time resolution accessible in a pump-probe measurement.

Advances in laser technology providing ever shorter flashes of light have paved the way for a large diversity of optical pump-probe applications including femtosecond transition-state spectroscopy [13], attosecond transient-absorption spectroscopy [15], time-resolved photoelectron spectroscopy [14], time-resolved multi-terahertz nano-spectroscopy [16] or dual-comb Raman spectroscopy [17]. Representing a nonlinear and broadband spectroscopy technique, dual-comb Raman spectroscopy with two femtosecond laser sources at 1-GHz repetition frequency (see Mohler et al. [19]) was demonstrated in the course of this thesis (see Chapter 2). Its successful implementation unites an ultrafast pump-probe detection scheme with the unique potential of frequency-comb-based precision measurements while the high peak intensity of ultrashort laser pulses is harnessed simultaneously to efficiently drive the four-wave-mixing process involved in coherent anti-Stokes Raman scattering (CARS) [17, 19].

Even though the time synchronization required for successful pump-probe measurements is facilitated for optical laser pulses, certain processes of interest might favor probing pulses of different nature, such as X-rays or electron pulses. While the charged nature of electrons can provide elusive access to certain phenomena not accessible with photons, Coulomb repulsion and vacuum dispersion impose additional challenges for realizing ultrashort pulse durations for electrons [18, 20], rendering the

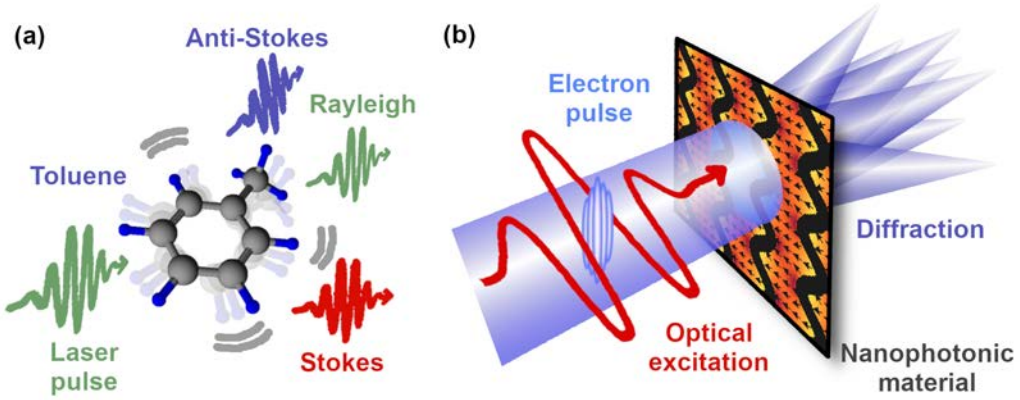


**Figure 1.1: Exemplary ultrafast light-matter interactions.** **(a)** Elastic Rayleigh scattering and inelastic Raman scattering revealing laser-excited molecular vibrations. **(b)** Electron diffraction as probing technique for optically-excited nanophotonic materials.

development of customized techniques for electron pulse compression indispensable. While most X-ray optics are restricted to harnessing compound refractive optics, reflection or diffraction owing to the relatively weak interaction of hard X-rays with matter [21], electron beams can comparatively easily be focused, deflected or even spectrally modified by applied electric and magnetic fields [22, 23].

Previously demonstrated experimental techniques to minimize the duration of electron pulses at the sample's position and thereby to enhance the temporal precision of pump-probe experiments include energy filtering [24], pulse compression with microwave cavities [25], time-stamping [26], optical gating [27] and compression via ponderomotive forces [28, 29]. All-optical electron pulse compression (see Chapter 3) circumvents synchronization issues by relying on a single light source to excite the sample, to trigger the emission of photoelectrons from a gold-coated cathode as well as to optically generate single-cycle terahertz (THz) pulses via optical rectification [30]. The inherently synchronized electron-THz interaction at a bowtie-shaped aperture [31] or a thin metal foil [32] is subsequently harnessed to efficiently time-compress the electron pulses (details in Chapter 3). The recent achievement of isolated few-electron pulses with sub-100-fs pulse durations [25, 31, 32] offers researchers the beneficial choice between optical (see Chapter 2) and electron probe pulses (see Chapter 5) for ultrafast pump-probe measurements in order to maximize the information yield about the optically-induced femtosecond dynamics under investigation.

However, the capability for ultrafast measurements is only half the story on the journey towards high resolution imaging in both space and time. Owing to the large number of particles typically involved in condensed matter or biological systems, an all-embracing spatio-temporal characterization, accounting for the high complexity of the system with all its possible configurations, requires three-dimensional structural information in addition to knowledge about the system's temporal evolution.

## 1.2 Electron Microscopy and Diffraction for Highest Spatial Resolution

Aiming for highest spatial resolution to complement the temporal precision offered by pump-probe measurements, conventional optical microscopy methods sooner or later encounter Abbe's wavelength-dependent limitations dictated by diffraction. In contrast to visible light, X-rays and electrons with moderate kinetic energies in the multi-keV range, by benefiting from their much shorter wavelengths,

provide promising probe pulses for revealing fine details down to the atomic structure of crystals [5,33]. Bridging the resolution gap between conventional light and electron microscopy is the venture of two conceptually different optical nanoscopy approaches [34–36], namely scanning near-field optical microscopy (SNOM) [37] and far-field super-resolution optical microscopy [38–41]. The concept of SNOM [37] merges contrast mechanisms from optical microscopy with the high topographic resolution known from atomic force microscopy (AFM) [42] to surpass the diffraction limit by harnessing the sub-wavelength properties of evanescent waves. The award-winning family of far-field super-resolution optical microscopy techniques, resulting in three Nobel prizes in 2014 for Stefan Hell, Eric Betzig and William Moerner, comprises the following four concepts: (1) Structured illumination microscopy (SIM) [38] extracts a high-resolution image from the moiré fringe pattern obtained under precisely tailored illumination. (2) Stimulated emission depletion microscopy (STED) [39] exploits a dedicated spatial modulation of transitions between two molecular states to confine the region of fluorescence. (3,4) The high resolution of two wide-field techniques for single-molecule localization, called photo-activated localization microscopy (PALM) [40] and stochastic optical reconstruction microscopy (STORM) [41], relies on a series of measurements each probing a different distribution of a small number of stochastically selected and activated fluorophores.

Super-resolution light microscopy can also be combined with electron microscopy in order to capture fluorophore-labeled molecules and sub-cellular, label-free structures alike [43], exploiting two different mechanisms of contrast and equipping researchers with a powerful, versatile and overarching high-resolution imaging modality. Ever since the pioneering days, electron and X-ray diffraction have proven their tremendous potential to unravel the arrangement of atoms and electron density distributions of crystalline structures [44–46]. In tribute to the significance of X-rays for studying lattice structures of condensed matter, three Nobel prizes were awarded to Wilhelm Röntgen, Max von Laue as well as William L. Bragg and his father William H. Bragg for the discovery of X-rays, for the first observation of X-ray diffraction by crystals [47] and for the analysis of crystal structures by means of X-rays [44], respectively. The groundbreaking conception about the wave-like behavior of matter by Louis de Broglie [48] was first experimentally confirmed by Clinton Davisson and Lester Germer via diffraction of electrons at a nickel crystal [45] and independently by George Paget Thomson and Alexander Reid via scattering of cathode rays at thin films [49].

Electron-based and X-ray-based techniques provide complementary insights due to their different nature of interaction with the sample while harnessing similar diffractive imaging techniques for analyzing and interpreting the obtained diffraction patterns. Here, electrons with their approximately six orders of magnitude higher total elastic scattering cross section [50], charged nature and flexible choice of energy-dependent de Broglie wavelength [48] are typically favored for nanoscale sample thicknesses [50, 51], for configurations relying on homogeneous pumping [52], for selected area diffraction [53] or for probing of electric and magnetic field distributions [54]. Equipped with all these sophisticated experimental tools, the final remaining step is now to provide such high resolution in space also at ultrafast acquisition rates and highest precision in time.

## 1.3 High-Resolution Time-Resolved Diffractive Imaging

Despite the wealth of groundbreaking innovations in the wake of this journey towards the ultimate imaging modality, ultrafast high-resolution measurements still remain a balancing act between spatial and temporal precision. Pioneering time-resolved nanoscopy studies accepting this challenge include sub-picosecond terahertz-pulse-induced scanning tunneling microscopy [55], pump-probe terahertz

spectroscopy at a sharp metal tip in a SNOM scheme [16] as well as successful demonstrations of video-rate STED [56] and STORM [57], despite the limited number of valuable frames owing to the detrimental effect of photo bleaching.

The successful incorporation of time resolution into X-ray crystallography via the application of a pump-probe scheme, in order to enable studies of dynamical changes in crystalline structures, strongly relies on the availability of ultrashort and highly brilliant X-ray pulses. Large-scale facilities such as synchrotron radiation sources or free-electron lasers [58] offer a tremendous potential for the generation of such X-ray pulses, but access to this top-level research remains confined to a few facilities worldwide [33]. In contrast, laser-triggered ultrafast electron sources [59, 60], based on the well-known photoelectric effect and moderate electron energy levels of multi-keV, represent table-top systems of reasonable complexity. They easily fit into any laboratory environment, can be equipped with techniques for electron pulse compression to counteract vacuum dispersion (see previous paragraphs as well as Chapter 3) and can in principle provide ultimate spatial resolution due to the ultrashort energy-dependent de Broglie wavelength [48]. For these reasons, the main part of this thesis will focus on electron diffraction and microscopy and the unique capabilities, which the charged nature of electrons can offer for investigating light-matter interactions while dispensing with the need for large-scale facilities, fluorescent molecules or interaction with a nanoscale probe.

The first experimental demonstration of time-resolved electron diffraction with laser-triggered photoelectrons, serving as picosecond pulses for probing a phase transition in a thin aluminum film, was performed by Gérard Mourou and Steve Williamson in 1982 [61]. Over the last decades, their discovery has inspired the development of multiple innovative experimental techniques [2, 62] such as four-dimensional electron microscopy [2], photon-induced near-field electron microscopy (PINEM) [63] or femtosecond electron crystallography [46], which turned electron diffraction and microscopy with laser-generated electron pulses into widespread approaches for studying structural dynamics in molecules and condensed matter. For now, coherent electron-interferometric investigations with electron holography [64, 65], differential phase contrast [64, 65] and atomic picodiffraction [66], however, remain restricted to slower time scales hindering modern electron microscopy and diffraction devices from unleashing the full potential and versatility of their highly coherent electron beams [67].

The concept of ultrafast electron diffraction from optically-excited nanostructures [67], as developed in the course of this thesis (see Chapters 4 to 6), finally marks the advance of time-resolved coherent electron imaging and scattering from studies of atomic motions [46, 68, 69] into the domain of sub-cycle electromagnetism. Here, the advance to the domain of sub-cycle electromagnetism targets the foundations of light-matter interactions in nanophotonic devices or metamaterials in order to characterize their exceptional optical responses [70–72] on the intrinsic time scales, the cycles of light.

## 1.4 Outline of this Thesis

Before discussing this novel experimental and theoretical concept of optically-induced electron nanodiffraction in detail in Chapters 5 and 6, the underlying pump-probe approach for ultrafast measurements is introduced by the optical example of dual-comb Raman spectroscopy (see Chapter 2). Moreover, all-optical electron pulse compression for the generation of sub-100-fs electron pulses is presented (see Chapter 3) and the challenges arising for static electron nanodiffraction with such time-compressed electron pulses, at untypically high electron energies for small-angle electron diffraction [51], are outlined in Chapter 4.

Chapter 2 presents the first successful implementation of broadband pump-probe impulsive Raman spectroscopy via a dual-comb coherent anti-Stokes Raman scattering (CARS) scheme employing two synchronized femtosecond laser sources at around 1-GHz pulse repetition frequency (see Mohler et al. [19]). Addressing the constant quest for ever faster hyper-spectral imaging modalities offering chemical specificity in a non-invasive and label-free manner, the high-resolution broadband coverage of around 1000 $cm^{-1}$ was retained from a previous study at 100 MHz [17] while the ten-fold increase of pulse repetition frequency substantially reduced the waiting period between consecutive spectra by a factor of 20 with the perspective of boosting the acquisition rates even beyond a few kHz. Proof-of-principle investigations of microscale polystyrene beads further evaluate the prospect of extending dual-comb CARS from liquid phase spectroscopy to hyper-spectral microscopy of solid samples.

Chapter 3 explores the potential of all-optically generated and compressed electron pulses for the implementation of ultrafast pump-probe experiments at the high spatial precision which the tiny electron de Broglie wavelength can offer at electron energies of 75 keV. An experimental toolbox for characterizing optical-pump and electron-probe pulses is presented. The interaction of free electrons with single-cycle THz pulses at a thin metal film is harnessed to compensate for dispersion effects and to generate sub-100-fs electron pulses at the sample's position with a timing stability on the level of a few femtoseconds. Reliable electron pulse compression to sub-excitation-cycle durations, as demonstrated in the course of this thesis (see Ehberger et al. [32]), provides a clear perspective for diffraction experiments targeting light-matter interactions on their intrinsic time and length scales.

The characterization of a nanophotonic material's functionality from a fundamental perspective relies on tools to analyze nanoscale electrodynamic near fields in space and time, ideally with sub-wavelength and sub-excitation-cycle precision. Chapter 4 paves the way for time-resolved experimental investigations of optically-excited nanostructures with electron probe pulses by addressing the challenges involved with static electron nanodiffraction at electron energies of 75 keV, where diffraction angles are tiny, the partial coherence of the electron beam imposes substantial constraints on the visibility of the diffraction pattern and the compensation for stray magnetic fields becomes indispensable [67].

Chapter 5, as the heart of this thesis, reports the first application of THz-compressed electron pulses in a pump-probe electron diffraction scheme and establishes electrons as suitable probes for non-invasively revealing electrodynamics in nanophotonic materials, complementing studies using ultrafast scanning probe methods [16,55] or microscale waveform imaging via electron microscopy [54] on their quest for understanding the functionality of complex optical materials on nanometer and femtosecond dimensions. Here, the initiated sub-cycle electromagnetic dynamics in a 2D THz-excited nanostructured array become evident from the observation of centrosymmetry-violating Bragg diffraction in synchrony to the electromagnetic near-field oscillations (see Mohler et al. [67]).

Chapter 6 establishes a theoretical framework for predicting and interpreting the effects experimentally observed with ultrafast electron nanodiffraction. Within this framework (see Mohler et al. [67]), the optically-induced Bragg spot dynamics are attributed to transient phase shifts of the electron de Broglie wave function, originating from the rapidly-oscillating electromagnetic potentials in proximity to the nanostructured material. These results illustrate that electron diffraction equipped with sub-excitation-cycle electron pulses can capture time-resolved snapshots of dynamic electromagnetic potentials, which advances electron diffraction, holography and other coherent imaging techniques from fairly stationary settings to the domain of highly dynamical light-matter interactions [67].

Chapter 7 concludes this thesis by summarizing the main results and providing an outlook on the prospect of the presented techniques for high-resolution imaging in space and time.

# 2

# Dual-Comb Raman Spectroscopy

*"If you want to find the secrets of the universe, think in terms of energy, frequency and vibration."*

*– quote by Nikola Tesla*

The idea of magnifying objects with a set of lenses in an optical microscope has revolutionized our ability to non-invasively visualize and analyze the microscopic world already centuries ago. Nowadays, there exists a whole family of microscopy techniques harnessing different mechanisms of contrast and various imaging schemes [1, 2, 39, 40, 55]. Video-rate imaging has replaced static image acquisition, powerful laser systems serve as coherent broadband light sources, electrons complement photons for ultrahigh resolution imaging applications and molecular spectroscopy is readily incorporated in modern optical microscopy, wherever chemical specificity is needed. A powerful technique often combined with optical microscopy is Raman scattering spectroscopy [1, 73–76], which probes inherent molecular vibrational levels to deliver a spectroscopic fingerprint of the sample, serving for the classification and identification of the different molecules contained in the specimen under investigation.

Molecular species exposed to electromagnetic radiation in the near-infrared (NIR) spectral region can be subject to a change in energy as a consequence of an optically-induced transition between two vibrational states, which is then directly encoded in an observed difference in photon energy between incident and inelastically-scattered radiation. Contrasting with elastic Rayleigh scattering, the terminology of inelastic Raman scattering [1, 73–76] includes the generation of red-shifted Stokes and blue-shifted anti-Stokes radiation (see Fig. 1.1 (a)), both serving as highly sensitive markers for the geometry and composition of the irradiated molecules. Reflecting the direct applicability of the quote by Nikola Tesla cited above to light-matter interactions, the photon energies and molecular-specific vibrational frequencies involved in inelastic Raman scattering can unveil the secret about a sample's chemical composition in a purely-optical, label-free way and, if incorporated into a microscopy setting, even in a spatially-resolved manner.

Enriching conventional microscopy with chemical specificity to identify and potentially even quantify the number of illuminated molecules, however, strongly relies on the rapid acquisition of broadband vibrational spectra in order to cover the excitation frequencies of all molecular species contained in the specimen and, given a desired spatial resolution and a scanning-based system, to address the quadratic dependence of the total imaging time on the lateral dimension of the sample under investigation. Accordingly, this second chapter of my thesis addresses the constant quest for ever faster hyper-spectral imaging modalities with broadband spectral coverage by introducing the pump-probe dual-comb approach for ultrafast broadband measurements at highest precision [11, 17, 19] and by presenting the successful implementation of impulsive Raman spectroscopy harnessing two synchronized femtosecond laser sources at around 1-GHz pulse repetition frequencies (see Fig. 2.1 (a)).

## 2.1 Vibrational Molecular Spectroscopy

As the characteristic patterns formed by the friction ridges of human fingers serve as unique markers of human identity, molecules can be characterized and distinguished by their unique inherent vibrational levels, which enables label-free interrogations of a sample's molecular composition via vibrational spectroscopy techniques [77], namely infrared absorption spectroscopy [11, 12, 78–80] and Raman scattering spectroscopy [1, 17, 73–76]. With typical molecular fingerprint spectra ranging from 6.7 µm to 20 µm (1500 $cm^{-1}$ to 500 $cm^{-1}$) [80], direct mid-infrared (MIR) absorption spectroscopy can excite and reveal the vibrational modes associated with a change in dipole moment. To unleash the full capabilities of vibrational spectroscopy, MIR spectroscopy can be complemented by Raman spectroscopy techniques, harnessing an inelastic scattering process sensitive to changes in polarizability and therefore being subject to different selection rules regarding the accessible vibrational modes [77].

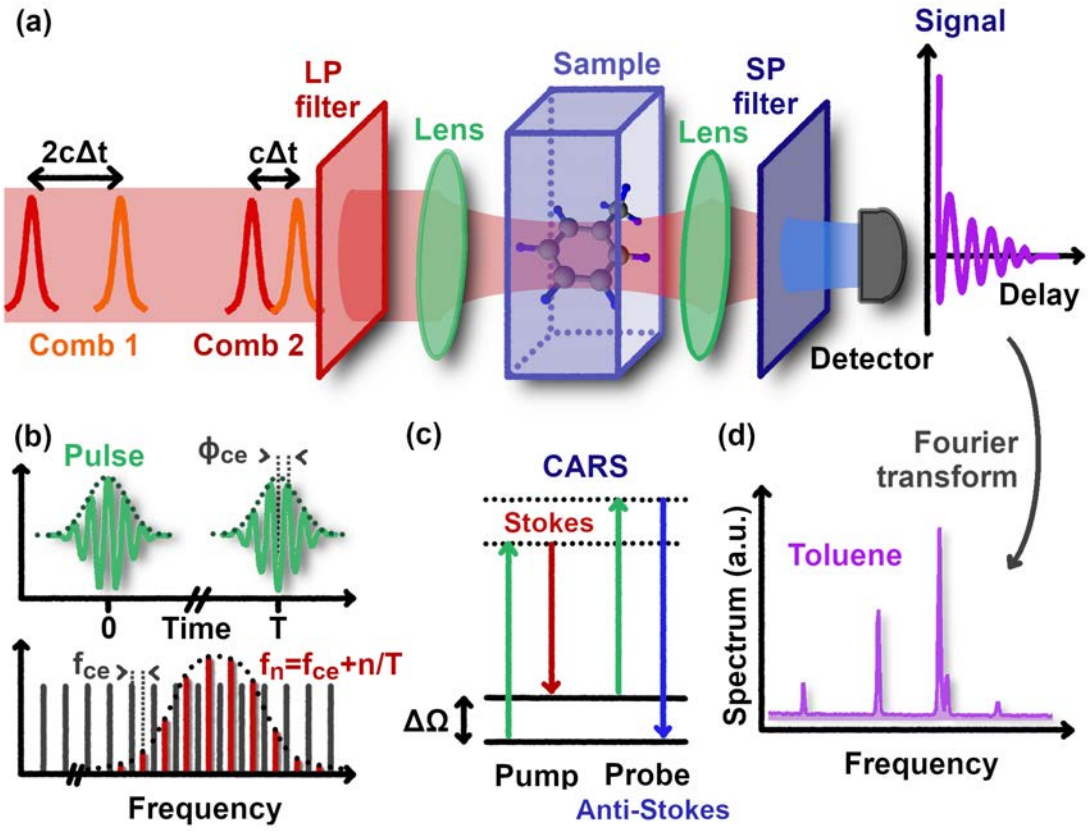


**Figure 2.1: Coherent anti-Stokes Raman scattering (CARS) scheme for molecular vibrational spectroscopy of liquid samples.** **(a)** Pump-probe dual-comb CARS spectroscopy as ultrafast Fourier transform spectroscopy scheme. **(b)** The optical frequency comb with its evenly-spaced, sharp laser lines $f_n$ and two degrees of freedom, which require stabilization, namely the repetition frequency of the pulse envelope $1/T$ and the carrier-envelope offset frequency $f_{ce}$ (figure design inspired by [81]). **(c)** Four-wave-mixing process of CARS examining two molecular vibrational levels (black solid lines) with a resonance frequency of $\Delta\Omega$. The involved virtual energy levels are depicted as dashed lines. **(d)** Intensity spectra are obtained from the time-encoded dual-comb CARS signal via Fourier transform.

While strong water absorption in the MIR spectral region hampers vibrational studies of biological systems in their natural environment via resonant absorption spectroscopy, the powerful near-infrared light sources typically applied for inelastic Raman scattering circumvent this difficulty [1]. The usage of shorter wavelengths additionally provides the advantage of smaller focal spot sizes, fostering microscopy applications, in combination with the availability of high-performance detectors in the NIR spectral region. The bottleneck of Raman spectroscopy, however, is represented by the relative

weakness of the red-shifted (Stokes) and blue-shifted (anti-Stokes) spectral components [1], generated by an inefficient, inelastic scattering process in comparison to the much more intense elastic Rayleigh scattering (see Fig. 1.1 (a)). Here, the blue-shifted anti-Stokes contribution is generated in a fluorescence-free spectral region [1], which bears the advantage of isolated detection but it is also less intense than the red-shifted Stokes' contribution to Raman scattering, owing to the typically smaller initial population of the excited vibrational states in comparison to the ground state. This challenge is tackled by coherent anti-Stokes Raman scattering [1], where two different wavelengths $\omega_F$ and $\omega_S$ with a difference matching the vibrational frequency $\Delta\Omega$ (see Fig. 2.1 (c)) mix to coherently drive all respective resonant molecular transitions in the excitation volume with a well-defined phase:

$$\omega_{AS} = \omega_F + \Delta\Omega = 2\omega_F - \omega_S \tag{2.1}$$

where $\omega_F$, $\omega_S$ and $\omega_{AS}$ represent the fundamental, red-shifted Stokes and blue-shifted anti-Stokes frequencies. The induced periodic macroscopic modulation of the material's refractive index, following the interaction with the pump pulse, causes a blue-shift of the impinging probe beam, resulting in an anti-Stokes signal that is substantially enhanced in comparison to spontaneous Raman scattering [17].

Advances in laser technology have crucially increased the excitation brilliance, boosting the sensitivity of Raman spectroscopy and thereby revolutionizing our ability to study the microscopic world with chemical specificity in a non-invasive, label-free manner. Over the last decades, multiple different variations of Raman spectroscopy have emerged including stimulated Raman spectroscopy [82], surface-enhanced Raman spectroscopy [83] and tip-enhanced Raman spectroscopy [84]. Depending on the desired application, acquisition speeds have been boosted to video-rates for spectroscopic investigations of single-color Raman bands [8] and broadband spectral coverage required for the analysis of complex samples has been demonstrated, for example, via multiplex Raman spectroscopy with chirped pulses [85] or frequency-swept laser sources [86]. A promising alternative to sweeping the wavelength of a single laser line over time, for achieving a broadband spectral coverage, are light sources emitting a comb of continuous-wave-like laser frequencies [11, 81, 87].

## 2.2 Optical Frequency Combs for Broadband Precision Spectroscopy

Pioneered by John L. Hall and Theodor W. Hänsch, optical frequency combs with their discrete and equidistant frequency components, associated with a regular train of ultrashort pulses (see Fig. 2.1 (b)), fulfill all requirements of an ideal coherent light source for broadband spectroscopic measurements at highest precision [11, 81, 88–90]. While the equidistant mode spacing $1/T$ results from the periodicity of the pulse envelope function, the difference in group and phase velocities, originating from dispersion inside the laser cavity, causes a constant slippage in carrier-envelope phase $\Phi_{ce}$ from pulse-pair to pulse-pair and a corresponding offset $f_{ce}$ in the frequency domain [81]. The unique key features of this versatile coherent light source are a broadband spectral coverage by a series of continuous-wave-like laser frequencies and its inherent phase-coherent link between optical and radio frequencies [91]. The latter implies that simultaneous stabilization of the two radio frequencies $f = 1/T$ (repetition frequency of the pulse envelope) and $f_{ce}$ (carrier-envelope offset frequency) is automatically transferred to the optical frequencies $f_n$ of the frequency comb, dispensing with the need for direct monitoring and stabilization of the high optical frequencies themselves [81, 91]. While the repetition rate of the pulse train can directly be captured by a fast photodiode, the carrier-envelope offset of an octave-spanning spectrum can, for example, be recovered by an f-to-2f interferometer [87]. Based on the fact that

the highest frequencies of an octave-spanning optical spectrum exceed the lowest frequencies by a factor of 2, a beat signal, originating from the second harmonic $2(f_{ce} + n/T)$ of the lowest frequency components and the high frequency end of the original comb spectrum $f_{ce} + 2n/T$, can be generated and uncovers the carrier-envelope offset frequency $f_{ce}$ as the difference frequency. Frequency-comb-based spectroscopy schemes include dispersive spectroscopy techniques [92, 93] as well as Fourier transform spectroscopy methods [11, 94] such as dual-comb spectroscopy [11, 90, 95, 96].

Aiming for fully exploiting the high frequency precision of the underlying comb structure, the applied detection scheme needs to match its broadband spectral coverage as well as to resolve the narrow individual comb lines [11]. Comb-based Fourier transform spectroscopy [89] tackles this challenge with a time-resolved heterodyne detection scheme. The underlying principle is the Wiener-Khinchin theorem [97], according to which the Fourier transform of the field autocorrelation function or interferogram unveils the spectrum with a frequency resolution ultimately limited only by the laser source itself. The successful acquisition of the interferogram in our case requires the sequential probing of the pulse train, composing the frequency comb, by replicated pulses at varying time delays.

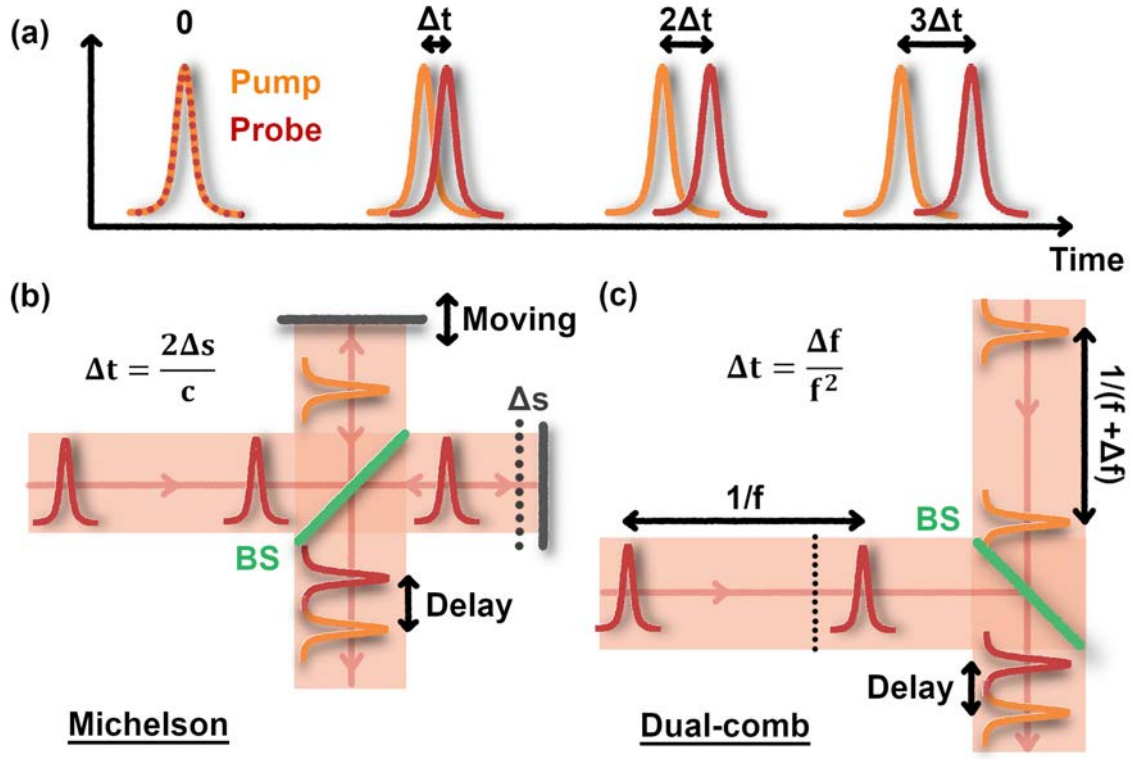


**Figure 2.2: Optical to radio frequency mapping in frequency-comb-based Fourier transform spectroscopy. (a)** Linear scanning of the time delay from pulse-pair to pulse-pair with a step size of $\Delta t$ implemented **(b)** via a Michelson interferometer (beam splitter (BS) in green, $c$ is the speed of light) equipped with a movable mirror (gray) or **(c)** a dual-comb scheme employing two femtosecond laser sources with slightly different repetition frequencies, respectively. For the Michelson interferometer, the sampling steps in time $\Delta t$ are directly linked via the speed of light $c$ to the step-wise displacement $\Delta s$ of the movable mirror, whereas the average pulse repetition frequency $f$ and the difference in pulse repetition frequencies between the two femtosecond laser sources $\Delta f$ are the decisive parameters in the dual-comb scheme.

This desired linear increase in time delay from pulse-pair to pulse-pair can alternatively be incorporated (see Fig. 2.2) by the combination of a single optical frequency comb with a Michelson interferometer [94] or by the employment of a second frequency comb with slightly different repetition frequency [95]. Both techniques yield a comparable down-converted version of the optical frequency comb by a factor of $\Delta t/T$ (typically on the order of $10^{-7}$ or $10^{-6}$) so that its whole spectrum is encoded simultaneously in a time-dependent signal, resolvable by a single photodetector at moderate speed. The latter approach,

however, referred to as dual-comb spectroscopy [11, 95] and employed in this thesis, dispenses with any movable parts and therefore generally allows for shorter acquisition times, capitalizing the high brightness of frequency combs to its full extent. Modifications to the comb spectrum, induced by the insertion of a specimen into the beam path of one or both combs, can be visualized and characterized in the same way in order to spectroscopically study the sample's optical response [11].

## 2.3 Concept of Nonlinear Dual-Comb Raman Spectroscopy

By now, the concepts underlying frequency-comb-based Fourier transform absorption spectroscopy have been successfully transferred to broadband coherent anti-Stokes Raman spectroscopy (CARS) [17, 98, 99], fully exploiting the high peak power of femtosecond pulses to coherently drive this nonlinear scattering process. In analogy to absorption spectroscopy, the required scanning of the time delay in pump-probe CARS can be implemented via a Michelson interferometer [98, 99] or a dual-comb scheme [17, 19]. Broadband spectral coverage offered by optical frequency combs, short acquisition times owing to the rapid delay scanning and enhanced focusing in the near-infrared (NIR) wavelength range render dual-comb Raman spectroscopy a very promising approach for ultrafast, high-resolution microscopy with label-free molecular specificity.

Within the framework of dual-comb CARS (depicted in Fig. 2.3 and described in [17] as well as our publication [19]), drawing on pump-probe impulsive stimulated Raman scattering, the pulses of one comb with a pulse repetition frequency of $f + \Delta f$ coherently excite molecular vibrational levels in a two-photon Raman process. Following this impulsive excitation, the induced coherent molecular oscillations modulate the refractive index of the sample at their vibrational frequency, whereby the molecular ring-down time for liquid samples is typically in the few picosecond range [100], substantially exceeding the pulse duration of the femtosecond combs. This modulation in refractive index during the molecular ringing time is subsequently probed by the pulses of the second comb, delivered at a repetition frequency of $f$. Depending on the pump-probe time delay, which is automatically scanned due to the slightly different repetition frequencies (see Fig. 2.2), the vibrational motion is either alleviated or enhanced during the probing process so that the spectrum of the probe comb experiences a blue- or red-shift, respectively [19]. The resulting intensity modulation in the generated blue-shifted anti-Stokes signal can then be isolated by spectral edge filtering behind the sample, which delivers a down-converted and therefore easily measurable copy of the optically-induced refractive index modulation (see Fig. 2.3). In analogy to dual-comb absorption spectroscopy, all covered frequency components of the molecular Raman spectrum are encoded simultaneously in this single time-resolved signal and can be revealed by a Fourier transform.

As the concepts of linear and nonlinear dual-comb spectroscopy have already been discussed in literature [11, 17, 89], the following paragraphs highlight in a condensed way only the parameters of special importance for understanding the results presented in this thesis. Recapitulating the basic principles underlying Fourier transforms, the instrumental resolution of Fourier transform spectroscopy is given by the largest feasible time delay, which is limited by the scanning range of the Michelson interferometer or by the periodicity of the envelope function in the corresponding dual-comb scheme, respectively. The latter results from the inherent property of dual-comb spectroscopy involving a repetitive scanning of the time delay from pulse-pair to pulse-pair with a step size of $\Delta t$ (see Fig. 2.2) until a perfect overlap is reached again. Pump and probe pulses coincide again after a maximum measurement time of $1/\Delta f$, in which the train of probe pulses has sampled the molecular response (see Fig. 2.3) occurring on the entire time scale of the temporal spacing between subsequent

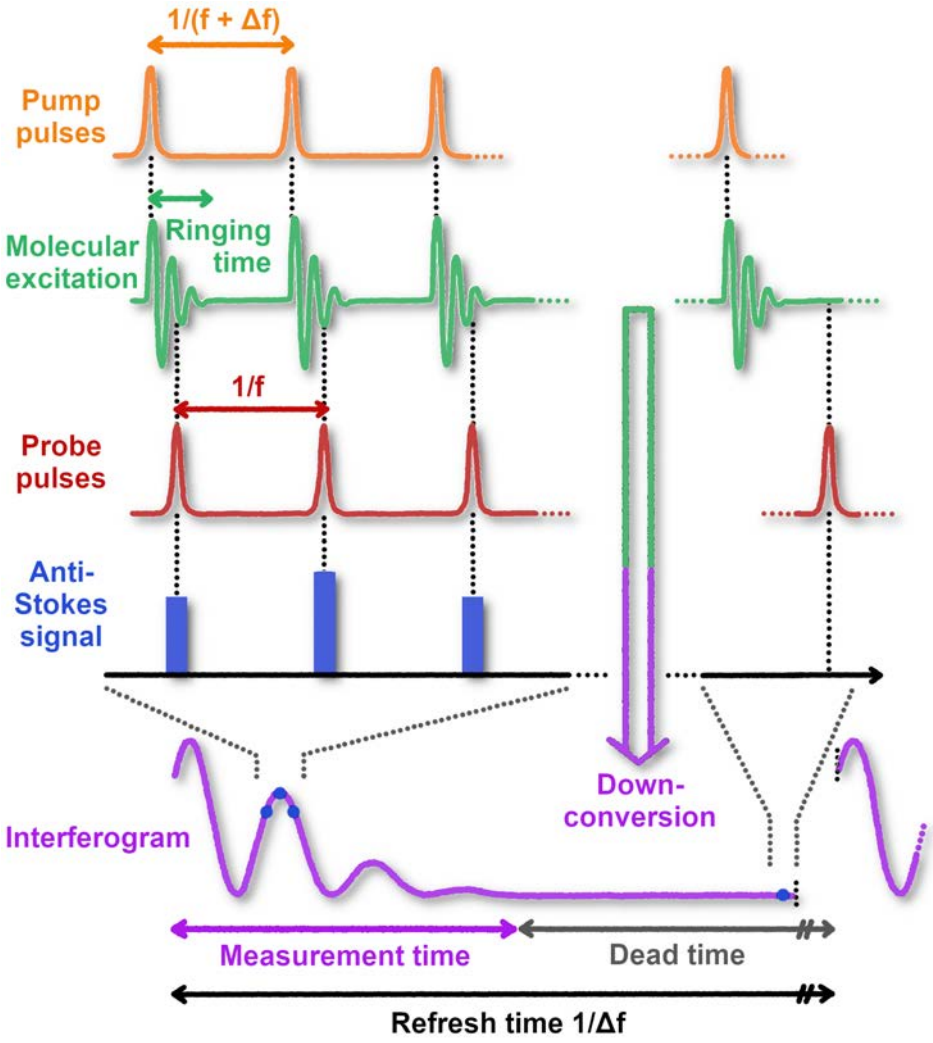


**Figure 2.3: Concept of dual-comb CARS spectroscopy.** The underlying elegant way of frequency down-conversion maps the induced refractive index modulation at molecular vibrational frequencies to a slowly-oscillating, directly-measurable anti-Stokes intensity. For liquid samples, the refresh time of the interferograms $1/\Delta f$ typically substantially exceeds the ring-down time of the molecular oscillations, which defines the measurement time of choice. (Figure design inspired by our publication [19])

pump pulses. Here, the difference in repetition frequency $\Delta f$ defines the number of pump-probe pulse-pairs contributing to the interferogram and therefore has a direct impact on the maximum achievable signal-to-noise ratio, which additionally scales with the pulse energy. In case of consecutive measurements, fast decay times and a given damage threshold for the sample, a chopper synchronized to the data acquisition can block the laser beam during the time, in which no molecular signal is detected, in order to reduce the average thermal load on the sample and thereby to allow for the application of higher pulse energies (see following CARS measurements of polystyrene beads).

Interpreting the modulation imprinted on the detected signal as a copy of the initiated molecular ringing but down-converted by a factor of $\Delta t/T = \Delta f/f$ to the radio frequency domain, valuable insights can be gained regarding the limits for the accessible resolution $\Delta\nu$ and bandwidth $\Delta B$. The time-encoded detection scheme of frequency-comb-based Fourier transform spectroscopy bears the intrinsic advantage that any undesired instantaneous background signals can be separated from the retarded molecular vibrational signatures of interest by the application of an appropriate window function [17]. This idea of harnessing temporal separation follows a strategy similar to gated heterodyne CARS microscopy [101] or to the recently reported field-resolved spectroscopy technique with its optical

gating process involved in electro-optic sampling [12]. Moreover, such a window function can suppress the contribution of noise by restricting the analyzed time delays to the sample's maximum molecular ringing time. In case a triangular window function [17], selecting a certain measurement time $T_{\mathrm{meas}}$ corresponding to the time interval $T_{\mathrm{opt}}$ in the optical domain, is applied to a recorded interferogram before performing the Fourier transform step, the achieved apodized spectral resolution $\Delta\nu$ can be calculated in dependence of the pulse repetition frequency $f$:

$$\Delta\nu = \frac{1.8}{T_{\mathrm{opt}}} = \frac{1.8}{T_{\mathrm{meas}}} \cdot \frac{T}{\Delta t} = \frac{1.8}{T_{\mathrm{meas}}} \cdot \frac{f}{\Delta f} \tag{2.2}$$

Under the assumption of sufficiently high detector speed, the maximum value of the spectral bandwidth $\Delta B$ accessible for a given repetition frequency $f$ can be deduced from the Nyquist-Shannon sampling theorem in dependence of the difference in repetition frequencies $\Delta f$ [11]:

$$\Delta B \leq \frac{1}{2\Delta t} = \frac{f}{2} \cdot \frac{f}{\Delta f} \tag{2.3}$$

The versatility of dual-comb spectroscopy is highlighted by its two degrees of freedom, namely the average pulse repetition rate $f$ and the difference in repetition frequencies $\Delta f$, which serve for fine tuning the trade-off between bandwidth $\Delta B$, refresh time $1/\Delta f$ and optical resolution $\Delta\nu$ according to the application of interest. Aiming for ultrafast repetitive data acquisition at a given spectral bandwidth $\Delta B$, the shortest feasible refresh time $1/\Delta f$ is limited by the repetition frequency $f$ to:

$$\Delta f = \frac{f^2}{2\Delta B} \tag{2.4}$$

Consequently, higher pulse repetition frequencies offer a higher flexibility and the potential for shorter waiting times in liquid samples while in high-precision measurements a choice of smaller $\Delta f$ can trade acquisition speed for an improved signal-to-noise ratio. A measure for the efficiency of repetitive data collection is further given by the duty cycle $D$ [17,19], defined as the ratio of the selected measurement time $T_{\mathrm{meas}}$ to the refresh time of the interferograms $1/\Delta f$:

$$D = T_{\mathrm{meas}} \cdot \Delta f = 1.8 \cdot \frac{f}{\Delta\nu} \tag{2.5}$$

The linear scaling of the duty cycle with the pulse repetition frequency $f$ implies that higher pulse repetition frequencies do not only offer the potential for faster measurement times but also for an enhancement of the duty cycle at a given resolution and covered spectral bandwidth. Accounting for the constant quest in microscopy applications for ever higher acquisition speeds, the following study, presented in this thesis and in our corresponding publication (see Mohler et al. [19]), advanced the dual-comb approach of multiplex coherent Raman spectroscopy [17] from a pulse repetition frequency of 100 MHz to 1 GHz. Thereby, the duty cycle of the data acquisition is enhanced by a factor of 10 while the minimum waiting period between consecutive acquisitions $1/\Delta f$, according to Eq. (2.4), can be lowered by up to two orders of magnitude. Ideally, pulse repetition frequencies and their respective pump-probe cycles should approach the relaxation time of the sample, needed to return to its initial state. However, the damage threshold of the specimen restricts the maximum average thermal load that can be deposited in the sample, which hampers the use of high repetition frequency lasers for four-wave mixing processes such as CARS since their signal typically scales with the cube of the laser peak power [1]. This challenge also becomes evident from the prediction of Ideguchi et

al. [17], who theoretically extrapolated from their 100-MHz results an achievable signal-to-noise ratio of merely 20 at 1-GHz pulse repetition frequency and a refresh time of 1 ms. Our proposed strategy and experimental demonstration on how to mitigate this predicted limitation for GHz pulse repetition frequencies are two central topics of the following paragraphs.

## 2.4 Dual-Comb CARS Setup at 1-GHz Pulse Repetition Frequency

Our successful implementation of the presented pump-probe CARS scheme for ultrafast measurements relies on two synchronized femtosecond laser sources with highly stable repetition frequencies, pulse compression techniques for efficiently driving the nonlinear Raman process, a set of optical filters for suppression of undesired background signals and custom post-processing including a Fourier transform step of the recorded time-encoded signal. The dual-comb CARS setup, implemented in the course of this thesis as depicted in Fig. 2.4 and described in our publication [19], harnesses two identical titanium-sapphire femtosecond mode-locked lasers (Laser Quantum, Taccor-10s) with repetition frequencies around 1 GHz, spectra centered around 795 nm and a bandwidth of 60 nm (FWHM). Piezo-electric transducers adjust the repetition frequency via the cavity length of the laser and a servo controller (Laser Quantum, TL-1000) phase-locks the repetition frequency to an external reference provided by a radio-frequency synthesizer (Rohde & Schwarz, SMA100A-B22). In contrast to absorption spectroscopy, the applied dual-comb CARS scheme merely relies on intra-pulse frequency differences of the comb lines (see Fig. 2.1 (c)) that are intrinsically passively stabilized, which renders any active stabilization of the carrier envelope offset redundant and substantially reduces the complexity of the setup [19].

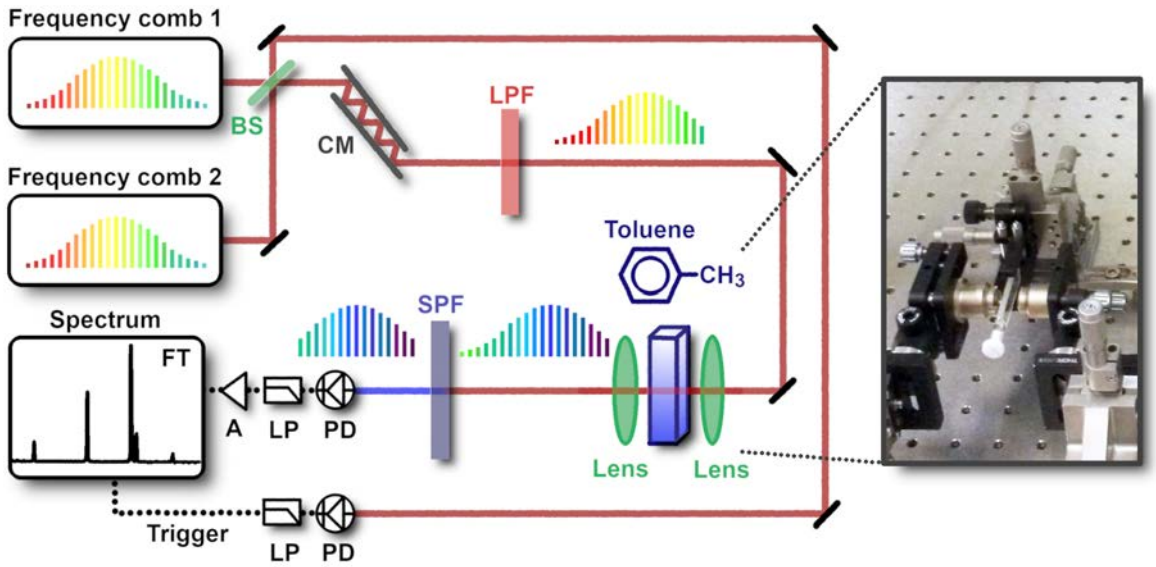


**Figure 2.4: Experimental dual-comb CARS setup for liquid samples.** The experimental setup employs two femtosecond laser sources with slightly different repetition frequencies, chirped mirrors (CM) for pulse compression, a combination of optical filters (long-pass (LPF) and short-pass (SPF)) for isolating the generated anti-Stokes radiation from the fundamental light as well as a signal detection unit, including a silicon photodiode (PD), low-pass (LP) filtering and amplification (A). Software-based post-processing finally reveals the Raman spectrum of the sample under investigation via Fourier transform (FT).

The two laser beams are combined on a pellicle beam splitter, where one of the two outputs provides a trigger signal at a periodicity of $1/\Delta f$ by monitoring the time-domain interference between the two trains of femtosecond laser pulses on a fast photodiode. The second output leads to the CARS setup where the efficiency of the four-wave mixing process and the ultimate time resolution of the

pump-probe scheme are boosted by the insertion of chirped mirrors (CM), which compensate for group delay dispersion, induced by optical components as well as the laser itself, and time-compress the laser pulses to durations of less than 20 fs at the sample's position. A combination of optical long-pass filter (LPF) and short-pass filter (SPF) largely suppresses any spectral components overlapping with the spectral region of the blue-shifted anti-Stokes radiation (cut-off at roughly 750 nm) before the sample as well as separates the generated anti-Stokes contribution from the fundamental light of the titanium-sapphire lasers after the sample (cut-off: 750 nm). Consequently, the maximum spectral bandwidth of the experimentally accessible CARS spectra is limited on the low-wavenumber side by the optical filters and on the high-wavenumber side by the spectral bandwidth of the femtosecond laser sources (see also Mohler et al. [19]). Tight focusing of the incident laser pulses with energies of 0.5 nJ relaxes the phase matching condition of forward-generated CARS [1]. The anti-Stokes radiation, emerging from the 1-mm–thick quartz cuvette containing the sample, is collimated by a second lens, optically short-pass filtered and focused onto a fast silicon photodiode (Newport, 1621).

Non-resonant signals such as non-resonant four-wave mixing can dramatically impede CARS measurements at high sensitivity [1]. The depolarization potential of liquid samples, however, can be exploited to suppress undesired non-resonant interferometric background signals by using nearly orthogonally-polarized laser beams while retaining a substantial portion of the resonant CARS signal of interest [19]. Additionally, non-interferometric signals occurring at the repetition frequency of the laser sources and its harmonics can be removed by electronic filtering. After amplification (L-3 Narda-MITEQ, AU-1332), the time-domain signal is recorded by a data acquisition board (AlazarTech, ATS9360). Custom post-processing includes the application of a triangular window function [17] before the subsequent Fourier transform in order to remove any residual instantaneous non-resonant contribution from the retarded molecular signal of interest and to reduce the noise level by excluding the time interval exceeding the decay time of the molecular vibrations (see also Mohler et al. [19]).

## 2.5 Experimental Results of Dual-Comb CARS at 1-GHz Repetition Frequency

To study the feasibility of dual-comb CARS with mode-locked laser sources at 1-GHz pulse repetition frequency, the following experiments were performed at the MPQ in collaboration with Bernhard J. Bohn and the results presented in the following paragraphs were partially published in 2017 (see Mohler et al. [19]) as the first experimental demonstration of high-speed dual-comb CARS employing two femtosecond laser sources of around 1-GHz pulse repetition frequency.

### 2.5.1 Acquisition Time and Signal-to-Noise Ratio

Figure 2.5 highlights the versatility of dual-comb Raman spectroscopy provided by the high pulse repetition frequency of 1 GHz at the example of neat toluene. All four dual-comb CARS spectra (see Fig. 2.5 (a)) comprise in total 166 spectral elements covering a spectral bandwidth of 1000 $cm^{-1}$ at an apodized resolution of 6 $cm^{-1}$ and clearly resolve the five most intense Raman lines of toluene in this spectral region [102]. The ample flexibility of the applied dual-comb approach, resulting from the finely tunable difference in pulse repetition frequencies and the freely selectable number of averaged records, offers the capability of both ultrafast single records and high-precision measurements contained in a single device. For individual spectra, the experimental time is determined by the desired resolution

of 6 $cm^{-1}$ and can be set as short as 20 µs or even 5 µs for differences in pulse repetition frequencies of 500 Hz and 2000 Hz, respectively. Figure 2.5 (c) visualizes that the signal-to-noise ratio scales approximately inversely with the square-root of the difference in laser repetition frequencies $\Delta f$.

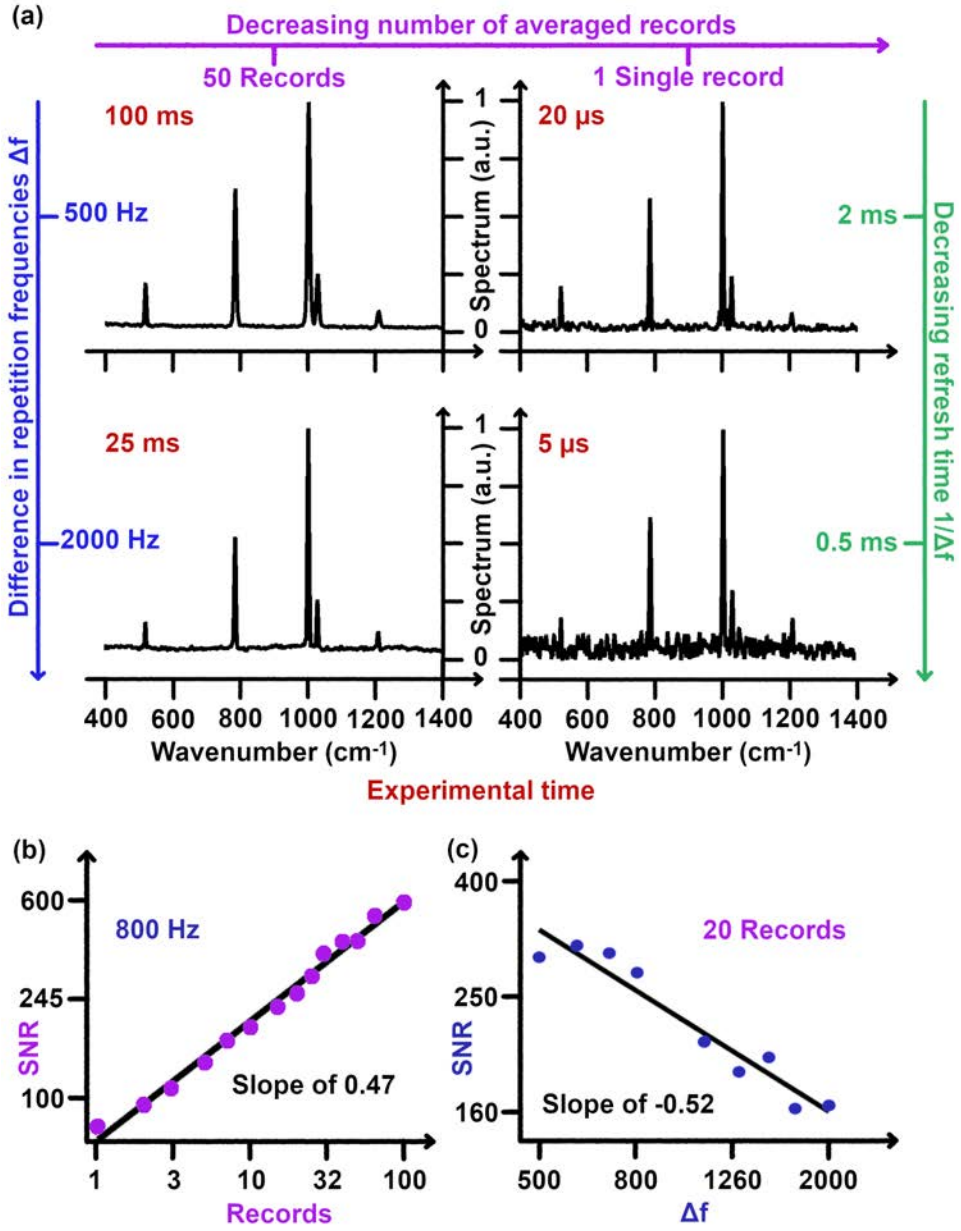


**Figure 2.5: Dual-comb CARS spectra of toluene at 1-GHz laser repetition frequency. (a)** Versatile data acquisition enabling fine-tuning of signal-to-noise ratio (SNR) up to 600 or an experimental time down to 5 µs in accordance to the desired application. **(b)** Approximate square-root dependence of the signal-to-noise ratio on the number of averaged records at the example of a difference in laser repetition frequency of 800 Hz. **(c)** As depicted for 20 averaged records, the signal-to-noise ratio scales approximately inversely with the square-root of the difference in repetition frequency owing to the decreasing number of pulse-pairs composing a single interferogram. Log-scale display is employed for panels **(b)** and **(c)**.

Here, the noise is taken as the standard deviation of the baseline in the signature-free wavenumber region around 1100 $cm^{-1}$. Averaging is a second degree of freedom to adjust the signal-to-noise ratio (see Fig. 2.5 (b)), which bears the intrinsic advantage that shorter individual measurement times enable the acquisition of distortion-free spectra while residual inter-acquisition fluctuations in repetition frequencies can be eliminated in post-processing. In case of multiple acquired records, the refresh time of the interferograms $1/\Delta f$ represents the decisive limitation for the experimental time, clearly

favoring our 1-GHz repetition frequencies over the previous 100-MHz system (see Eq. (2.4)). The depicted CARS spectrum for 50 averaged records acquired at a difference in repetition rates of 500 Hz (see Fig. 2.5 (a)) further highlights the capability of broadband dual-comb spectroscopy at GHz pulse repetition frequencies to provide the high signal-to-noise ratio desired for precision measurements.

### 2.5.2 Heterodyne Coherent Anti-Stokes Raman Scattering

Considering the damage threshold of the sample, the major challenge of increasing the laser repetition frequency is imposed by the typically cubic dependence of the dual-comb CARS signal on the peak intensity of the laser pulses [1]. However, the dramatic drop in signal-to-noise ratio, expected for a 1-GHz system compared to laser repetition frequencies of 100 MHz, can be mitigated by a heterodyne detection scheme with a local oscillator [98, 103].

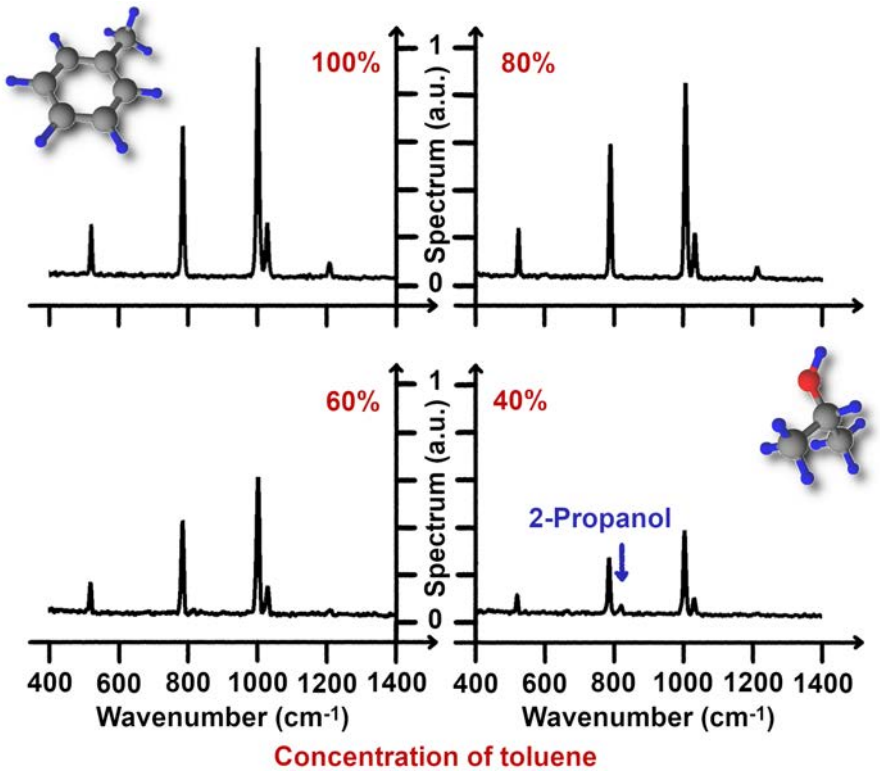


**Figure 2.6: Linear concentration dependence of dual-comb CARS spectra.** Heterodyne detection of the CARS signal with a local oscillator at the example of a mixture of toluene and 2-propanol.

The generated anti-Stokes field in the pump-probe dual-comb scheme results from induced macroscopic third-order polarization and is given by [1]:

$$E_{\mathrm{CARS}} \propto \chi^{(3)} \cdot E_{\mathrm{Pump}} \cdot E^{*}_{\mathrm{Pump}} \cdot E_{\mathrm{Probe}} \tag{2.6}$$

where $\chi^{(3)}$ is the third-order susceptibility, which is proportional to the number of molecules, while $E_{\mathrm{Pump}}$ and $E_{\mathrm{Probe}}$ are the electric fields of the pump and probe pulses, respectively. Heterodyning the generated CARS field with the phase-coherent blue edge of the probe pulse $E_{\mathrm{Probe}}$, which can experimentally be realized by slightly rotating the interferometric long-pass filter in front of the sample (see our publication [19] and Fig. 2.4), yields a recorded signal of:

$$S^{\mathrm{LO}}_{\mathrm{CARS}} \propto |E_{\mathrm{CARS}} + E_{\mathrm{Probe}}|^2 = |E_{\mathrm{CARS}}|^2 + |E_{\mathrm{Probe}}|^2 + 2\chi^{(3)} \cdot I_{\mathrm{Pump}} \cdot I_{\mathrm{Probe}} \tag{2.7}$$

The second term $|E_{\text{Probe}}|^2$ is independent of the pump-probe time-delay while the first term $|E_{\text{CARS}}|^2$ can be considered as comparatively small since the nonlinearly-generated anti-Stokes radiation is typically much weaker than the incident fundamental light [1]. This leaves the third term as the most dominant modulated contribution, which approximately results in a quadratic dependence on the pulse energy and a linear dependence on the concentration [19,103]. The latter is also observed experimentally for a mixture of toluene and 2-propanol (see Fig. 2.5.2) and, in combination with the precise adjustment of the spectral overlap after the long-pass filter, implies that the enhanced signal-to-noise ratio can indeed be attributed to such heterodyne mixing in this improved detection scheme. In addition to the observed boost in signal-to-noise ratio, being of particular importance for systems employing laser sources with ultrafast pulse repetition frequencies, the resulting linear concentration dependence, in contrast to a quadratic scaling, further facilitates the detection of molecules at low concentrations as well as any quantitative analysis of a sample's molecular composition.

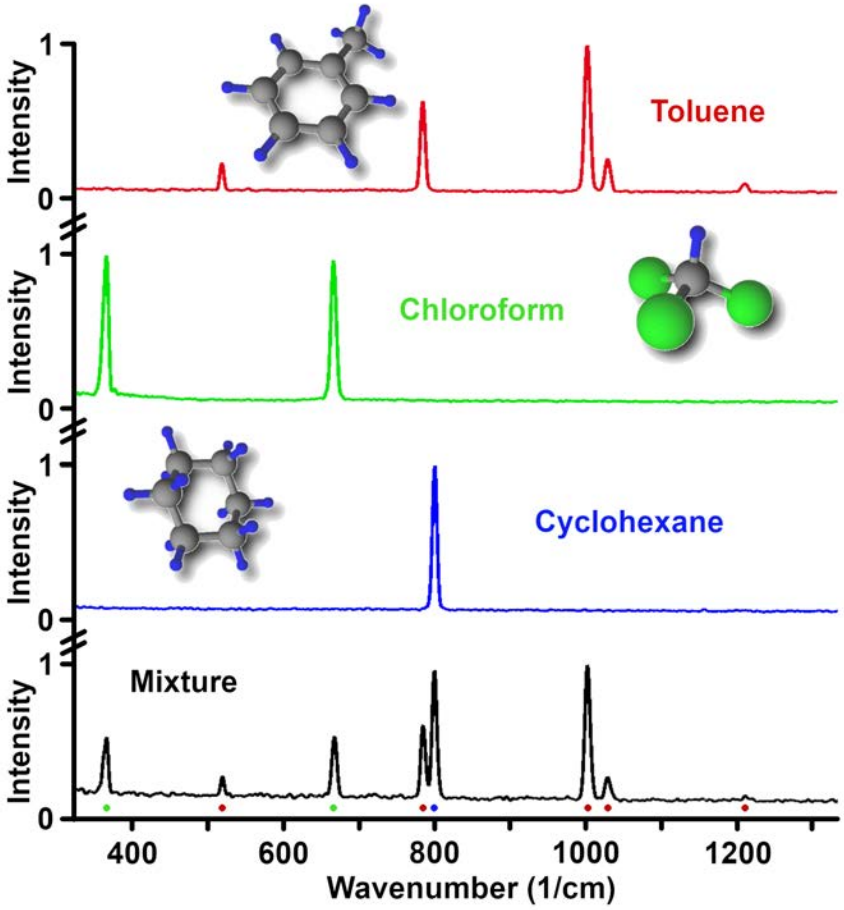


**Figure 2.7: Broadband and high-resolution dual-comb Raman spectra of a mixture comprising of toluene, chloroform and cyclohexane.** For each of the four traces, 120 individual spectra were averaged, corresponding to a total measurement time of 2 ms and experimental time (dead time included) of 200 ms. Mixing ratio of 1:1:1.

Figure 2.7 illustrates the chemical specificity offered by dual-comb CARS spectroscopy at 1-GHz pulse repetition frequency at the exemplary mixture of toluene, cyclohexane and chloroform (mixing ratio of 1:1:1) for a difference in repetition frequencies of $\Delta f = 600$ Hz. The provided bandwidth enables the observation of multiple spectral features spanning approximately 850 $\text{cm}^{-1}$ in total (Raman lines of chloroform at 366 $\text{cm}^{-1}$ [104] and toluene at 1210 $\text{cm}^{-1}$ [102]) while at the same time the apodized resolution of 6 $\text{cm}^{-1}$ is high enough to clearly distinguish the neighboring Raman transitions of toluene at 788 $\text{cm}^{-1}$ [102] and cyclohexane at 802 $\text{cm}^{-1}$ [105].

## 2.6 Towards Dual-Comb Raman Microscopy

The presented results demonstrate that femtosecond laser sources of 1-GHz pulse repetition frequency can be successfully employed for obtaining broadband and high-resolution dual-comb CARS spectra of neat liquids at refresh rates in the few kHz-range. Duty-cycles are enhanced ten-fold in comparison to a previous study with a 100-MHz system [17]. Moreover, a heterodyne detection scheme is shown to boost the signal-to-noise ratio and thereby to mitigate the detrimental effects of the reduced pulse energies, which renders the presented approach a very versatile tool for vibrational spectroscopy.

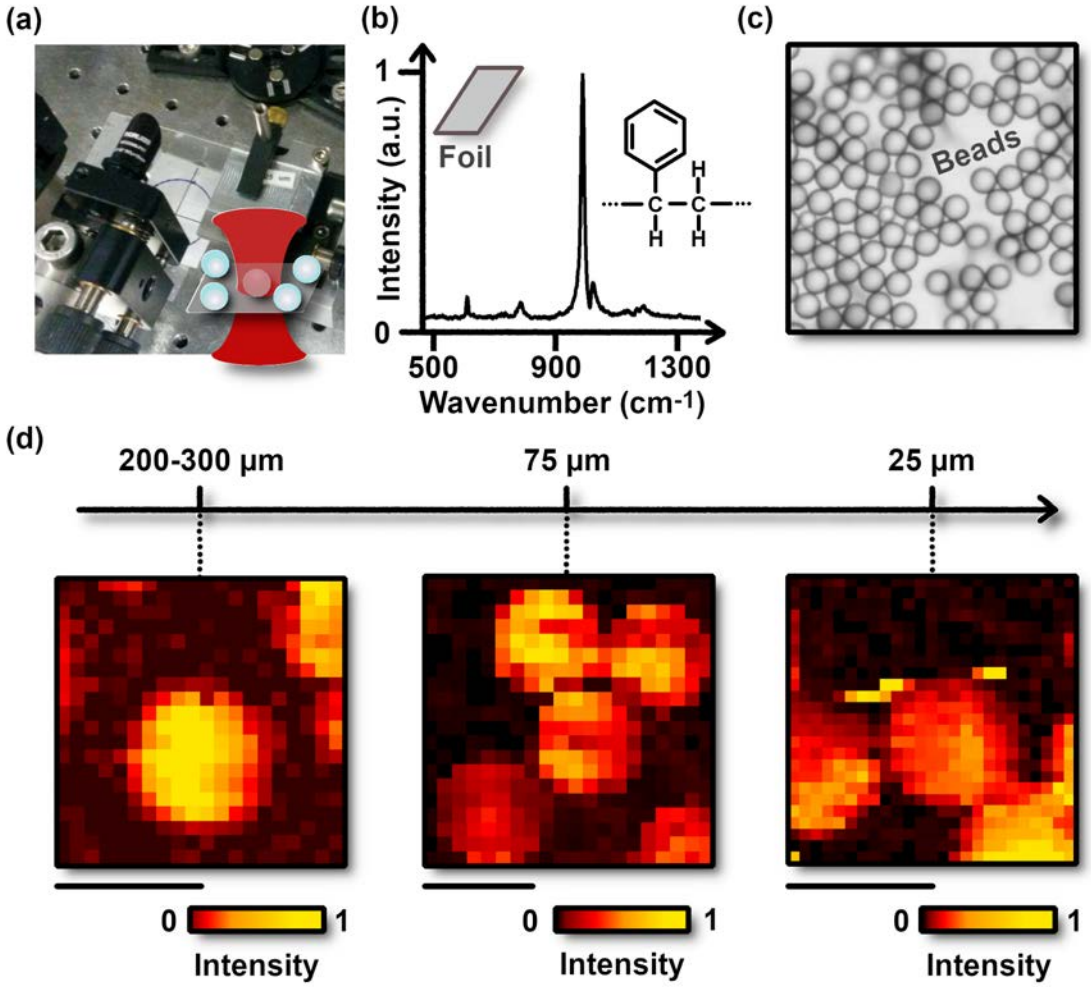


**Figure 2.8: Towards dual-comb CARS microscopy.** **(a)** Close-up view of the experimental setup for epi-directed CARS microscopy of polystyrene beads. **(b)** Dual-comb spectra obtained at 100-MHz laser repetition rate of a 125-µm-thick polystyrene foil, employed for calibration purposes and as reference. **(c)** Distribution of the polystyrene beads on a glass substrate imaged by a Zeiss microscope. **(d)** Dual-comb CARS microscopy images for polystyrene beads of different sizes. For each sampling point, 10 records were averaged to yield an entire Raman spectrum, from which the intensity of the central peak around 1001 $cm^{-1}$ is depicted in the 2D intensity maps. The scale bars visualize 250 µm, 75 µm and 25 µm, respectively, for a direct correlation with the corresponding sizes of the polystyrene beads.

Our first successful demonstration of dual-comb Raman spectroscopy at 1-GHz laser repetition frequency in 2017 [19] has not only paved the way for the implementation of a high-throughput label-free particle analyzer for statistical analysis of a large number of polystyrene microparticles in 2018 [106] but it additionally suggests such dual-comb schemes as powerful tools for high sensitivity experiments requiring rapid signal averaging and for fast hyper-spectral imaging alike.

The prospect of extending the presented dual-comb Raman scheme from liquid phase spectroscopy to hyper-spectral microscopy of solid samples was further explored in the course of this thesis by proof-of-principle experimental investigations of polystyrene beads performed with a 100-MHz dual-comb system (see Fig. 2.8). For this purpose, the experimental spectroscopy setup, based on two titanium–sapphire lasers (Synergy20 UHP; Femtolasers) and described in detail in [17], was complemented with a motorized and computer-controlled scanning stage for the sample and with a parabolic mirror for focusing the incident pulses as well as for collecting the epi-directed CARS signal (see Fig. 2.8 (a)). A combination of two choppers synchronized to the data acquisition reduced the heat load on the sample by blocking the fundamental light during the dead time. In the applied microscopy configuration, the chemical Raman contrast measured in epi-direction depends on the size and shape of the scattering objects, sharp discontinuities at interfaces breaking the symmetry of the focal volume and the amount of elastic backscattering of the forward-generated CARS signal [1].

Besides, the dispersion compensation has to be adjusted more precisely for imaging a single layer of microscale polystyrene beads than for liquid samples, the polarization of the two femtosecond laser sources was chosen to be approximately parallel and a 125-µm-thin polystyrene foil served for calibration and alignment purposes (see Fig. 2.8 (b)). Figure 2.8 (d) finally presents our successful demonstration of dual-comb CARS microscopy visualizing polystyrene beads with sizes down to 25 µm in a proof-of-principle experiment, whereby the spatial resolution limit of the system has not even been fully exploited yet. The obtained CARS microscopy images clearly demonstrate that bare polystyrene beads, placed on a simple glass substrate, can withstand the high peak powers of femtosecond laser sources at 100-MHz repetition frequency given an appropriate scanning scheme, even without being covered by a chemical solution for enhanced heat removal. Therefore, these results marked a first but important step towards hyper-spectral dual-comb Raman microscopy and paved the way for future microscopy studies with 1-GHz pulse repetition frequencies, mixtures of microscale beads with different chemical signatures and ultimately even biological samples.

In the meantime, the dual-comb CARS scheme has also been successfully applied to surface-enhanced Raman spectroscopy (SERS) [107] and other intriguing applications are likely to follow in the near future. The technique of SERS [83] arose from the discovery of a dramatic increase of Raman scattering originating from molecules in close vicinity to metallic nanoparticles or rough metal surfaces and laid the foundation for the broad field of plasmon-enhanced spectroscopy. The related technique of tip-enhanced Raman spectroscopy [84] unites this substantial increase in sensitivity with nanoscale spatial resolution, illustrating the long-term perspective of hyper-spectral Raman imaging at reasonable acquisition speeds in combination with nanoscale precision. While the maximum spatial resolution in conventional optical microscopy is governed by Abbe's diffraction limit, the excited surface plasmons of an illuminated raster-scanned sharp metallic nanotip enhances the light field in close vicinity of the tip so that the obtained Raman spectrum for each sampling point originates primarily from molecules confined to a nanoscopic volume of the sample [84].

Even though such near-field methods can surpass the diffraction limit of light, electron microscopes, owing to the ultrashort de Broglie wavelength [48], can still exceed the resolution accessible in optical microscopy by far [4, 5]. However, standard electron diffraction and microscopy typically applied in material science or biology do not offer any time resolution. For this reason, the following chapters continue our journey towards high-resolution imaging in space and time by illustrating how the principles underlying optical pump-probe measurements, such as dual-comb CARS, can successfully be transferred to enable ultrafast electron diffraction and microscopy studies of highly dynamical light-matter interactions on their fundamental time and length scales.

# 3

# Femtosecond Electron Pulses and Terahertz Radiation

*"The electron: may it never be of any use to anybody!"*

*– quote by Joseph J. Thomson*

At the time when Joseph J. Thomson discovered a tiny particle of electrically-charged matter, the electron, it was impossible to foresee the spectacular impact his discovery should hold on revolutionizing the human understanding of the composition and functionality of matter and thereby ultimately also on the triumphant development of the electronics industry in the decades to follow. Nowadays, the substructure of atoms is well characterized, the principles of quantum mechanics are well established, countless electronic devices such as computers and cell phones considerably shape the everyday life of today's society and electron microscopy unveils interesting glimpses of the atomic world around us. Despite these tremendous achievements in the past, there still remains a wide range of intriguing opportunities for future developments and applications though, including the incorporation of femtosecond or even attosecond time resolution into conventional electron microscopy in order to gain valuable insights of ultrafast structural dynamics from an atomic level perspective [46, 69, 108].

Ever since the demonstration of the first prototype systems by Clinton Davisson and Lester Germer in 1928 [45] as well as Ernst Ruska and Max Knoll in 1932 [109], electron diffraction setups and electron microscopes, respectively, have served humanity as the ultimate magnifying glasses providing high-resolution structural information down to sub-atomic scales [4, 5]. As two of the most important milestones on the venture towards high-precision imaging, these techniques have caused a tremendous impact on biology and material science over the last decades. Relying on the velocity-dependent de Broglie wavelength [48] of accelerated free electrons in vacuum and their charged nature, ultrafast microscopy and diffraction share the elusive access to certain phenomena not accessible with photons. Femtosecond optical spectroscopy techniques, including dual-comb Raman spectroscopy (see Chapter 2), can provide valuable molecular-specific insights by tuning the optical probe to specific electronic or vibrational transitions, whereby the window of observation on the dynamics is typically restricted by selection rules [43, 77]. Harnessing a different mechanism of contrast, free electrons probe the arrangement and vibrational excitations of all atoms and molecules of the material via the interaction of their electron charge with the material's Coulomb potential, shaped by the electron density together with the crystal lattice [110]. Equipped with sufficiently short electron pulses (see e.g. Fig. 3.1), electron diffraction and microscopy can therefore investigate atomic motion in space and time [46, 68, 69, 108].

Due to the substantially lower weight of electrons compared to the cores, the electron densities of the samples under investigation show an almost instantaneous response to any applied perturbation [7], whereby the respective dynamics of bound electrons become the primary processes in the case of dielectrics while the functionality of semiconductors and metals is determined by the collective motion

of charge carriers. Thus, femtosecond or even attosecond time resolution is required to capture the fastest dynamics. Besides, the elementary charge of free electrons in a microscopy setting can serve as a sensitive probe for any magnetic and electric field distributions of arbitrary shape [54], dynamically or statically induced inside the sample. In this way, the application regime can be extended from studies of femtosecond atomic motions [46, 68, 69] to the examination of sub-excitation-cycle electrodynamics in nanophotonic materials (see Chapter 5), complementing optical spectroscopy and microscopy on their venture towards capturing a conclusive picture of the microscale, nanoscale and atomic world.

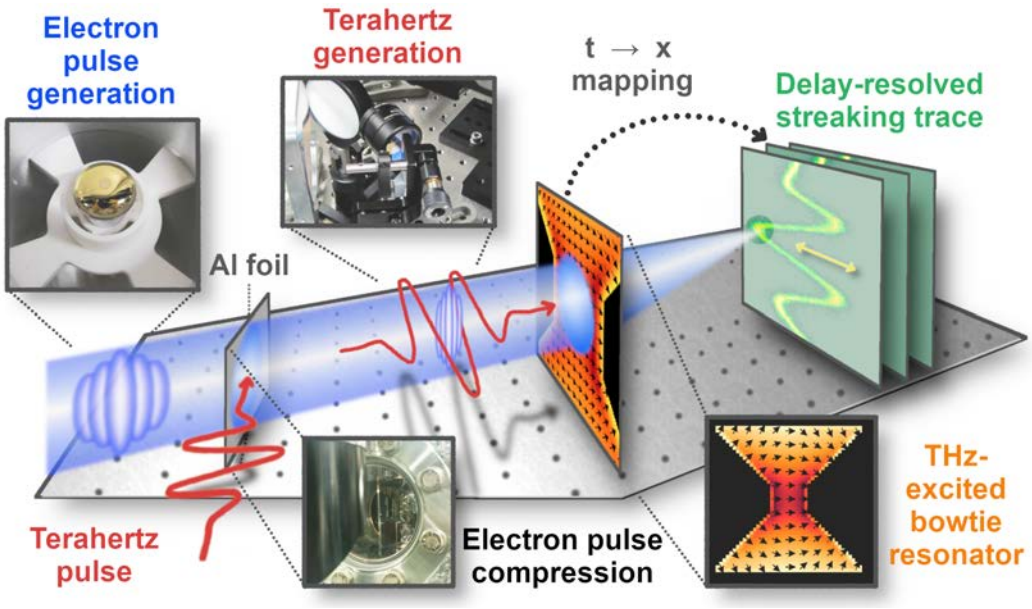


**Figure 3.1: Terahertz-based electron pulse compression and characterization.** Few-electron pulses (blue), for reduced Coulomb repulsion effects, are generated via the photoelectric effect by laser pulses impinging on a gold-coated sapphire cathode and are subsequently accelerated to energies of 75 keV. The dynamic optical near fields (amplitude map in orange, directions as black arrows) of a resonantly-excited bowtie-shaped aperture in a copper film induce a time-dependent deflection of the electron beam (yellow arrow), mapping the temporal profile of the electron pulses onto a spatial coordinate. Scanning of the pump-probe time delay generates a delay-resolved streaking trace, detectable by a phosphor-coated CMOS camera (green). Functioning as a temporal lens for all-optical electron pulse compression, close to single-cycle terahertz (THz) pulses (red) interact with the electron probe pulses at a planar mirror surface (gray). The mediated THz-electron interaction serves for imprinting a negative velocity chirp onto the electron pulses in order to counteract vacuum dispersion and to deliver the shortest electron pulse duration precisely at the position of the bowtie-shaped aperture (i.e. the designated position of the sample).

## 3.1 From Optical to Electron Probe Pulses

By merging high-precision conventional diffractive imaging with a rapid pump-probe detection scheme, ultrafast electron diffraction (UED) [7, 50, 61, 69] can reveal a wealth of dynamics involving molecules, atoms and charge carriers. In contrast to optical pump pulses, sub-relativistic electron probe pulses suffer from undesired temporal broadening effects attributed to vacuum dispersion and Coulomb repulsion [20, 111], resulting from the finite rest mass and charged nature of electrons, respectively. For this reason, the successful incorporation of the superior spatial resolution provided by the ultrashort electron de Broglie wavelength [48] into an ultrafast optical-pump electron-probe scheme requires a transfer of the established concepts of light optics to the design of electron optics (see Fig. 3.2) for efficient deflection, focusing and in particular for electron pulse compression. With electrons being strongly scattered and absorbed in air and solid materials such as glass, electron-based experiments require operation in low-pressure environments and refractive optics known from optical systems

have to be replaced by magnetic and electric fields, harnessing the charged nature of electrons. While deflection and beam-guiding can be implemented via magnetic multipoles, Hans Busch [112] paved the way for efficient focusing and imaging in electron microscopes by discovering that the magnetic field of a solenoid can manipulate electron beams in a comparable way as convex glass lenses affect optical radiation (see Fig. 3.2). Here, the focal distance of magnetic lenses scales inversely with the square of the electric current running through the solenoid and the focusing capability is further accompanied by a rotation of the electron beam, which becomes essential for the correct interpretation of electron diffraction and microscopy data [22, 113]. The flexibility in almost arbitrarily shaping electron pulses by the means of electromagnetic fields, however, also comes at the cost of a high sensitivity to any stray fields potentially infiltrating the experimental setup (see Chapter 4).

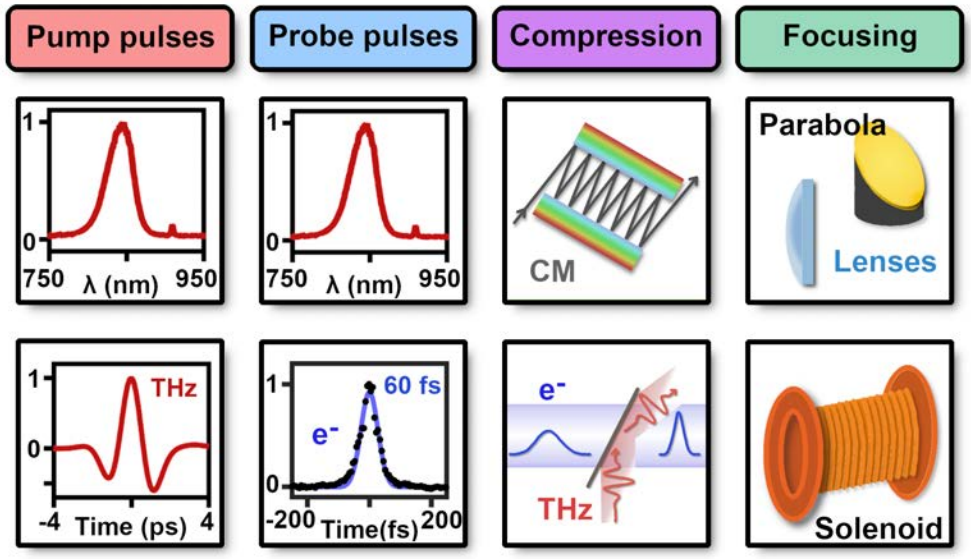


**Figure 3.2: Pump-probe approaches for ultrafast measurements.** Photons and electrons as femtosecond probes for ultrafast pump-probe measurements at the examples of dual-comb Raman spectroscopy (first row) and electron nanodiffraction (second row). For the electron diffraction scheme employed in this thesis, single-cycle terahertz (THz) radiation replaces the femtosecond pump pulses (first column), time-compressed sub-100-fs electron pulses serve as probe pulses (second column), all-optical electron pulse compression at a thin metal foil fulfills the role of chirped mirrors (CM) in optics (third column) and focusing is achieved by taking advantage of magnetic fields originating from solenoids (fourth column).

Recapping the limits for the time resolution in pump-probe measurements, imposed by the pulse durations as well as by the synchronization accuracy of pump and probe pulses, stresses the importance of stabilizing the pump-probe delay and of generating the shortest possible electron pulse durations at the position of the sample. Electron sources based on laser-triggered photoemission can deliver sub-relativistic electron pulses [59, 60]. Owing to Coulomb repulsion in dense electron bunches, their inherent energy spread and the fermionic nature of electrons, a gradual increase of the pulse duration, however, is observed along the direction of propagation [20]. Space charge effects can be mitigated at the expense of electron flux by reducing the number of electrons per pulse [18, 111]. While covering the distance from the source to the sample even low-density electron bunches with a certain energy distribution, however, will get sorted according to their velocities, with faster electrons gradually accumulating in the leading part and slower electrons in the trailing part of the electron pulse. Thus, sub-relativistic electron pulses are always subject to temporal broadening in the course of propagation. To reach ultimately short electron pulse durations, vacuum dispersion has to be actively compensated for, as chirped mirrors counteract detrimental dispersion effects from optical components on the duration of laser pulses (see Fig. 3.2). Since ultrashort pulse durations cannot be maintained over

longer distances for sub-relativistic electrons, previously demonstrated complementary approaches for ultrafast measurements include: (1) compact systems with minimized distances of propagation [59], (2) active shaping of the electrons' velocity distribution in a designated manner (i.e. like a temporal lens) to generate the shortest pulses precisely at the position of the sample [25, 31, 114] and (3) the combination of longer pulses with appropriate post-selection procedures such as energy filtering [24, 115].

Owing to its applicability for achieving ultimate spatio-temporal resolutions, this chapter of my thesis briefly describes the second strategy and explores the potential of all-optically generated and time-compressed few-electron probe pulses (see Fig. 3.1) for the implementation of ultrafast pump-probe diffraction experiments in terms of timing stability and achievable pulse duration. The special focus will be placed on the generation of electron probe pulses suitable for applications involving optically-induced collective electronic motion in nanostructures, whose key signatures include: (1) highly reversible processes, (2) a required spatial coherence length exceeding 100 nanometers (see Chapter 4), (3) very tiny diffraction angles (see Chapter 4) and (4) a desired temporal precision sufficient for resolving the electromagnetic near-field cycles (see Chapter 5). Our employed approach for electron pulse compression by all-optical means and with intrinsic time synchronization (see Fig. 3.1) harnesses the interaction of free electrons with the electromagnetic fields of approximately single-cycle THz radiation impinging on a thin metal film. Here, a single laser source is employed to drive the electron and THz generation processes in a synchronized and highly reproducible manner [31, 32].

## 3.2 Single-Electron Pulses and Ultrafast Electron Diffraction

The most decisive experimental parameters of studies targeting high-quality time-resolved microscopy and diffractive imaging applications are represented by the achievable spatio-temporal precision, durable measurement times and sufficient signal-to-noise ratio for unraveling the dynamics of interest emerging in microscopy images or Bragg spot positions and intensities, respectively. The ample possibilities offered by modern ultrafast transmission electron microscopes and table-top diffraction apparatuses allow for a precise adaption of these highly interlinked parameters to the specific requirements imposed by the intended investigation [67]. Under the assumption of available optical pulses optimized for triggering the respective process under exploration, the major limitations of optical-pump electron-probe approaches with respect to the achievable time resolution are imposed by the finite duration of the electron pulses and the accuracy of adjusting the pump-probe time delay. As complementary techniques, ultrafast microscopy and diffraction share the common pump-probe principle but work in slightly different domains with electron microscopy providing direct images of tiny volumes of matter while diffractive imaging is typically employed for investigating periodic samples such as crystalline structures in reciprocal space. Since the details underlying ultrafast electron microscopy and diffraction have already been discussed in literature [2, 18, 69, 116–118], the following paragraphs primarily aim for providing a comprehensible overview. The intentionally reduced complexity serves for highlighting the basic concepts and available tools for thoroughly characterizing the experimental setup (see Fig. 3.3 (a)), later applied for small-angle diffractive imaging of optically-excited nanoscale structures with sub-excitation-cycle time resolution (see Chapter 5).

### 3.2.1 Tabletop Apparatuses for Ultrafast Electron Diffraction

In ultrafast electron diffraction, as employed in the course of this thesis for studying periodic nanostructured arrays (see Chapter 4), electrons scattered by the material under examination interfere

coherently to form a far-field diffraction pattern on a phosphor screen, thereby revealing detailed structural information about the sample. A single high-quality diffraction pattern, visualizing a rich 2D set of multiple Bragg spots with sufficiently high signal-to-noise ratio to allow for extensive data analysis, typically contains around $10^6$ to $10^8$ electrons in total [18, 117, 119], depending on the sample's complexity. Here, the minimum measurement time of time-resolved experiments, comprising a series of diffraction patterns, additionally scales with the number of snapshots required to deliver the desired temporal resolution over the time window of interest. Considering a maximum feasible total acquisition time, primarily defined by the stability of the system, there is an on-going quest for reducing the acquisition time of individual diffraction patterns at a given signal-to-noise ratio in addition to optimizing the accessible time resolution by further shortening the pulse durations.

Tabletop ultrafast electron diffraction and microscopy systems typically rely on free electron pulses generated via the photoelectric effect by illuminating a photocathode with a train of laser pulses, whose photon energies slightly exceed the work function of the cathode's material [111]. Based on a design by the Fritz Haber Institute of the Max Planck Society in Berlin [59], a compact electron source was implemented in the course of this thesis in close collaboration with Dominik Ehberger [32]. This electron source employs a back-illuminated gold-coated sapphire cathode (see Fig. 3.1) with an applied electrostatic field to rapidly accelerate the generated electrons to energies of 75 keV towards the anode. While the category of flat photocathodes is a common choice for ultrafast electron-based setups, benefiting from a relatively small divergence of the generated electron beam and stable operation at moderately low pressure levels, alternative electron sources include tip-shaped photocathodes with nanoscale emission areas and promising coherence properties [118, 120]. To provide the necessary electron flux for high-quality diffraction experiments, there exist two opposing strategies for capturing snapshots of individual transient states of irreversible and reversible dynamics, respectively: (1) near-single-shot exposures with dense electron bunches [69, 117] or (2) averaging of multiple repetitive measurements obtained with few-electron pulses for each pump-probe time delay [2, 111].

### 3.2.2 Single-Electron Pulses for Ultimate Time Resolutions

For a long time, advancing the picosecond pulse durations of the first pioneering studies by Gérard Mourou and Steve Williamson [61] as well as the research group of Ahmed Zewail [121] towards the femtosecond or even attosecond regime have been hindered by space charge effects and insufficient pump-probe synchronization. The main obstacle for reaching ultimately short pulse durations with bright electron sources is represented by the repulsive action of Coulomb forces between electrons, which can substantially broaden the electron pulses in time, so that after covering the propagation distance to the sample their original duration can be exceeded by far [20]. Consequently, the detrimental effect of space charge typically implies a balancing act in ultrafast electron diffraction and microscopy experiments between: (1) minimum reachable pulse durations defining the temporal resolution and (2) sufficiently high electron flux for delivering the required signal-to-noise ratio. The detrimental impact of Coulomb repulsion can be alleviated by avoiding regions of high electron densities via a careful design of the applied electron imaging system in combination with a compact electron source with maximally reduced distances [20, 59]. However, space charge effects can never be fully eliminated and maintaining coherence, monochromaticity and sufficiently short pulse duration becomes increasingly challenging when upscaling the number of electrons per pulse [18].

Despite the risk of space-charge-induced distortions of single-shot diffraction patterns, the regime of dense electron bunches remains indispensable for examining irreversible processes such as melting [69],

not accessible with repetitive techniques unless the sample would be exchanged on a shot-by-shot basis. In contrast, the repetitive regime of single-electron or few-electron pulses [2,111], circumventing space charge broadening altogether, is designated for highly reversible processes such as electron dynamics and condensed-matter physics, for which the final diffraction pattern can build up sequentially from many individual scattering events. The high reversibility of light-driven collective electronic motion qualifies this regime for applications involving nanophotonics, as targeted in this thesis, with all the benefits that low-density electron pulses and their provided high temporal resolution imply.

The substantial reduction in electron flux that comes along with the lower number of electrons per pulse can, at least partially, be compensated for by maximizing the pump-probe repetition rate under the restrictions imposed by the relaxation time of the sample and by its damage threshold with respect to the optical pump pulses. Experimentally, laser-triggered electron emission from a flat cathode obeys Poissonian statistics [18] and the probability of having multiple electrons per pulse can be significantly suppressed by fine-tuning the incident laser intensity for gradually approaching the ultimate regime of single-electron pulses (see Fig. 3.3 (b)). For pump-probe diffraction experiments with single-electron wave packets, conventional experimental parameters such as electron pulse duration, beam diameter or divergence transform into concepts of statistical nature, resulting from the respective distributions obtained over multiple excitation and probing cycles [18]. In the end, for repetitive measurements it is the ensemble distribution of electron arrival times at the sample's position relative to the starting point of the optically-excited dynamics that determine the maximum accessible time resolution.

The absence of space charge broadening redirects the attention to the temporal profile of the laser pulses, which trigger the electron generation process in a nearly instantaneous fashion. Even though shortest optical pulse durations result in a minimized time window of photoelectron emission, they do not automatically imply the shortest possible electron pulses at the sample as a consequence of the time-bandwidth product [111]. Laser-generated photoelectrons emitted from the imperfect surfaces of real-world cathodes show statistical distributions of longitudinal velocities since any mismatch between the work function of the cathode's material and the spectral characteristics of the incident optical pulses, defined by the center wavelength and spectral bandwidth, directly transfers into a finite energy spread of the emitted electrons [111]. Sub-relativistic electron bunches, with a certain energy and corresponding velocity distribution, suffer from temporal broadening during acceleration and propagation since some electrons reach the sample position faster than others. Consequently, there exists a trade-off between optical pulse duration and spectral bandwidth when aiming for the shortest uncompressed few-electron pulse durations in UED experiments [111]. In summary, short uncompressed electron pulse durations rely on the minimization of dispersion effects by reducing the mismatch with the cathode's work function, by rapidly accelerating the electrons using high electrostatic fields and by shortening the distance $L$ from electron generation to the sample [18,111]:

$$\tau_{\mathrm{electron}} = \sqrt{\tau_{\mathrm{laser}}^2 + \tau_{\mathrm{acc}}^2 + \tau_{\mathrm{free}}^2} \approx \sqrt{\tau_{\mathrm{laser}}^2 + \frac{\sqrt{2}m}{(eE_{\mathrm{acc}})^2}\Delta E + \left(\frac{L}{v_{\mathrm{e}}(E)} - \frac{L}{v_{\mathrm{e}}(E+\Delta E)}\right)^2} \tag{3.1}$$

Here, $\tau_{\mathrm{laser}}$, $\tau_{\mathrm{acc}}$ and $\tau_{\mathrm{free}}$ represent three contributions, which define the final electron pulse duration $\tau_{\mathrm{electron}}$ and originate from the duration of the optical pulses, the temporal broadening of the generated electron pulses during acceleration and the subsequent dispersive effects during propagation towards the sample, respectively. $E_{\mathrm{acc}}$ is the electric field strength inside the electron source, $m$ is the electron mass, $e$ is the elementary charge, $\Delta E$ is the energy spread, $E$ is the average electron energy and $v_{\mathrm{e}}(E)$ is the energy-dependent velocity of the electrons.

### 3.2.3 Experimental Setup for Electron Pulse Generation

Taking these considerations into account, the experimental results presented in this thesis were obtained with a Yb:YAG laser source (Pharos, Light Conversion Inc.), operating at 50 kHz repetition rate and delivering pulses of 270 fs duration at a center wavelength of 1030 nm. A compact experimental setup, equipped with a computer-controlled optical delay stage, a beta barium borate (BBO) crystal for frequency-doubling the initial laser pulses and with units for precise power adjustment and focusing, was constructed. In this way, the emission of femtosecond few-electron pulses from our gold-coated cathode is triggered in a highly reproducible manner via two-photon absorption (see Fig. 3.3 (b)). The resulting energy spread, at an average electron energy of 75 keV after acceleration, amounts to approximately 1.3 eV [32]. The predicted duration of uncompressed electron pulses at the sample, installed 0.9 m behind the electron source, amounts to $\tau_{\text{electron}} \approx 500$ fs with the major contribution originating from temporal broadening during acceleration ($E_{\text{acc}} \approx 7$ MV/m). Thus, even in the absence of space charge, suitable wave-packet-compression techniques become indispensable for providing the temporal precision required for resolving optical cycles in light-matter interaction with our optical-pump electron-probe diffraction setup. As magnetic solenoids focus the beam in space, the electron pulses also have to be compressed in time to generate the shortest pulses at the position of the sample.

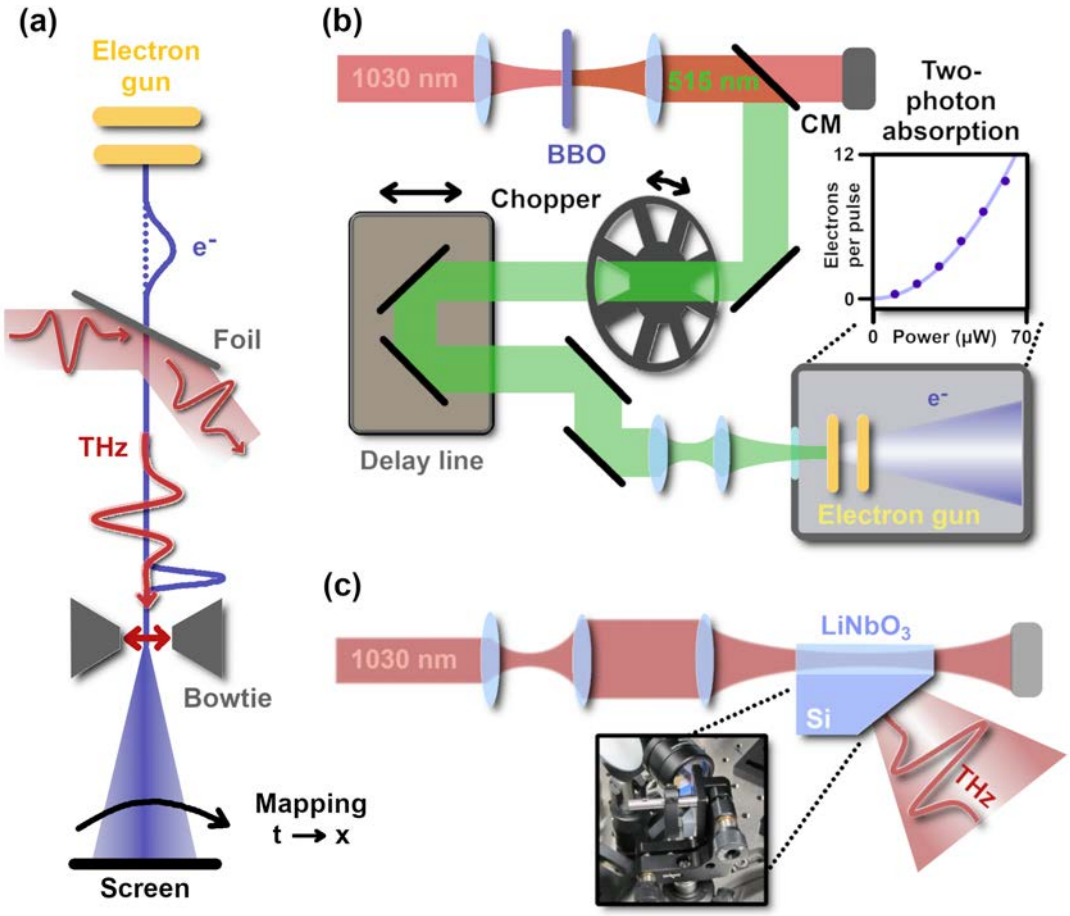


**Figure 3.3: Experimental setup for THz-based electron pulse compression and characterization.** **(a)** Diffraction setup with THz-compressed electron pulses (figure design adapted from [32]). **(b)** Laser-triggered photoemission of electron pulses via second harmonic generation (depicted power values at a wavelength of 515 nm) in combination with two-photon absorption at the cathode (measured data as dots; quadratic fit as solid line; more details also in [111]). **(c)** Cherenkov-style generation of single-cycle THz radiation from a slab-like $LiNbO_3$ crystal. A silicon prism serves as output coupler (details in [30]).

## 3.3 Characterization of Electron Probe Pulses

To evaluate the efficiency of electron pulse compression and to advance the temporal precision of electron diffraction and microscopy, an accurate and reliable tool for characterizing the temporal profile of compressed and uncompressed pulses alike at the position of the sample becomes indispensable. Previously reported techniques tackling the challenge of electron pulse characterization include streak cameras [122], energy analyzers [25] or ponderomotive scattering [123]. While the absorption of a photon by a free electron is prohibited in vacuum since energy and momentum conservation cannot be fulfilled simultaneously, the interaction with optical near fields confined to sub-wavelength dimensions can indeed result in a net deflection of the electron beam [31]. For example, the approximately homogeneous electric fields in the center of a resonantly-excited bowtie-shaped aperture in a metal foil can cause a global sideways deflection of transiting electrons as a function of arrival time [31], provided that a collinear geometry with perpendicular incidence of electrons and photons is used.

This sideways deflection predominantly occurs along the polarization direction of the optical radiation (see Fig. 3.3 (a)) whereas the longitudinal velocity of the electrons is left unaffected by the interaction. Given that the incident electron pulses have durations well below half the optical cycle, there exists a range of time delays offering a point-to-point correlation between the direction and amplitude of deflection and the arrival time of the electrons with respect to the optical excitation. Thus, the temporal profile of the electron pulse can be mapped onto a spatial coordinate, detectable by a phosphor-coated complementary metal-oxide-semiconductor (CMOS) camera. A scan of the optical-pump electron-probe time delay additionally reveals the optical response of the resonantly-illuminated bowtie [31]. For visualizing the optically-induced deflection in a single delay-dependent streaking trace (see Fig. 3.4 (a)), the information contained in the recorded sequence of delay-dependent 2D images is condensed by averaging the individual records along the direction perpendicular to the observed deflection.

### 3.3.1 Evaluation of the Electron Pulse Duration

An exemplary THz-induced streaking trace of uncompressed electron pulses, deflected by a resonantly-excited bowtie-shaped aperture, is depicted in the left panel of Fig. 3.4 (a). As long as the optically-excited apertures substantially exceed the spatial dimensions of the electron wave functions and the period of the optical cycles is much longer than the temporal coherence of the electrons, a classical description is sufficient for explaining the observed dynamics. In this regime, the wave nature of the electron beam largely remains invisible, the electrons can be approximated as point particles with respect to the optical waveform and the optically-induced deflection is determined by the Lorentz force [54]. The measured streaking traces visualize the resonant optical response of the bowtie convoluted with both, the static electron beam diameter on the CMOS camera and the temporal profile of the electron pulse. Consequently, the observed delay-dependent broadening and corresponding reduction in peak intensity show a clear dependence on the slope of the streaking curve and can be attributed to the finite duration of the uncompressed electron pulses. The longer the pulses, the more pronounced are such broadening effects (compare left and right panels of Fig. 3.4 (a)).

For electron pulse durations well below the excitation cycle, the streaking trace around the zero crossings shows an approximately linear behavior. Thus, the THz-induced spatial broadening of the line scan observed at these specific delays delivers an estimate of the electron pulse duration. Here, the slope of the streaking trace around these delays serves for calibrating the conversion between the arrival time of the electrons and the amplitude of the spatial deflection. Experimentally, the achievable

temporal streaking resolution is mainly determined by the ratio of the streaking amplitude, scaling with the incident THz-field strength, to the static electron beam diameter at the detector and additionally by the homogeneity of the electromagnetic near fields, which inflict the delay-dependent deflection on the electrons. By placing a circular aperture of 50 µm in diameter in front of the THz-excited bowtie resonator to reduce the extension of the electron beam, the region of electron-THz interaction gets confined to the very central part of the bowtie with its highly homogeneous electromagnetic field distribution [32]. Consequently, the temporal streaking resolution is enhanced but owing to the inserted aperture only at the expense of a reduced electron flux and therefore signal intensity.

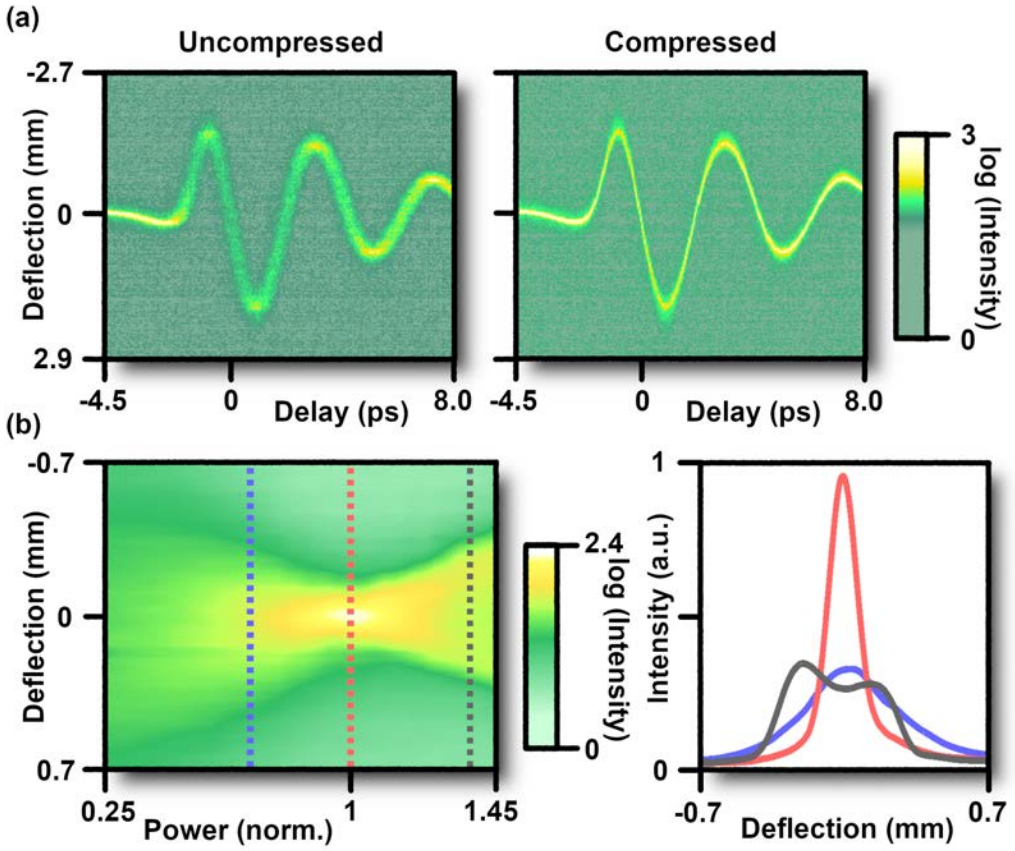


**Figure 3.4: Electron pulse compression and characterization by all-optical means.** **(a)** Time-resolved deflectograms obtained with a THz-excited bowtie-shaped aperture for uncompressed and time-compressed electron pulses, respectively. Spatial broadening effects around the zero crossings serve as an estimate for the electron pulse durations since these streaking curves visualize the convolution of the bowtie's optical response with the temporal profile of the electron pulse. **(b)** Optimization of the electron pulse compression by tuning the incident optical power for precisely adjusting the focus of the temporal lens and thereby to generate the shortest electron pulse durations (in red) at the position of the sample (figure design based on our publication [32]; color-coded dashed vertical lines in the left panel indicate the three extracted line scans depicted in the right panel).

Such streaking measurements fulfill all major requirements for determining the efficiency of the pulse-compression procedure, for including the stability of the system into the assessment and for defining the time resolution expected for subsequent UED experiments. This temporal characterization scheme can be applied to both compressed and uncompressed electron pulses alike. The measurement can be directly performed at the temporal focus of the compression element (see subsequent paragraphs) by exchanging the sample with a bowtie-shaped aperture. Moreover, the pump-probe timing stability can be examined simultaneously as long as the same excitation pulses, triggering the dynamics of interest in the UED experiment, are harnessed to induce the optical near fields in the bowtie resonator. Depending on the information of interest, such a measurement can therefore serve a three-folded

purpose: (1) to analyze the electron probe pulses, (2) to visualize the optical response of an unknown resonant structure or (3) to recover information about the optical pump pulses if well-characterized resonant structures together with sufficiently time-compressed electron pulses are employed.

### 3.3.2 Terahertz Generation via Optical Rectification

The electron pulse durations, intended to be applied and characterized in the experimental setup, set the parameters for the optimum choice of optical radiation. Long-wavelength terahertz and infrared radiation derived from a single ultrafast laser source typically follow the timing of the generating laser pulses with almost perfect temporal synchronization and are therefore ideally suited for manipulating laser-generated electron pulses in a highly reproducible way. Close to single-cycle terahertz pulses [30] can be generated in a well-controlled manner via laser-driven optical rectification in a slab-like lithium niobate ($LiNbO_3$) crystal (see Fig. 3.3 (c)), designed for enhanced sideways heat removal similar to thin-disk lasers. Here, the induced nonlinear polarization generates THz radiation in a Cherenkov-style fashion by matching the group velocity of the optical pump pulses with the phase velocity of the nearly single-cycle THz pulses [30]. With the THz electric field being locked to the envelope of the optical pump pulses, passive time synchronization in the UED experiment can be achieved by using a single ultrafast light source for both electron and THz generation. Additionally, the THz half-cycle durations and resonant structures in the low THz range match feasible spatio-temporal dimensions of sub-relativistic electron bunches, namely picoseconds and femtoseconds in time combined with millimeter and micrometer dimensions in space [31]. Therefore, two compact THz stages for electron pulse compression and characterization, respectively, were constructed and incorporated into our UED setup (see Fig. 3.3 (a)) in close collaboration with Dominik Ehberger in the course of this thesis.

## 3.4 Electron Pulse Compression at a Planar Mirror Surface

Optical near fields of resonantly-excited apertures are not only capable of deflecting electrons but also of accelerating and decelerating them for appropriate orientations and timing of the induced electric field components. Recapping the statistical temporal broadening of sub-relativistic few-electron pulses, resulting from close-to-linear vacuum dispersion effects and the associated accumulation of fast electrons in the leading part and of slow electrons in the trailing part of the pulse, implies that any electron pulse with an inverse spatial velocity distribution would self-compress after a certain distance of propagation. Actively inducing such an inversion by optical means [31,32] is exactly the strategy behind the approach for efficient temporal compression of few-electron pulses applied in this thesis. Other previously-reported techniques for improving the time resolution in electron diffraction and microscopy applications include energy-filtering [24], microwave cavities [25,119,124], time-stamping [26], optical gating [27], ponderomotive forces [28,29] and relativistic acceleration [125,126].

The desired time-dependent electron momentum modulation by optical means can be implemented via THz-excited resonators if tilted in such a way that there exists a non-vanishing projection of the enhanced and slowly-varying electric near fields onto the propagation direction of the electrons [31]. In this thesis, a more direct electron-THz interaction scheme (see our publication [32]) is employed with relaxed requirements with respect to the precise focusing and steering of the electron beam unavoidably linked to microscale resonators. A planar mirror surface, reflecting the THz radiation while being thin enough for sufficient electron penetration, serves as a symmetry-breaking surface and lets the electrons abruptly enter or exist the electromagnetic field. Thus, the interaction gets

truncated in a delay-dependent way before the accumulated effect would average out to zero and a delay-dependent electron momentum change is observed [32]. Again, the ratio of the electron pulse duration to the period of the optical field cycles defines the regime of operation. For electron pulse durations covering multiple optical cycles in the near-infrared range, a periodic energy modulation can be imprinted on the electrons [127,128] and trains of attosecond electron pulses can be generated and detected [108,129]. Once the period of the optical cycle is increased to substantially exceed the initial electron pulse duration, the entire electron pulse can become subject to a monotonic, almost linear momentum modulation for an appropriate range of delays, so that under optimized conditions vacuum dispersion can be compensated for and isolated sub-100-fs electron pulses can be generated [32].

### 3.4.1 Electron Pulse Compression at Velocity-Matching Condition

A delay-dependent momentum modulation is imprinted homogeneously over the entire spatial profile of extended electron beams for suitable combinations of electron and THz angles of incidence [32]:

$$c \cdot sin(\alpha_e) = v_e \cdot sin(\alpha_{THz}) \tag{3.2}$$

where $c$ is the speed of light, $v_e$ is the electron velocity and $\alpha_{THz}$ and $\alpha_e$ are the incident angles of the THz and electron pulses onto the mirror surface, respectively. By appropriately adjusting the timing, the focusing conditions and in particular the Gouy phase of the long-wavelength THz radiation, impinging on the compression element, the approximately linear momentum modulation required for efficient electron pulse compression can be generated [32]. Conveniently, the velocity-matching condition for a planar mirror surface (see Eq. (3.2)) does not only provide spatially-uniform longitudinal momentum transfer and therefore ideal conditions for efficient electron pulse compression but it additionally coincides with the absence of any transverse deflection [32,130]. Thus, non-tilted electron pulses can be generated without altering the propagation direction of the electron beam [130], which substantially facilitates the operation and optimization of the UED setup. By precisely adjusting this longitudinal momentum transfer, the initial dispersion-induced velocity distribution of the electron pulse can get inverted so that the pulse will self-compress in time during the propagation to the sample [25].

For linear dispersion effects, the conservation of phase-space volume implies that shortening of the electron pulse duration can only be achieved at the expense of an increase in energy bandwidth [25]. In particular, electron pulses can be generated at the sample's position with pulse durations even below the duration of the initializing laser pulses. However, the energy spread should not be arbitrarily increased since a sufficiently high degree of monochromaticity is required to enable distortion-free acquisitions of diffraction patterns with time-compressed electron pulses. Typically, the initial energy spread of few-electron pulses, delivered by planar femtosecond photocathodes and accelerated to energies of 75 keV, only amounts to approximately 1 eV [32]. Consequently, there is still ample room for additional spectral broadening as a result of the applied pulse compression scheme and the degree of monochromaticity of time-compressed electron pulses approaches the one obtained with conventional electron microscopes, but with all the benefits that femtosecond pulse durations imply [18].

### 3.4.2 Experimental Implementation of Electron Pulse Compression

In summary, the applied optical-pump electron-probe diffraction setup (see Fig. 3.3 (a))) comprises three stages in total: (1) for electron generation via second harmonic generation and two-photon

absorption, (2) for optical rectification and THz-based electron pulse compression at a planar mirror membrane and (3) for sample excitation and electron pulse characterization via THz-induced spatial deflection, all driven by a single femtosecond laser source for intrinsic passive synchronization. While only a minor portion of the laser power is harnessed for electron pulse generation (see Fig. 3.3 (b))), pump powers of approximately 3 W and 12 W drive the Cherenkov-style stages, generating close to single-cycle THz pulses required for electron pulse compression and sample excitation, respectively. In this prototype ultrafast diffraction setup, the THz-based compression element takes on the role of chirped mirrors in optical systems while magnetic solenoids serve for focusing the electron beam on the phosphor-coated CMOS camera installed at the end of the beam line. The successful experimental implementation and optimization of a back-illuminated electron source in combination with THz-based electron pulse compression at a symmetry-breaking surface was performed in the course of this thesis in close collaboration with Dominik Ehberger and a more detailed description is provided in our corresponding publication by Ehberger et al. [32]. Therefore, the following paragraphs just summarize the most important experimental results with respect to the intended application of examining the optical response of nanostructures via pump-probe ultrafast electron diffraction (see Chapter 5).

For the data presented in this thesis, electron pulse compression is implemented via intersecting the THz beam and the electron beam at an angle of approximately 90° on the planar compression element. By gradually increasing the incident THz power and monitoring the profile of the electron beam at the zero crossing of the streaking curve, it can be visualized clearly that the single electron pulses first become shorter and shorter in time and reach a minimum pulse duration at around a field strength of 3 kV/cm (normalized to unity in Fig. 3.4 (b)) before, at higher compressor field strength, the electron pulse duration starts to increase again [32]. As previously described, a first estimate of the electron pulse duration can be obtained from the THz-induced spatial broadening by employing the approximately linear slope of the streaking curve (see Figs. 3.4 (a)) around the zero crossing in order to map the measured deflection back to the original arrival times of the electrons. A more detailed analysis with an additional deconvolution step, removing the contribution of the static electron beam profile on the camera (for more details please refer to our publication [32]), yields electron pulse durations as short as 28 fs (FWHM) for our experimental setup. This value is approximately 17 times shorter than the uncompressed pulse durations of 490 fs measured at the position of the sample [32].

## 3.5 Timing Stability of Ultrafast Single-Electron Diffraction

The average electron energies of 75 keV selected in this thesis represent a compromise between: (1) the spatio-temporal resolutions offered by the generated electron pulses and (2) the small diffraction angles emerging for nanoscale structures (see Chapter 4). Lower electron energies benefit from larger diffraction angles while efficient electron pulse compression, however, is more challenging [32] and the penetration through the underlying substrate of the sample is reduced. Besides, the detrimental impact of stray magnetic fields on the electron trajectories and consequently on the spatial precision is more severe. Higher electron energies can alleviate effects from space charge and stray magnetic fields but only at the cost of smaller diffraction angles, reduced focusing capabilities of magnetic solenoid lenses and a lower sensitivity to the nanoscale electromagnetic near fields under investigation in the time-resolved study (see Chapters 5 and 6). To elucidate the experimentally achievable time resolution and to evaluate the potential of all-optically generated and compressed electron pulses for the implementation of the intended repetitive optical-pump electron-probe application, namely ultrafast electron diffraction of THz-excited nanostructures, a thorough characterization of jitter and

drift effects is required (see also our publication [32]). In ultrafast electron diffraction with all-optically compressed electron pulses, residual timing fluctuations can emerge from instabilities of the electric fields applied for accelerating the electrons. Additional detrimental effects may originate from pointing variations of the laser beam driving the optical rectification process and leading to timing errors of the generated single-cycle terahertz radiation. As depicted in Fig. 3.5, all of the timing fluctuations occurring on experimentally relevant time scales are on the level of a few femtoseconds with negligible systematic timing drifts and therefore clearly smaller than the electron pulse duration.

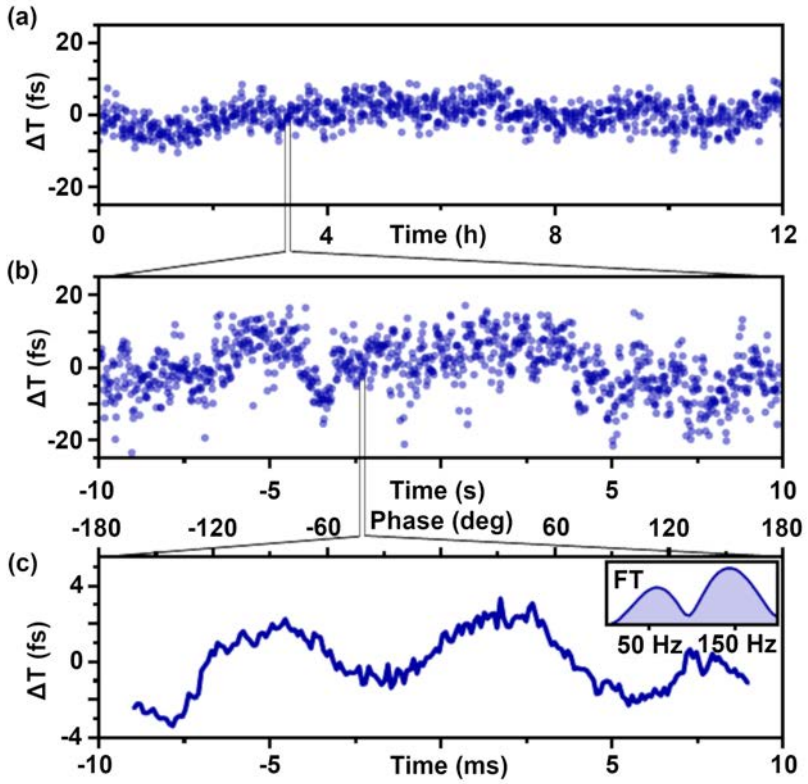


**Figure 3.5: Timing stability of all-optical-based ultrafast electron diffraction dispensing with any kind of active stabilization scheme. (a)** Long-term fluctuations amount to 3.7 fs (rms) without any noticeable systematic timing drifts over 12 h. **(b)** Short-term jitter of 7.5 fs (rms) on average is clearly smaller than the electron pulse duration. **(c)** Electronically-driven capacitor plates, installed behind the sample and locked to the 50-Hz laboratory mains, deflect the electron beam and uncover systematic timing errors occurring on millisecond time scales. The Fourier analysis (FT) is depicted in the inset. (Figure reproduced from our publication [32])

## 3.6 Characterization of Terahertz Pump Pulses

An all-embracing characterization of the optical-pump electron-probe diffraction setup further requires information about the THz pump pulses, which can either be retrieved from additional electro-optic sampling measurements [30] or from the measured global deflections of the three mesoscopic resonators depicted in Fig. 3.6. Finite-difference time-domain (FDTD) calculations (Lumerical; all on micrometer dimensions) for a bowtie-shaped aperture, the nanostructured sample including its mesoscopic support structures and an empty transmission electron microscopy (TEM) grid numerically predict the electromagnetic fields. A custom MATLAB script determines the accumulated transverse momentum transfer, imprinted on the electrons when propagating along straight trajectories through the optically-induced, rapidly-oscillating electromagnetic near fields [67]. Following the interaction with the THz fields, the transverse momentum transfer maps into a sideways deflection of the electron

beam during the propagation towards the phosphor-coated camera. In contrast to the highly resonant excitation of the bowtie-shaped aperture, optimized for electron pulse characterization via THz-induced streaking, the ringing in the 2D deflectograms of the TEM-grid-based structures is much less pronounced, indicating that the applied THz frequency is far off resonance for these two samples. While the experimental curves (black) are extracted from the 2D streaking data via Gaussian fits, applied independently for each of the captured THz-electron time delays, a global fit of the incoming terahertz waveform under variation of its optical parameters, namely the central frequency, pulse duration and carrier-envelope phase, produces the theoretically derived deflections depicted in Fig. 3.6 (b-d) (green) [67]. This global fit yields a cosine-shaped, single-cycle THz pulse in accordance with the THz waveform retrieved from electro-optic sampling for a comparable experimental setting [30].

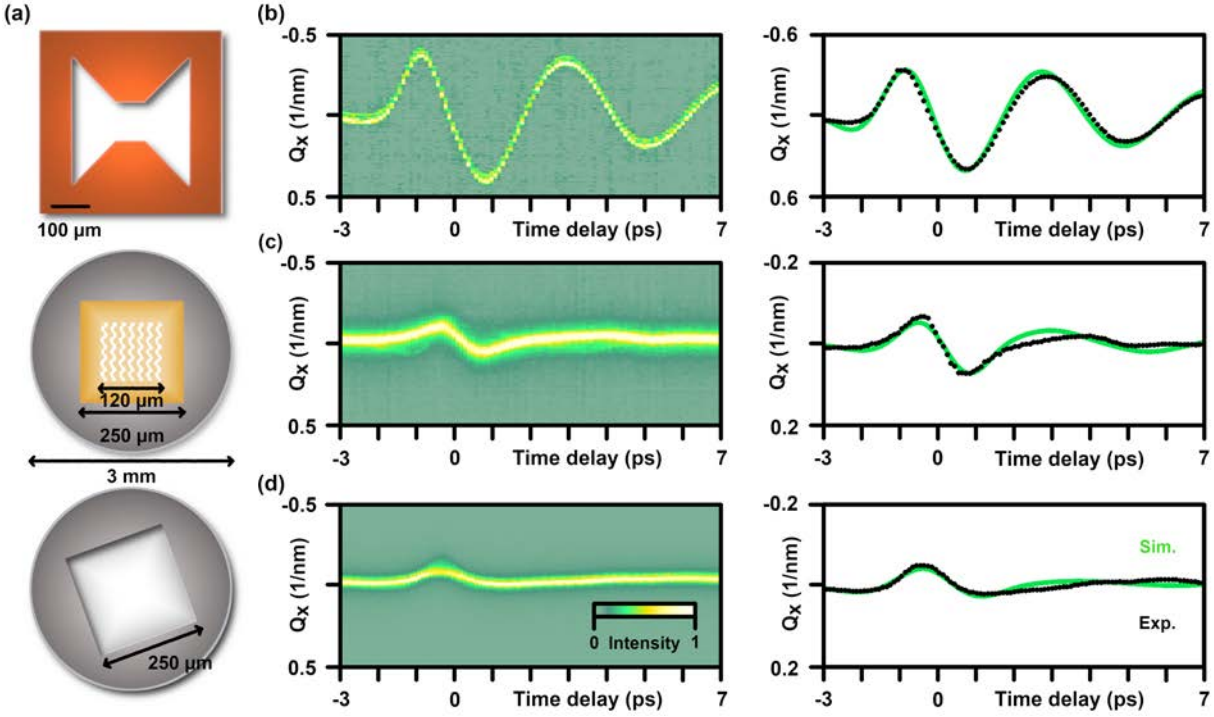


**Figure 3.6: Observation of mesoscopic resonances via global deflections of sub-100-fs electron pulses for characterizing the incident terahertz waveform.** A selection of three mesoscopic structures under investigation **(a)** and their measured dynamics under THz excitation are depicted. The respective delay-dependent deflections of the electron beam (black dots) are extracted from the measured streaking traces of **(b)** a bowtie resonator, **(c)** the nanostructured sample including its mesoscopic support structures, which is closely examined in Chapters 4 to 6, and **(d)** an empty transmission electron microscopy (TEM) grid for comparison. Numerical finite-difference time-domain (FDTD) calculations, performed on micrometer dimensions and evaluating the propagation of the electrons through the induced electromagnetic fields, are depicted as green lines. The underlying global fit of the theoretical results, obtained for the three different mesoscopic resonances, yields a satisfying agreement with the experimental results and further serves for characterizing the incoming terahertz waveform. (Figure design inspired by Mohler et al. [67]; units of the vertical axes chosen in accordance with the static diffraction patterns in Chapter 4)

In summary, the successful implementation of electron pulse compression at a symmetry-breaking membrane resulting in sub-100-fs few-electron pulses, the achieved timing stability on the level of a few femtoseconds and the presented tools for THz and electron pulse characterization provide a clear perspective for ultrafast diffraction experiments with THz-compressed electron probe pulses to study light-matter interactions on their intrinsic time scales, the cycles of light. Since sub-excitation-cycle time resolution is only half the story when aiming for high-precision imaging in space and time, the next chapter of my thesis will explore the achievable spatial resolution in static settings before proceeding to the corresponding study of THz-induced dynamics in nanophotonic materials.

# 4

# Static Electron Nanodiffraction

*"The electron can no longer be conceived as a single, small granule of electricity; it must be associated with a wave, and this wave is no myth; its wavelength can be measured and its interferences predicted."*

*– quote by Louis de Broglie*

The presented terahertz-based schemes for delivering time-compressed sub-100-fs electron pulses (see Chapter 3), including the characterization of their temporal profiles via optically-induced deflections of the electron beam, can be correctly described in the limit of a point-particle approximation with classical electron trajectories and terahertz-electron interactions governed by the Lorentz force [130]. This classical description of the underlying dynamics is justified since the spatio-temporal coherence properties of the electron beam largely remain invisible on microscopic length scales as well as for a temporal coherence of the electron beam that is substantially smaller than a terahertz (THz) cycle period [67]. When proceeding towards applications of electron interferometry on nanometer or atomic dimensions, however, it becomes of vital importance to consider the quantum nature of free electrons and their wave-like behavior, which may emerge for appropriate experimental conditions. The interferometric nature of diffraction experiments (see Fig. 4.1) necessitates a quantum mechanical description with delocalized electrons beyond a classical point-particle approximation because the mere existence of Bragg spots requires interference of coherent electron de Broglie waves and knowledge about the amplitude and phase of the electron wave function to predict the interference pattern [67].

The wave-particle duality of light and matter [48, 131, 132] has intrigued physicists for many decades by now. On the one hand, the wave-like characteristics of optical radiation are clearly captured by Huygens–Fresnel principle, providing a conceptual understanding of the propagation, diffraction and interference of light, or by Thomas Young's famous double slit experiment in 1801 [131]. On the other hand, Albert Einstein's photo effect [132], as harnessed in our ultrafast electron source [59], serves as an explicit example demonstrating that, during its interaction with matter, light can also very much act like a composition of individual particles with quantized momentum and energy. In 1924, Louis de Broglie extended the conception of wave-particle duality from optical radiation to elementary particles by associating electrons with an energy-dependent wavelength $\lambda = h/p$ [48], where $h$ stands for the Planck constant and $p$ for the electron momentum. Typical electron energies harnessed in transmission electron microscopy and diffractive imaging range from 30 keV to 300 keV, which implies sub-atomic-scale de Broglie wavelengths covering the span from 7 pm down to 2 pm [18].

Experimental evidence for Louis de Broglie's landmark postulate of wave-like properties of matter followed quickly: Only approximately four years later, Clinton Davisson and Lester Germer successfully demonstrated diffraction of electrons at a nickel crystal [45] and independently George Paget Thomson and Alexander Reid observed scattering of cathode rays at thin films [49]. In 1956, Gottfried Möllenstedt and Heinrich Düker [133] investigated electron interference phenomena by employing

a very thin conducting wire as an electron biprism, nowadays commonly applied in electron holography settings [64,65]. Several years later Claus Jönsson [134] finally complemented Thomas Young's original investigations with optical radiation by performing the first actual double-slit experiment with electrons. Meanwhile, electron diffraction has turned into an indispensable tool for material science, whereby the whole family of electron-based techniques, including electron microscopy [109], low-energy electron diffraction [135] and electron holography [64, 65], share the benefits of the high spatial resolution offered by the picometer-scale and energy-dependent de Broglie wavelengths of sub-relativistic electrons. Targeting slightly different domains, electron microscopy can provide direct images of tiny volumes of matter while diffractive imaging is typically employed for investigating periodic samples such as crystalline structures in reciprocal space. Another interesting category of materials, besides crystals, to be studied via electron diffraction is represented by the recently emerging family of metamaterials [136–138]. As artificially engineered materials, they are capable of generating intriguing novel optical effects, not realizable with conventional materials.

## 4.1 Electron Diffraction and Nanophotonic Materials

Metamaterials [136–138] gain their novel and unprecedented functionalities from the carefully designed shape and periodic arrangement of tiny building blocks, which manipulate impinging electromagnetic waves in a well-defined manner on a sub-wavelength scale.

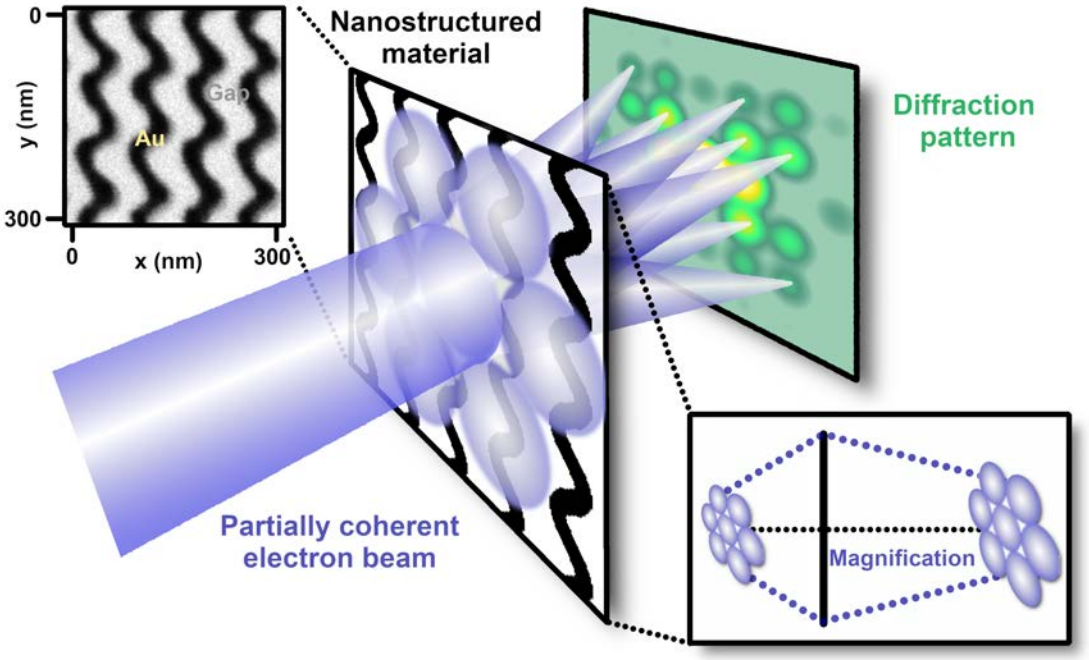


**Figure 4.1: Static diffraction of a partially coherent electron beam at a 2D nanostructured material.** The material under investigation consists of a periodic arrangement of wavy metal nanostructures (black), which block the electrons (blue) while the gaps between the nanoscale elements allow for electron transmission. The transverse coherence length (illustrated as circles) of the partially coherent electron beam can be increased by magnifying the beam diameter at the position of the sample with a magnetic solenoid lens (black line in inset on the right) installed after the electron source. Once the transverse coherence length exceeds the size of the unit cells, the transmitted de Broglie waves start to interfere coherently leading to the appearance of a 2D diffraction pattern (green) on the phosphor-coated camera.

Harnessing the precisely tailored imprint of spatially-dependent amplitudes, phases and polarizations onto the electromagnetic field cycles on sub-wavelength dimensions, previously reported exceptional

optical responses delivered by metamaterials, including cloaking devices [71], negative refraction [139] and flat lenses [72], have paved the way for innovative imaging and sensing applications with nanoscale and lightweight optics [67]. The typical nanoscale structure of metamaterials, however, imposes challenging demands on the resolutions, required simultaneously in space and time for thoroughly characterizing a nanophotonic material's functionality from a fundamental perspective and analyzing the induced nanoscale electrodynamic near fields with sub-wavelength and sub-excitation-cycle precision [67]. Even for relatively large wavelengths in the THz range interacting with nanostructures, spatial and temporal resolutions on the scale of nanometers and sub-picoseconds are required simultaneously. The far-field interaction of optical radiation with metamaterials typically resembles the one with a uniform, continuous medium concealing its sub-wavelength-scale architecture [140], whereas the substantially shorter de Broglie wavelength of sub-relativistic electrons impinging on a nanostructured material causes them to scatter off the individual building blocks and thereby to reveal their explicit shape and periodic arrangement. Besides, electron pulses with sub-100-fs duration can now be reliably generated using THz-based electron-pulse-compression schemes [32], as described in Chapter 3, and can therefore serve as valuable probes for investigating ultrafast dynamics in matter.

The typically periodic arrangement of sub-wavelength-scale elements, the high reversibility of light-driven collective electronic motion and the high sensitivity of the electron charge to electromagnetic fields render ultrafast pump-probe electron diffraction in transmission geometry a very promising approach for investigating the fundamental electrodynamics, underlying the exceptional functionality of metamaterials and nanophotonic devices. To elucidate the prospects of these desired time-resolved experimental investigations of optically-excited nanostructured materials with femtosecond electron pulses, this preparatory chapter first addresses the major challenges generally involved with static electron nanodiffraction (see Fig. 4.1) at electron energies of 75 keV, where diffraction angles are tiny, the partial coherence of the electron beam imposes substantial constraints on the visibility of the diffraction pattern and the compensation for stray magnetic fields becomes indispensable.

## 4.2 Sample Design and Fabrication

Complying with typical dimensions of optical metamaterials and mimicking a field-enhancing nanostructure for nonlinear optics, a two-dimensional array of periodically-arranged wavy metal nanostructures was printed via electron beam lithography on a dielectric substrate for this study (see Fig. 4.2(a-c)). Our sample (see also Mohler et al. [67]) resembles a grid of linear wires but, owing to the additional local curvatures, a pronounced 2D diffraction pattern with slightly different diagonal Bragg spot intensities emerges, given a sufficiently large transverse coherence length of the electron beam. The wavy structures (see Fig. 4.2(c)) were fabricated at the University of Regensburg via electron beam lithography in the center of a silicon nitride membrane (thickness of 50 nm, Pelco, Plano GmbH) using a Zeiss Supra 40 electron microscope with a Nanonic lithography unit, which operates at an acceleration voltage of 30 kV [67]. A high positive electron-beam resist was applied to the sample by spin coating. After resist development, the generated mask was annealed at a temperature of 90 °C on a hot plate. Subsequently, a titanium adhesion layer with a thickness of 5 nm and a gold layer with a thickness of 25 nm were deposited by physical vapor deposition before lift-off was performed using acetone [67]. The structured area measures 120 µm × 120 µm with an individual unit cell size of 82 nm × 100 nm. A solid gold frame (250 µm × 250 µm) covers the outer, unstructured part of the window (see Fig. 4.2 (a)) to block the electron beam outside of the nanostructured area, which fulfills an essential requirement for achieving a sufficiently high signal-to-noise ratio for the higher-order Bragg spots.

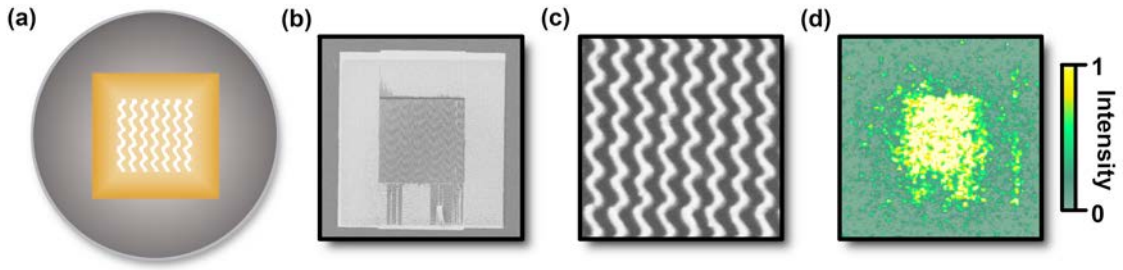


**Figure 4.2: Wavy nanostructures as prototype sample for small-angle diffraction with femtosecond electron pulses.** **(a)** Design of the nanostructured sample including its surrounding support structures. **(b)** SEM image visualizing the wavy gold structures extending over the central area of 120 µm × 120 µm together with a solid gold frame (250 µm × 250 µm) covering the outer, unstructured part of the window. **(c)** Close-up view of the nanostructures with an individual unit cell size of 82 nm × 100 nm. **(d)** Shadow image of the sample installed in our UED beam line clearly demonstrating that the support structures substantially suppress the transmission of electrons outside of the nanostructured area.

## 4.3 Transverse Coherence Length of the Electron Beam

As the contrast arising from constructive and destructive interference provides the basis of all diffraction experiments, the spatio-temporal coherence properties of the electron beam have a fundamental impact on the visibility of Bragg spots. Coherent interference of scattered de Broglie waves and the appearance of a far-field diffraction pattern are typically observed for experimental settings, in which the dimensions of the unit cells are roughly on the same order as the de Broglie wavelength. The diffraction experiments targeted with this thesis, however, work in a completely different regime with the combination of our femtosecond electron pulses at electron energies of 75 keV and unit cell sizes of approximately 100 nm, which is comparable to sending a laser beam in the visible frequency range towards a centimeter-scale grating (see Fig. 4.3). The two major requirements for observing a pronounced diffraction pattern in this unusual regime are represented by: (1) a sufficiently large transverse coherence length, allowing for coherent illumination and interference over more than one unit cell as well as (2) by an appropriate detection scheme for resolving the tiny diffraction angles.

For establishing an optical analogy, a highly coherent laser beam in the visible range is expanded by a telescope to a beam diameter of ~10 cm, illuminating a 2D array of periodically-arranged centimeter-scale apertures (see Fig. 4.3 (a)). The diffracted light is subsequently focused by a second telescope on a screen, installed at a distance of approximately 2 m behind the sample in order to spatially separate the individual Bragg spots and to yield the optical diffraction patterns depicted in Fig. 4.3 (b-f). By gradually adjusting the imaging settings of the second telescope, a whole series of near-field Fresnel and far-field Fraunhofer diffraction patterns can sequentially be projected onto the screen. Although the laser wavelength is >40,000 times smaller than the size of the unit cells comprising the sample, rich 2D diffraction patterns of more than 20 diffraction orders can be captured successfully. Corresponding theoretical results are displayed in the bottom row of Fig. 4.3 for comparison. Here, the periodic arrangement and geometry of the apertures comprising the sample are accounted for by a structure-specific absorption mask [51]. The finite transverse coherence length of the laser beam is modeled as a Gaussian distribution. Subsequently, the generated absorption mask is multiplied with the Gaussian distribution and the absolute square of its Fourier transform yields the depicted far-field diffraction patterns. In diffraction, the finite transverse coherence length manifests itself as the so-called point spread function leading to broadening of the Bragg spots whereas the shape of the unit cell determines the envelope of the diffraction pattern. The satisfying overall agreement between experimentally observed diffraction patterns and the theoretical predictions underlines the general

validity of this simple theoretical picture. The residual minor deviations are attributed to uncertainties in accurately reproducing the explicit shape and actual 2D arrangement of the real-world apertures.

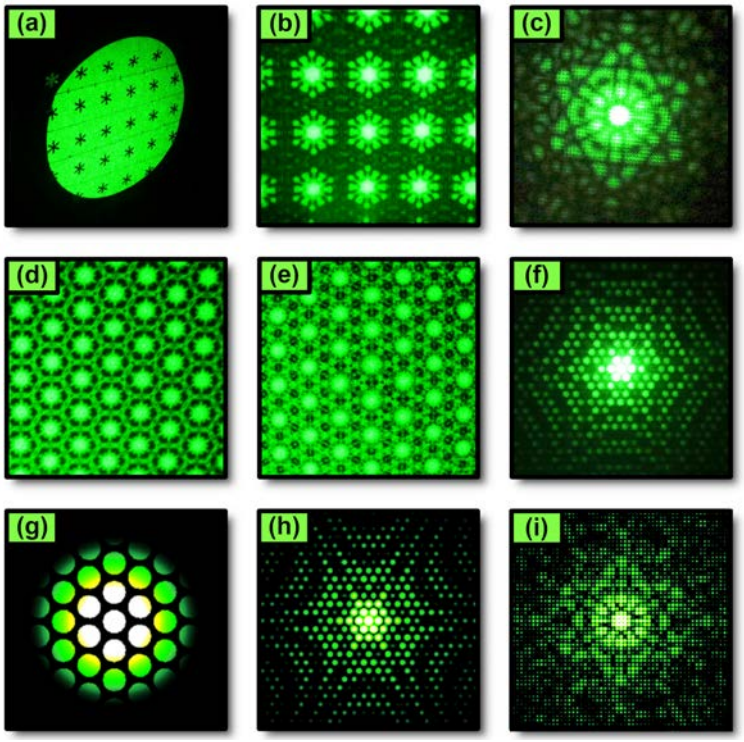


**Figure 4.3: Optical Fresnel and Fraunhofer diffraction of macroscale periodic structures.** Photographs depicting the periodic arrangement of centimeter-scale, snowflake-shaped apertures illuminated by a highly coherent, largely magnified laser beam (green) **(a)** and its corresponding Fresnel **(b)** and Fraunhofer diffraction patterns **(c)**. Near-field Fresnel diffraction **(d-e)** and far-field Fraunhofer diffraction **(f)** for a hexagonal pattern of circular apertures. Theoretical model of the illuminated sample **(g)**, accounting for the transverse coherence length of the optical radiation as well as the periodically structured absorption mask, and its simulated far-field diffraction pattern **(h)**. Theoretically calculated Fraunhofer diffraction pattern of snowflake-shaped apertures **(i)**. Original idea for the optical setup provided by Prof. Dr. Theodor Hänsch; Experimental implementation for this thesis and the optics lectures at the University of Konstanz performed in collaboration with Johannes Thurner.

This optical system provides a very convenient tool for determining the most decisive parameters and for closely examining the impact of possible real-world imperfections on the quality of the achievable interference pattern. The obtained conclusions can directly be transferred to electron diffraction, with the difference, however, that the electron beam is characterized by a partial transverse coherence, which is limited by the emittance of the electron source [141]. In other words, the transverse coherence of few-electron pulses delivered by flat photocathodes is determined by the source size at the cathode and the transverse velocity spread of the electron beam [141]. Typically, the beam quality is much worse than in the optical case even though the suppression of Coulomb repulsion effects for few-electron pulses results in a comparatively low transverse velocity spread. Moreover, the electron emission area can be reduced to micrometer scales since image charge effects, potentially preventing the escaping of photoelectrons from the cathode's surface, can be largely neglected for low density electron pulses [141]. As the low-density electron beam propagates through the beam line towards the sample, the ratio of the spatial coherence length to the beam diameter is conserved [141].

Consequently, the transverse coherence length in electron diffraction experiments, in analogy to the presented optical results, can be increased by expanding the electron beam diameter until multiple unit cells are covered coherently at the sample. However, nanostructured samples, comprising of millions of individual building blocks, can typically not be manufactured with sufficiently high quality

over arbitrary dimensions. Once the electron beam diameter exceeds the finite size of the sample, additional magnification of the transverse coherence length can only be achieved at the expense of a reduction in electron flux [141], which decreases the obtainable signal-to-noise ratio and represents one of the major experimental challenges in the employed single-electron regime.

In the experimental configuration applied in this thesis (see also Mohler et al. [67]), electron pulses at an energy of 75 keV are generated via femtosecond two-photon photoemission from an optical focal spot of approximately 5 µm in diameter and electron beam expansion delivers a diameter of approximately 2 mm at the position of the sample, which equals to a transverse coherence length of around 100 nm (full width at half maximum) matching the size of the repeating unit cells. In simulations, the partially-coherent electron beam (see Fig. 4.1) can be modeled as an incoherent ensemble of coherent single-electron wave packets impinging on the sample with random displacements with respect to the unit cells under investigation [67]. Consequently, the Gaussian distribution, accounting for the finite spatial coherence as already discussed for the optical setting, has to be gradually moved over the nanostructures while calculating the incoherent sum of the generated diffraction patterns.

## 4.4 Compensation for Stray Magnetic Fields

The two major objectives of static electron diffraction measurements with femtosecond electron pulses are given by: (1) a first quality assessment of the periodicity and shape of the nanoscale building blocks under investigation and (2) the supply of a reference measurement at sufficiently high signal-to-noise ratio for detecting THz-induced Bragg spot dynamics in the intended time-resolved study. Due to the unusually high electron energies for electron nanodiffraction [51], precise alignment, focusing and compensation for 50-Hz noise become inevitable for successful data acquisition. Owing to the picometer-scale de Broglie wavelengths of our 75-keV femtosecond electron pulses, diffraction angles for 100-nm unit cells are tiny and the spacing between the diffraction orders is just slightly larger than the camera resolution of 15.6 µm, installed approximately 1 m behind the position of the sample.

To capture the fine details of the small-angle diffraction patterns, magnetic stray fields in the laboratory have to be compensated for efficiently [67]. Slow drifts are tackled by Helmholtz coils (Macom, Müller BBM Gmbh) while fast magnetic field oscillations, originating from the laboratory mains, are counteracted by a pair of electrostatic deflection plates (designed by Ann-Kathrin Raab and Dominik Ehberger [142]), which are installed directly behind the sample and split the diffraction patterns in a step-wise manner into 8 or 10 separate copies in synchrony to the 50-Hz period of the laboratory voltage (see Fig. 4.4). A periodically applied voltage ramp, replacing the step-wise mode, can reveal the undesired deflections of the electron beam induced by fast magnetic field oscillations. With these deflections clearly exceeding the width of the point spread function and even the Bragg spot spacing, means to compensate for the impact of magnetic field oscillations become indispensable for observing a clear and undistorted diffraction pattern of nanostructures with our femtosecond electron pulses.

For direct applicability to the intended time-resolved studies, the step-wise deflection is implemented along the direction perpendicular to the terahertz-induced deflection (see Fig. 4.4). In post-processing, the individual images are superimposed with the help of Gaussian fits and thus produce diffraction patterns that approach the maximum sharpness allowed by the transverse coherence of the electron beam [67]. In contrast to placing an optical chopper with a 10% opening angle in the gun excitation path (see Fig. 3.3), the application of the capacitor plates allows for restoring diffraction patterns with substantially improved signal-to-noise ratio based on an effective duty cycle of up to 100%.

Additionally, interpolation via zero-padding can be applied to artificially increase the spatial precision beyond the camera's resolution and to improve relative alignment before averaging multiple data sets.

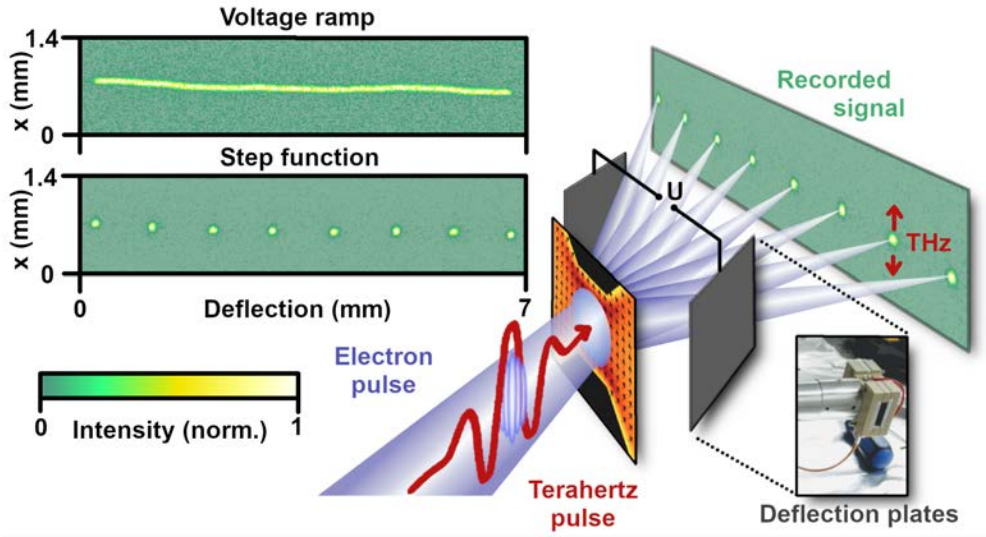


**Figure 4.4: Compensation for stray magnetic fields via a pair of electrostatic deflection plates installed directly behind the sample and operated in synchrony to the 50-Hz period of the laboratory voltage.** The pair of aluminum plates (inset) is surrounded by an insulating support structure and can reliably be operated at voltages of up to 2.5 kV. The periodic application of a voltage ramp enables the visualization and assessment of the 50-Hz magnetic field oscillations, originating from the laboratory mains and leading to undesired deflections of the electrons (blue) exceeding the Bragg spot spacing. The detrimental influence on the sharpness of the captured Bragg spots can be minimized by splitting the electron beam in a step-wise manner, in synchrony to the 50-Hz period of the laboratory voltage and in the direction perpendicular to the THz-induced deflection into 8 or 10 separate copies. For illustrating the applied geometry, the THz pulse (red) and the induced near-fields (black arrows) are depicted additionally.

## 4.5 Static Small-Angle Electron Diffraction

Taking all these considerations into account, static small-angle diffraction data (see Fig. 4.5) of a wavy nanostructured array (see Fig. 4.2) is obtained with femtosecond few-electron pulses. Complying with the optical analogy provided in the previous paragraphs, the electron de Broglie wavelength of 4.3 pm at 75 keV central energy is >20,000 times smaller than the unit cell of the wavy metal structures (82 nm x 100 nm) resulting in tiny diffraction angles below 0.1 mrad. The intrinsic transverse coherence of few-electron pulses allows for coherent interference over multiple unit cells and consequently for the observation of a 2D set of pronounced Bragg spots up to the $4^{th}$ order (see also Mohler et al. [67]) as long as the detrimental effects of stray magnetic fields are efficiently compensated for. The number of detectable Bragg spots is limited by the envelope of the diffraction pattern, the finite transverse coherence of the electron beam and the signal-to-noise ratio. The ratio of the direct beam intensity to the higher-order contributions is influenced by the electron transmission ratio of the nanoscale architecture. Assuming a given dynamic range of the camera, it is of key importance to avoid saturation by the direct beam to guarantee unambiguous detection of the adjacent higher-order peaks. To increase the signal-to-noise ratio, the recorded static diffraction data in Fig. 4.5 (a) is symmetrized in post-processing by harnessing the typical centrosymmetric characteristics of static electron diffraction patterns as the absolute square of the Fourier transformation of a real-valued object [67].

The Bragg spots are labeled by Miller indices ($hk$), where $h$ and $k$ are integer numbers. A third Miller index is omitted because our 2D array of wavy nanostructures is not periodic in $z$ direction and the

respective reciprocal space therefore crosses the Ewald sphere at no particular Laue zone [67]. The experimentally obtained small-angle diffraction (see Fig. 4.5 (a)) shows a high level of agreement with the theoretical pattern (see Fig. 4.5 (b)), derived from the scanning electron microscopy image of the static nanostructure. Comparison of the theoretical prediction with the experimentally obtained data yields an estimate for the measured inelastic scattering background (green dashed lines in Figs. 4.5 (c-e)). For a more detailed data evaluation, Figs. 4.5 (c-e) depict three integrated regions of the measured diffraction data (black dots) in comparison with the theoretical results (green solid line). The different intensities of $(1\bar{1})$ and $(\bar{1}1)$ compared to (11) and $(\bar{1}\bar{1})$, observed consistently in experiment and theory, reflect the deviations of our static wavy nanostructure from a perfectly sinusoidal pattern [67].

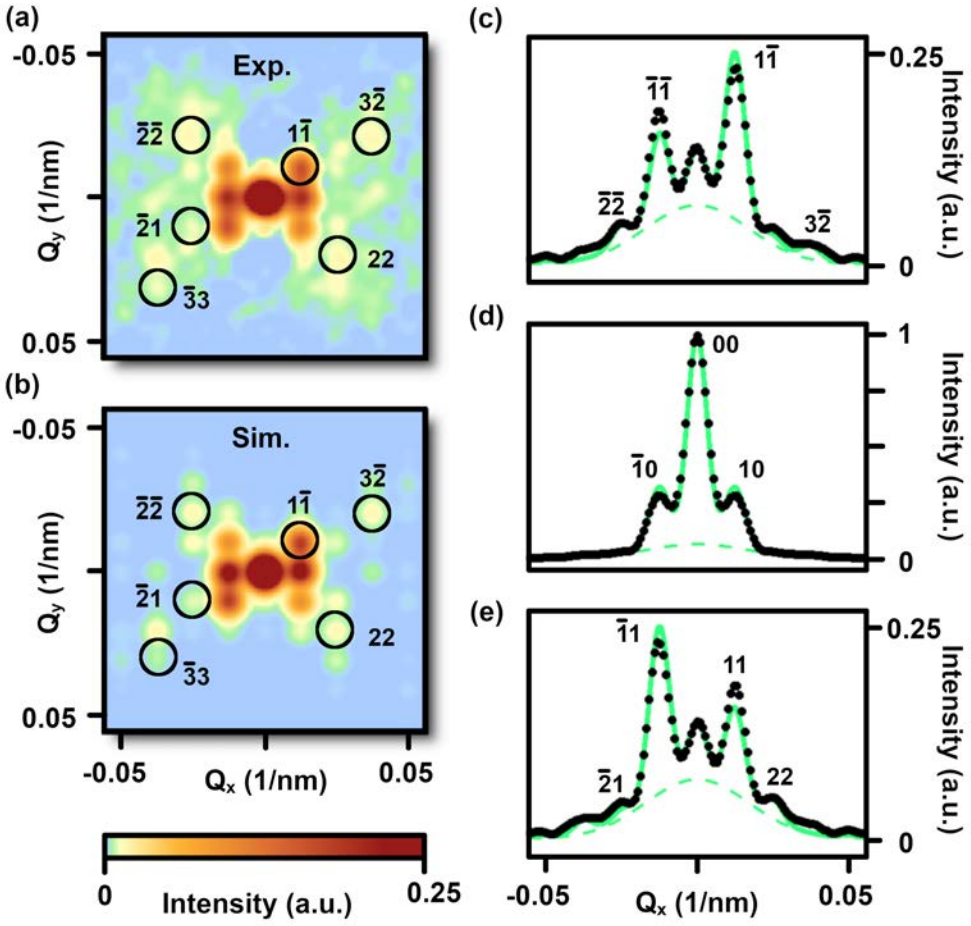


**Figure 4.5: Experimental ultrafast diffraction results in comparison to simulations. (a)** Measured static small-angle diffraction after subtraction of an inelastic scattering background. The appearance of $3^{rd}$ order spots in $x$ direction and $4^{th}$ order spots in $y$ direction indicate a sub-unit-cell resolution of ~25 nm in both dimensions. For display purposes, interpolation by a factor of three was performed via zero-padding. **(b)** Theoretical small-angle diffraction derived from the measured SEM image (see Fig. 4.2 (c)). **(c)** Integrated intensity (black dots) of the $-1^{st}$ and $-2^{nd}$ order in $y$ direction in comparison to theory (green solid line). Inelastic scattering background depicted as dashed line. **(d)** Integrated intensity (black dots) for the $0^{th}$ order in $y$ direction. **(e)** Integrated intensity (black dots) of the $+1^{st}$ and $+2^{nd}$ order in $y$ direction. (Figure reproduced from our publication [67])

In summary, THz-compressed sub-100-fs few-electron pulses at multi-keV electron energies can be generated with sufficiently high monochromaticity and transverse coherence to produce multi-beam interference and to yield undistorted small-angle diffraction patterns of nanoscale metal structures when adequately compensating for magnetic field oscillations. These encouraging results serve for quality assessment of the tiny static building blocks comprising our sample and additionally also as a valuable reference for the intended time-resolved measurements of optically-excited nanostructures.

# 5

# Terahertz-Induced Electron Nanodiffraction

*"The near field is the awkward customer in electromagnetism: it refuses to radiate away from objects and therefore cannot be captured by a conventional optical system. Locked away in the near field are the fine resolution details of the object; their absence from a conventional image limits resolution to the order of a wavelength."*

*– quote by John Pendry [140]*

In nature, there exists a huge diversity of materials which are capable of manipulating electromagnetic waves in all different kind of ways, be it for example through attenuation, deflection or dispersion. Solid lenses, prisms and mirrors have been utilized in microscopy applications and other optical devices for centuries to tailor freely propagating radiation with its rapidly-oscillating and strongly-interlinked electric and magnetic fields. Following Abbe's diffraction limit, the impinging wavelength determines the degree of detail encoded in the far-field response of conventional optics [140]. Sub-wavelength-scale features such as atomic details lose importance in this regime and the illuminated material mostly appears as a homogeneous rather than a structured medium. This justifies the applicability of common conceptual descriptions based on effective, homogeneous material properties [140], including refractive indices and absorption coefficients, for defining the underlying light-matter interactions.

The development of novel optical effects and devices with extraordinary capabilities, exceeding the ones of natural materials, often rely on enhanced control over electromagnetic radiation on a sub-wavelength scale in the underlying light-matter interactions [70,72,140]. Ideally, such ability is desired to precisely tailor at will the amplitude, phase and polarization of incident electric and magnetic contributions independently of each other, which are typically highly interlinked and strongly interdependent in the case of freely propagating waves [143]. When confined to sub-wavelength scales, however, the symmetry between electric and magnetic field components may be broken with one type of near field being more dominant than the other one as a result of selective field enhancement [144,145], which renders their relationship more complex than for freely propagating electromagnetic waves.

While electrons can be trapped and manipulated by harnessing Coulomb forces, spatial confinement of light waves is typically achieved via the interaction of photons with oscillations of electron densities induced inside of metallic structures [146,147]. In contrast to the typical loss of high spatial frequency information in the far field, the rapidly-decaying evanescent electromagnetic waves confined to the close vicinity of an irradiated material's surface carry superior information about the object's finest details [140]. Consequently, the near-field region of sub-wavelength-scale metal structures and its characteristic evanescent fields represent the predestined regime of executing an advanced level of control on electromagnetic waves.

## 5.1 Observing Nanophotonic Materials and Metamaterials at Work

Mesoscopic structures, as the bowtie-shaped resonator applied for THz-induced electron beam deflection in Chapter 3, and their electromagnetic near fields work in a regime where microscopic and macroscopic concepts overlap [148]. When further increasing the lateral confinement and squeezing the light down to nanoscale dimensions, the realm of nanophotonic materials and metamaterials [70, 72, 140, 149, 150] is entered, whose functionality relies on sophisticated structuring on intermediate length scales, i.e. between the incident optical wavelength and atomic scales. These smartly-engineered materials obtain their unprecedented electromagnetic properties from a precisely tailored sub-wavelength-scale architecture rather than the optical response of the constituent material [140, 147]. Thus, metamaterials and nanophotonic materials expand the conventional definition of materials with their atomic constituents to a novel category of artificial materials, characterized by a grid-like arrangement of sub-wavelength-scale building blocks and their specific nanoscale near fields.

Equipped with such arrays of tiny antennas serving for the localization of photon energy densities and offering advanced control of the vector nature of light on sub-wavelength dimensions, plasmonics and nanophotonics allow for the transformation of interacting electromagnetic wavefronts into almost arbitrary shapes [147]. Contemporary research, aiming for the development of flat and lightweight optics [70, 72] with exotic optical responses and functionalities, includes nanometric optical rulers [151], cloaking devices [71], negative refraction [139], flat lenses [72] and chiral sensors [152], for example.

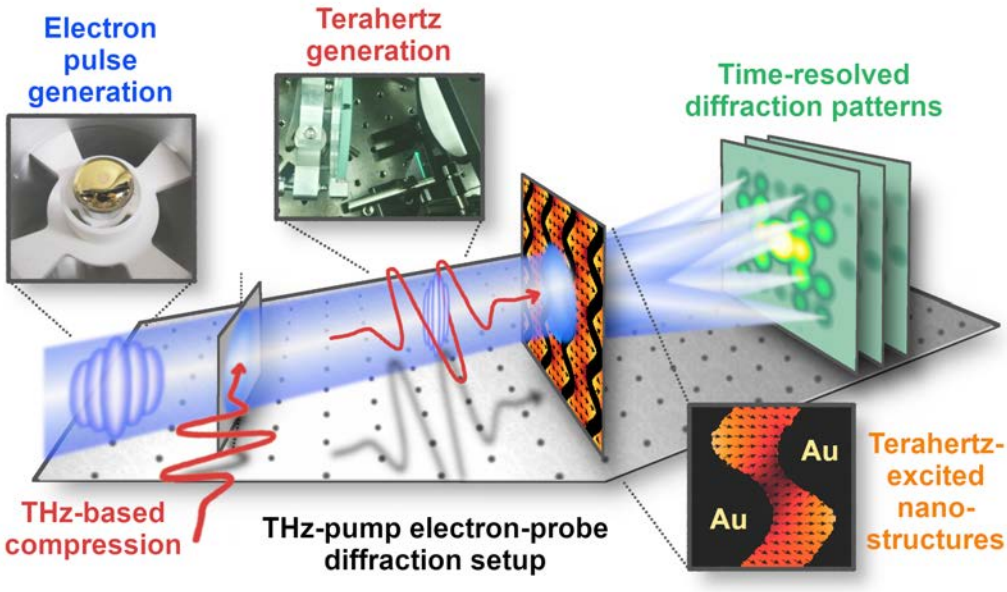


**Figure 5.1: Ultrafast electron diffraction of nanophotonic waveforms.** A 2D array of wavy metal nanostructures (black) on a dielectric substrate is illuminated with a single-cycle terahertz (THz) waveform (red), which induces rapidly-changing near fields (black arrows) in proximity of the material. Femtosecond single-electron probe pulses (blue), generated via laser-triggered two-photon photoemission at a gold-coated cathode and compressed in time by all-optical means, produce coherent multi-beam interference and therefore small-angle diffraction patterns (green), which capture time-frozen snapshots of the electromagnetic field distributions as a function of electron-THz delay time. For highest timing stability in the underlying THz-pump electron-probe scheme, a single laser source is harnessed to trigger electron emission as well as to generate single-cycle THz radiation via optical rectification.

Ever better engineering of the optical response and performance of nanophotonic devices, by refining the feature size of the underlying structures, crucially relies on the capability for detailed quality assessment of the individual building blocks as well as for precise examination of the induced near fields with highest spatio-temporal precision [140]. Since the incoming electromagnetic field takes

direct control of the electron densities inside the metal structures and thereby imprints its temporal evolution onto the induced charges and currents, an all-encompassing experimental analysis of the initiated dynamics in space and time even requires sub-excitation-cycle precision to complement the nanoscale spatial resolution. Near-field imaging methods to experimentally access these nanoscale fields are ever more important since theoretical modeling of all six structure-specific electromagnetic near-field components with nanoscale precision and in a time-resolved manner is far from trivial [145].

Sophisticated experimental tools are required for tackling this challenge since such sub-wavelength-scale features are typically concealed in the far-field radiation as evaluated in conventional imaging schemes [140]. Pioneering time-resolved nanoscopy studies with exceptional spatio-temporal precision include sub-picosecond terahertz-pulse-induced scanning tunneling microscopy [55], pump-probe terahertz spectroscopy at a sharp metal tip in a scanning near-field optical microscopy (SNOM) scheme [16] as well as successful demonstrations of video-rate stimulated emission depletion (STED) [56] and stochastic optical reconstruction microscopy (STORM) [57]. Super-resolution microscopy approaches, as STORM and STED, are capable of circumventing Abbe's resolution limit dictated by diffraction. However, they mostly rely on transparent samples that can be functionalized with fluorescent molecules [147], which is a completely different regime of application compared to electromagnetism in metal nanostructures. In contrast, SNOM employs a sharp needle which is raster scanned across the sample while converting some of the rapidly-decaying evanescent fields into far-field radiation [145,147]. For these promising nanoscopy approaches, signal detection remains a balancing act between sufficient interaction with the evanescent near fields for obtaining a detailed map of the nanoscale near-field distributions while restricting the probe-induced distortions to a minimum [145].

In this thesis, a more direct, complementary approach is proposed which dispenses with the need for a nanoscale probe. Ultrashort few-electron pulses (see Chapter 3) are suggested as suitable probes for non-invasively capturing time-frozen snapshots of nanoscale architectures including their rapidly-oscillating electromagnetic near fields (see Fig. 5.1). As demonstrated in Chapter 4, ultrafast electron diffraction equipped with THz-compressed few-electron pulses is capable of delivering distortion-free examination of nanoscale structural details in reciprocal space despite the tiny diffraction angles and the challenging demands regarding spatial coherence (see also Mohler et al. [67]). Besides, the well-defined interaction of the electron charge with structure-specific electromagnetic field distributions in nanophotonic materials holds promising potential as a probing method that is non-invasive, not entangled with the excitation and does not distort the fields and dynamics inside the structures [67].

Ultrafast electron microscopy and diffraction with laser-generated femtosecond electron pulses have been established as widespread approaches for investigating structural dynamics and atomic motions in molecules and condensed matter [46, 68, 69, 153]. The spatio-temporal resolution of ultrafast electrodynamic phenomena, however, has so far only been realized by incoherent point-particle scattering [54,108] and not by any electron-interferometric technique, which would fully capitalize the highly coherent electron beams of modern imaging devices. All electron-interferometric investigations with electron holography [64,65], differential phase contrast [64,65] and atomic picodiffraction [66,110] have so far been restricted to much slower time scales than the ultrahigh frequencies in the THz and PHz regimes, required to uncover the operation of complex photonic materials and metamaterials [70,72,140,149,150] on sub-wavelength and sub-cycle dimensions [16,54,154,155]. This chapter of my thesis reports the direct susceptibility of electron matter waves to the dynamic electromagnetic fields and potentials induced in nanophotonic materials, which advances electron diffraction, holography and related electron interferometric imaging methods from their established stationary settings to the domain of electrodynamics on the time scales of the cycles of light [67].

## 5.2 Basic Concept and First Experimental Results

Equipped with the quality assessment and reference measurement of the static nanostructures provided in the previous chapter, ultrafast small-angle diffraction with THz-compressed few-electron pulses is now applied to examine dynamic electromagnetic near fields and potentials arising from the exposure of our wavy nanostructured sample to single-cycle THz pulses. The basis of our measurement concept is the conjecture that the electron charge will interact with the structure-dependent optical near fields and potentials in proximity of the nanophotonic material. Thereby, the transient states of the optical excitation are expected to get encoded in the time-resolved electron diffraction patterns under the assumption of probing electron bunches with sub-excitation-cycle durations (detailed theoretical framework presented in Chapter 6). Despite the long-wavelength nature of the excitation, substantial non-resonant and structure-specific field enhancement is expected to arise for THz-illuminated arrays of metal nanostructures [146], breaking the symmetry between electric and magnetic contributions in a structure-specific way. Therefore, the interaction of electrons with the far-field terahertz radiation and the locally-induced sub-unit-cell dynamics may potentially give rise to characteristic dynamic changes affecting the locations and intensities of the recorded 2D electron diffraction patterns [67].

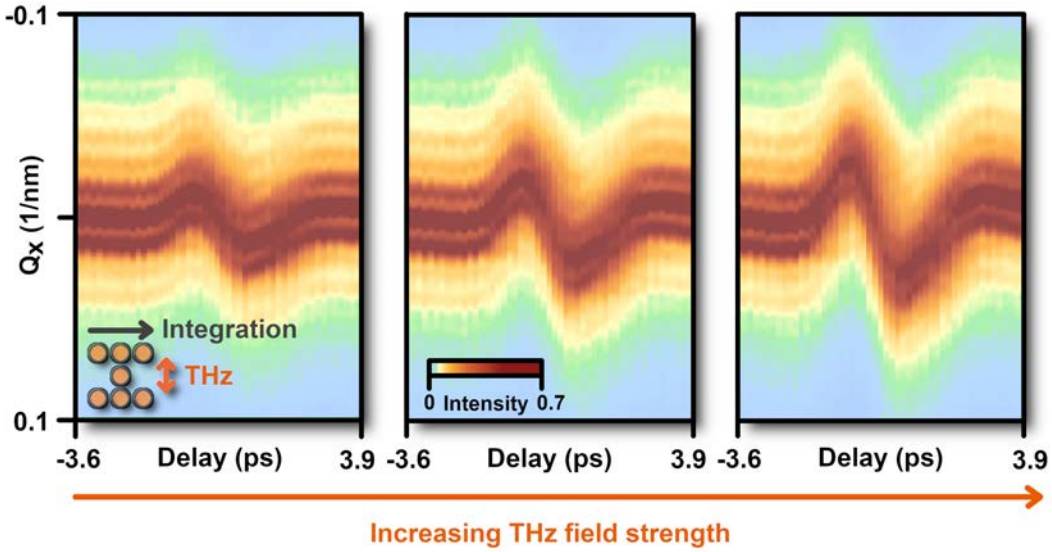


**Figure 5.2: Terahertz-induced electron nanodiffraction.** Visualization of three-dimensional time-dependent diffraction data in the time-Qx domain obtained from the terahertz-excited nanostructured material for three different terahertz (THz) field strengths. The integration of the entire 2D diffraction data (black arrow) for each time delay (major Bragg spots as illustrated in the inset), resulting in the depicted line scans, is performed perpendicular to the polarization of the excitation field (orange arrow) in order to display all major optically-induced dynamics. The observed delay-dependent global deflection clearly scales with the incident THz field strength, which underlines the electromagnetic origin of the observed dynamics. For display purposes, interpolation of the diffraction data is performed via zero-padding.

Preliminary proof-of-principle pump-probe diffraction experiments were performed by following the same measurement procedure as for the acquisition of the bowtie-based streaking curves in Chapter 3. When turning on the single-cycle electromagnetic excitation, we see several substantial and distinct modifications to the measured diffraction pattern as a function of the terahertz-electron time delay (see Fig. 5.2). Bragg spots up to the fourth order could be captured in the depicted delay-resolved line scans revealing that the most dominant dynamic feature is a time-dependent deflection of the whole diffraction pattern along $x$ [67], the polarization direction of the terahertz field. A quick assessment of the depicted data already delivers a wealth of information about the dynamics under investigation: (1) The observed global deflection reflects the single-cycle characteristics of the incoming THz radiation.

(2) The captured dynamics are highly reversible, as required for successful application of a pump-probe detection scheme, with the system quickly relaxing back to its original state after the excitation. (3) The Bragg spot spacing appears to remain unaffected by the light-matter interaction, reflecting the fact that the nanoscale architecture itself is not altered by the excitation field. (4) The amplitude of the deflection scales with the incident THz field strength, indicating that the observed phenomena are indeed of purely electromagnetic origin. (5) With increasing THz-induced deflections substantially exceeding the Bragg spot spacing, blurring effects start to arise at the delays of highest streaking slope, which are attributed to the finite duration of our electron probe pulses (compare Chapter 3).

Overall, the time-resolved diffraction patterns show a clear responsiveness to the THz-induced dynamics. Despite these encouraging preliminary results, the electron pulse duration turned out to be yet not short enough to allow for any sophisticated data analysis of Bragg spot intensities. This observation necessitated an upgrade (see Chapter 3) of the original UED setup. The old setup [31], solely applied in this thesis for these particular measurements (in Fig. 5.2) and based on a less compact electron gun design at 70 kV [156], utilized a ytterbium:yttrium aluminum garnet (Yb:YAG)–based regenerative amplifier with near-1-ps pulse duration [157] for laser-triggered electron pulse and THz generation.

## 5.3 Final Experimental Configuration

In the course of this thesis and in close collaboration with Dominik Ehberger, a more compact electron gun was put into operation [59], a new laser source with 270-fs pulse duration was incorporated into the UED setup and enhanced timing stability was achieved by a consolidated design of the optical systems applied for electron and THz generation (for details refer to Chapter 3 and Mohler et al. [67]).

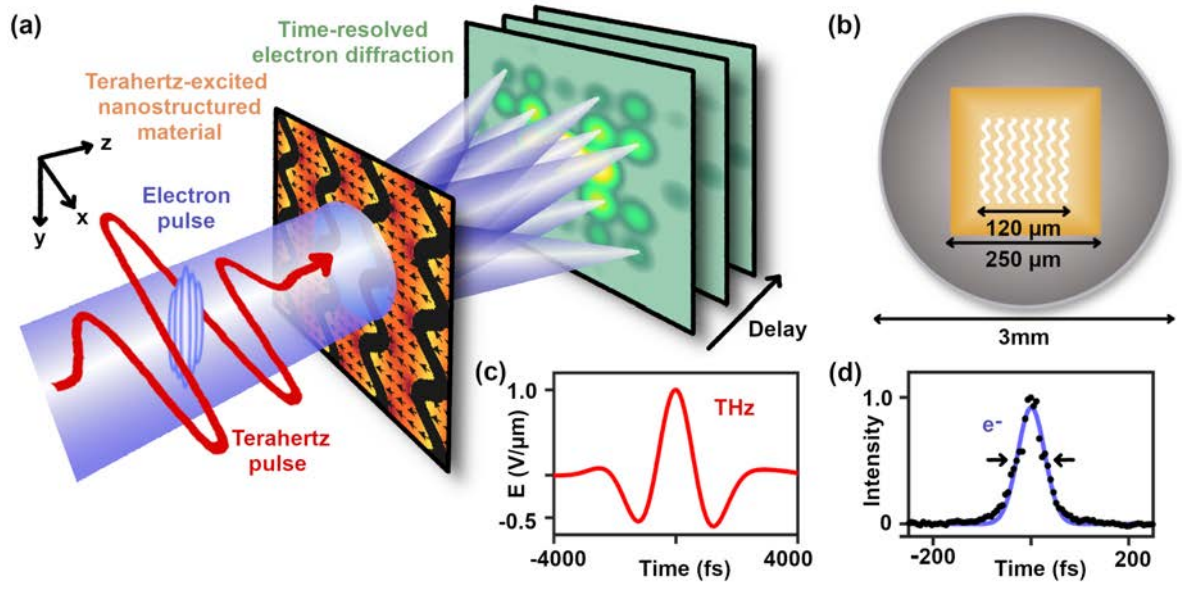


**Figure 5.3: Time-resolved small-angle electron diffraction of a two-dimensional THz-excited nanostructured array.** **(a)** Underlying concept and experimental setup. A THz pulse (red) excites photonic nanostructures (black) and induces local electrodynamic fields (amplitude in orange; direction as black arrows). Ultrashort electron pulses (blue) are diffracted of the nanostructures and probe the local electromagnetic potentials as a function of delay time. Delay-resolved diffraction patterns (green) reveal the THz-induced dynamics. **(b)** Design of our wavy nanostructured array including its support structures (more details in Chapter 4). **(c)** Electric field of the excitation pulse with a central frequency of 0.35 THz, as recovered from the mesoscopic resonances described in Chapter 3. **(d)** Temporal profile of the electron pulses (dots) measured via THz-induced streaking with a bowtie-shaped resonator (Gaussian fit as solid line). The full width at half maximum is ~60 fs (black arrows). (Figure design based on our publication [67])

### 5.3.1 Terahertz Pump Pulses for Optical Excitation

An all-embracing characterization of the applied optical-pump electron-probe diffraction setup requires information about the waveform of the terahertz pump pulses, which are produced via optical rectification and laser-generated Cherenkov radiation in a slab-like lithium niobate ($LiNbO_3$) crystal [30] with intrinsic time synchronization with respect to the laser-triggered electron emission at the cathode (details in Chapter 3). An evaluation of the mesoscopic resonances, visualized via global deflections of sub-100-fs electron pulses in Fig. 3.6, unveils a close-to-single-cycle, cosine-like incident waveform of the terahertz pump pulses (see Fig. 5.3 (c)), which is in accordance with the terahertz waveform retrieved from electro-optic sampling for a comparable experimental setting [30].

### 5.3.2 Electron Probe Pulses for the Acquisition of Time-Frozen Snapshots

Ultrafast electron diffraction at highest temporal resolution further requires schemes for efficient electron pulse compression and high electron energies to minimize dispersion effects, although lower electron energies would facilitate small-angle diffraction [51]. To avoid space-charge effects, only 4 ± 2 electrons per pulse are generated from an optical focal spot of ~5 µm in diameter at the source, of which less than one electron per pulse arrives at the sample [67]. These electron pulses are accelerated to energies of 75 keV and compressed in time with the help of terahertz radiation [30] at a planar metal membrane [32]. As a prerequisite for coherent interference and the appearance of a 2D diffraction pattern to occur, the transverse coherence length is increased to ~100 nm (full width at half maximum) at the expense of a reduction in electron flux by enlargement of the beam diameter to ~2 mm [141]. Streaking measurements via a THz-excited, bowtie-shaped aperture [31] reveal a pulse duration of ~25 fs (root mean square) or ~60 fs (full width at half maximum) at the sample's position (Fig. 5.3 (d)).

### 5.3.3 Experimental Implementation of Collinear Pump-Probe Diffractive Imaging

As magnetic solenoids (see Fig. 5.4 (a)) focus the beam in space, the electron pulses also have to be compressed in time to generate the shortest pulses at the position of the sample (details in Chapter 3). Terahertz-induced and velocity-matched electron pulse compression is implemented via intersecting the terahertz pulses and the electron beam at an angle of approximately 90° on a planar compression element (see Fig. 5.4 (b)). For the realization of a collinear pump-probe diffractive imaging configuration, the terahertz radiation is focused onto the sample by a parabolic mirror, which is equipped with a small hole in order to allow for undisturbed transit of the time-compressed sub-100-fs electron pulses and subsequent collinear electron-THz interaction at the nanostructured array (see Fig. 5.4 (c)).

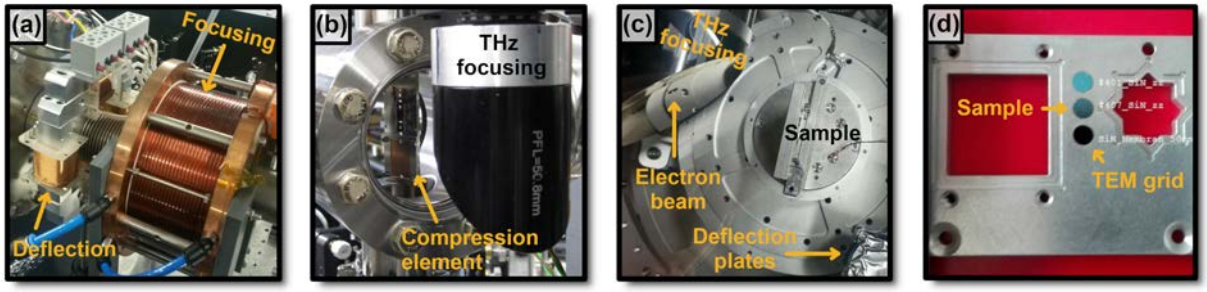


**Figure 5.4: Experimental implementation.** **(a)** Electron optics **(b)** Compression element and THz focusing **(c)** Sample chamber (deflection plates moved out of the electron beam) **(d)** Sample holder

## 5.4 Bragg Spot Dynamics of Optically-Excited Nanostructures

Figure 5.5 displays the 3D delay-resolved diffraction data in the time-$Qx$ domain obtained from our THz-excited nanostructures with THz-compressed sub-100-fs electron pulses (see Mohler et al. [67]). The enhanced temporal resolution finally allows for a detailed analysis of Bragg spot intensities and positions. For this purpose, the top, middle and bottom panels of Fig. 5.5 (a) depict the temporal evolution of three $y$-integrated regions. The data extracted from the three individual regions is plotted with a displacement, whereby the orange dots in the corresponding insets indicate the major Bragg spots plotted as a function of time. The time-resolved results reveal a wealth of sub-excitation-cycle dynamics and represent, to our knowledge, the first demonstration of a pump-probe diffraction experiment with THz-compressed electron pulses at the superior time resolution that they provide [67].

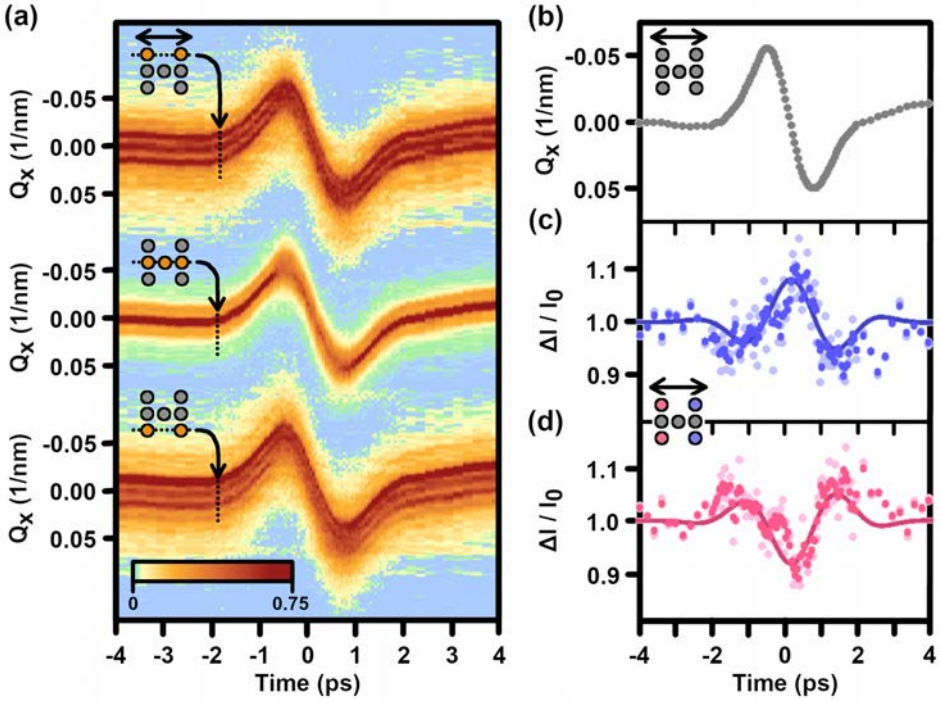


**Figure 5.5: Sub-excitation-cycle Bragg spot dynamics.** Visualization of the three-dimensional time-dependent diffraction data in the time-$Qx$ domain obtained from the terahertz-excited nanostructured sample. **(a)** The top, middle and bottom panels show the temporal evolution of three $y$-integrated regions whereby the orange dots in the insets indicate the major Bragg spots that are plotted as a function of time (see static line scans in Figs. 4.5 (c-e)). The black arrow in the uppermost inset indicates the polarization of the THz excitation. **(b)** Global deflection of the entire diffraction pattern as a function of time delay. **(c)** Relative Bragg spot intensity (bright dots, raw data; blue dots, smoothed) of $1\bar{1}$ and $11$ in comparison to simulations (solid line) as a function of time. **(d)** Relative Bragg spot intensity of $\bar{1}\bar{1}$ and $\bar{1}1$ (bright dots, raw data; red dots, smoothed) in comparison to the simulations (solid line). These Bragg spots project similarly along the excitation's polarization (inset, black arrow). (Figure design based on our publication [67])

### 5.4.1 Global Deflection of the Entire Diffraction Pattern

The most striking feature is a synchronous deflection of the entire pattern (see Fig. 5.5) exhibiting the following characteristics: (1) The temporal shape of the deflection is almost symmetric in time with an initial rise at $-1.8$ ps towards higher angular deflections as fast as the final decay towards zero deflection at 1.8 ps. (2) The Bragg spots remain discernible throughout the entire THz-electron delay range, although the maximum time-dependent global deflection exceeds the inverse lattice constant by four times. (3) The Bragg spot spacing stays constant at only minor changes of contrast and width.

### 5.4.2 Sub-Excitation-Cycle Dynamics of Bragg Spot Intensities

In addition to the global deflection affecting the entire pattern, we observe substantial changes of Bragg spot intensities as a function of electron-THz delay (see also Mohler et al. [67]). To study the induced sub-excitation-cycle dynamics, first-order Bragg spot intensities are averaged in a pair-wise way since our THz field cycles interact rather weakly with the nanostructures and the limited signal-to-noise ratio of our proof-of-concept experiment impedes conclusive analysis of single Bragg spots for now. In Figures 5.5 (c,d), the integrated relative intensities of $(1\bar{1})$ and (11) are compared with the average of $(\bar{1}\bar{1})$ and $(\bar{1}1)$, because these pairs share a common first Miller index and project similarly to the excitation's polarization along the x axis. For this purpose, the Bragg spot intensities are fitted with a polynomial peak-detection algorithm as products of amplitude and width, whereby width changes are determined from the correlated amplitude changes of all four evaluated spots. In Figures 5.5 (c,d), the smoothed results comprising of the dark blue and red dots are obtained by a 3-point moving average of the raw data (faint blue/red dots) while the solid lines depict theoretical predictions [67].

The insights delivered by the time-resolved analysis of the Bragg spot intensities include the following: (1) In analogy to the global deflection, the oscillations in Bragg spot intensities represent a highly reversible process. (2) The single-cycle characteristics of the incoming terahertz radiation is clearly imprinted onto the observed Bragg spot dynamics, indicating their purely electromagnetic origin. (3) The signal-to-noise ratio provided by our few-electron pulses is high enough for capturing the maximum relative intensity changes of ±8% observed for the pair-wise averaged first-order Bragg spots. (4) The opposing temporal shapes in Figs. 5.5 (c,d) have maxima and minima occurring at the turning points of the global deflection (see Figs. 5.5 (b)), which can be attributed to the phase shift of ~90° between incident waveform (see Fig. 5.3 (c)) and global Bragg pattern motion (see Fig. 3.6 (c)).

The captured time-resolved Bragg spot dynamics, including the centrosymmetry-violating Bragg spot intensities and their evolution in synchrony to the shape of the THz excitation field, establish THz-compressed few-electron pulses as valuable probes for investigating light-matter interactions in nanophotonic materials and metamaterials with sub-excitation-cycle resolution [67]. By further optimizing this proof-of-principle experimental setup in terms of signal-to-noise ratio, a thorough assessment of individual Bragg spot intensities should become feasible and deliver more detailed information about the structure-specific transient field distributions induced within the sample. This approach is widely applicable, independently of the explicit nanoscale architecture of the sample. The appearance of Bragg spot dynamics at optical frequencies simply arises from a structure-specific break in symmetry by our 2D nanostructured array, which favors electric over magnetic field enhancement (more details in Chapter 6). Sophisticated nanoscale architectures, precisely tailored for exhibiting exceptional optical responses, are expected to yield an even richer 2D set of Bragg spot intensities and more characteristic optically-induced Bragg spot dynamics than our simple wavy prototype sample.

Our experiment touches an extreme limit of quantum-coherent light-electron interaction, for which the electrons mostly seem like point particles with respect to the optical waveform (see Chapter 3). Nevertheless, substantial quantum effects are required for explaining the THz-electron interaction in our diffractive imaging experiment since the mere existence of Bragg spots requires interference of coherent electron de Broglie waves and detailed knowledge about the amplitude and phase of the electron wave function. The observed Bragg spot dynamics indicate that the quantum nature of free electrons is present irrespectively of the wave packet dimensions if a proper setting for analysis is applied. The underlying principles are further scrutinized in Chapter 6 by elucidating quantum-mechanical phase shifts of the electron wave function inflicted by electromagnetic potentials.

# 6

# Theoretical Interpretation of THz-Excited Bragg Spot Dynamics

*"On Mondays, Wednesdays and Fridays we use the wave theory; on Tuesdays, Thursdays and Saturdays we think in streams of flying energy quanta or corpuscles."*

*– quote by William Henry Bragg*

Electron diffraction experiments of terahertz-excited nanostructured materials touch an extreme limit of quantum-coherent light-electron interaction, for which quantum effects beyond a classical point-particle approximation of electrons may emerge (see Mohler et al. [67]). One of the key quantum mechanical concepts involved in such experiments is given by the principle of wave–particle duality, which expresses the inability of the rigorous classical differentiation between particles on the one hand and waves on the other hand to describe the behavior of quantum-scale objects to their full extent [158, 159]. As stated by the quote above, the particular quantum mechanical picture of choice depends on the explicit scientific question under interrogation. For some phenomena, the particle picture might deliver a more insightful description while for others the wave properties of quantum-scale objects might manifest themselves more dominantly and therefore provide a more intuitive interpretation of the observed dynamics. Multi-beam interference, as observed for single-electron pulses impinging on metallic nanostructures (see Chapter 4), clearly reflects the dual wave-particle nature of electrons as well as the probabilistic signatures of quantum mechanical phenomena [158, 159].

An important prerequisite for a structure to coherently diffract electron de Broglie waves and for an interference pattern to appear is given by a designated modification of the electron wave function on the nanoscale but without collapsing it [158, 159], so that the actual measurement remains restricted to the recording of the diffraction pattern. For single-electron pulses, the final diffraction pattern in the particle picture sequentially builds up from many individual scattering events. By integrating over many single-electron events, their statistical distribution gradually reproduces the pattern obtained from a single-shot measurement with a densely-packed electron pulse. The experimentally-demonstrated persistence of the interference pattern in Chapter 4, observable even for an ultimately reduced electron density approaching the regime of single-electron pulses, indicates that the electron wave function actually spreads coherently over multiple unit cells in the object plane and is capable of interfering with itself. The correct prediction of the resulting far-field interference pattern relies on detailed knowledge about the spatio-temporal amplitude and phase of the electron wave function.

Apart from the groundbreaking insight that light and matter exhibit inherent characteristics of both particles and waves, quantum mechanics differs from classical mechanics in Heisenberg's uncertainty relation [158, 159], which establishes the impossibility of simultaneously determining the position of a quantum particle and its conjugate momentum with arbitrarily high precision. Heisenberg's uncertainty principle has profound implications for electron interferometry applications, such as

presented in this thesis. For electron diffraction experiments with a single slit of appropriate dimensions, for example, the width of the slit confines the transverse position of the electrons in the object plane. In accordance with the uncertainty principle, this spatial confinement induces a spread in transverse momentum. The propagation of the electrons to the phosphor screen subsequently maps this momentum spread into a spatial distribution of positions in the far-field, whose width (i.e. the distance between the first diffraction minima), increases when narrowing the slit. In case of a grating structure, as a one-dimensional approximation of our wavy nanostructured array, an analogous dependence on the width of the gaps exists for the envelope of the diffraction pattern.

In addition to the uncertainty relation, the quantization of physical properties and the wave-particle duality of light and matter, the most significant cornerstones of quantum mechanics encompass the Schrödinger equation [158], governing the behavior of wave functions, as well as the Aharonov-Bohm effect [160], underpinning the importance of electromagnetic potentials for electron interferometry. According to Aharonov and Bohm [160], two parts of a coherent electron wave packet traveling along two distinct trajectories will acquire a quantum-mechanical phase shift, which is directly related to the electromagnetic potentials along these trajectories. Pointing out the significance of electromagnetic potentials for incorporating the contributions from local and non-local electromagnetic fields alike into the analysis while maintaining the principle of locality, Aharonov and Bohm [160] predicted in their most prominent textbook example the imprint of relative phase shifts on electrons traveling along trajectories that enclose the static magnetic field of a long solenoid, even without local exposure to the field itself. This principle of potential-induced electron phase shifts also has profound implications in electron microscopy, where it is ubiquitous for the description of coherent electron scattering from various types of macroscopic and atomistic electromagnetic fields [64–66, 110]. For example, electric polarization and magnetic flux in nanostructures [64, 65] or the electric fields in the chemical bonds between the atoms in a crystal [66, 110] have been elucidated in this way.

In our time-resolved small-angle diffraction experiment (see Chapter 5), the incident terahertz radiation triggers a wealth of delay-dependent phenomena that are caused by purely electromagnetic effects and not by structural changes of the material (see Mohler et al. [67]). The origin of the observed deflections, globally affecting the entire diffraction pattern, can be attributed to mesoscopic resonances (see Chapter 3). On such microscale dimensions, the coherence properties of the electron beam remain untouched and non-trivial quantum contributions beyond a classical description via Lorentz forces, point particles and classical trajectories are not expected. Consequently, a classical approximation can correctly predict the results presented for THz-induced electron pulse compression and characterization (see Chapter 3). Any nanostructure-specific, THz-induced sub-unit-cell dynamics, however, represent a completely different regime once the coherence length of the electron beam is increased to exceed the size of the optically-excited elements and coherent interference is observed. Even in our extreme limit of quantum-coherent light-electron interaction with femtosecond electron pulses and long-wavelength sample excitation, the time-dependent signatures imprinted on the electron wave function and in particular on its quantum phase, as predicted by Aharonov and Bohm [160], may emerge in form of dynamic modifications to the observed interference, which represents the content of this chapter.

Owing to the interferometric nature of our nanodiffraction experiment, only a quantum mechanical description can deliver an all-encompassing picture of the entire dynamics. For the sake of clarity, however, the complexity of the presented theoretical framework is intentionally reduced by invoking a point-particle approximation and classical electron trajectories wherever applicable while delocalized electrons with spatially-tailored and temporally-modulated quantum phases are considered for accurately describing the experimentally-observed Bragg spot dynamics (see also Mohler et al. [67]). To

model the effect of the optically-excited nanostructures on the electron wave function, a phase-object approximation is applied. Spatially-varying transmission amplitudes [51] are derived from the measured static structures as described in Chapter 4, while the dynamics inflicted by the electromagnetic excitation are incorporated into the theoretical framework by position-dependent and delay-dependent phase shifts of the electron wave function following the concept of Aharonov and Bohm [160].

## 6.1 Electromagnetic Potentials and Aharonov-Bohm Phases

To investigate the origin of the dynamic changes inflicted to the diffraction pattern (see Chapter 5), we analyze the quantum mechanical phase shifts that an electron experiences as a result of THz-induced electrodynamics. In quantum mechanics, electromagnetic interactions are described via the Hamiltonian and potentials rather than the corresponding fields [161], whereby in the classical limit the effects obtained via the Lorentz force are reproduced. Along a given closed loop in space-time, the electron wave function obtains a quantum-mechanical phase shift according to the line integral [160]:

$$\Phi_{\mathrm{AB}} = \frac{e}{\hbar} \oint A_\mu dx^\mu \tag{6.1}$$

where $e$ is the elementary charge, $\hbar$ is the reduced Planck constant, $x^\mu = (ct, x, y, z)$ is the position four-vector under the Minkowski metric sign convention $(+,-,-,-)$ and $A_\mu = (\varphi/c, -A_x, -A_y, -A_z)$ is the electromagnetic potential four-vector composed of the electric scalar potential $\varphi$ and three components of the magnetic vector potential $A_x$, $A_y$ and $A_z$.

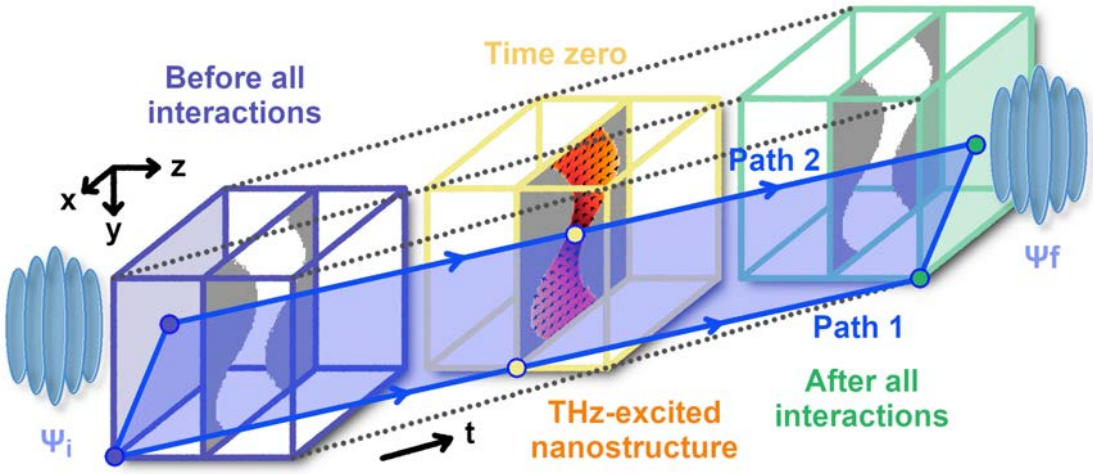


**Figure 6.1: Theoretical framework for THz-induced electron nanodiffraction based on 4D space-time integration of the electromagnetic potentials in proximity to a nanostructured material.** Space-time diagram for simulating the expected time-dependent phase maps imprinted on an incoming plane electron wave function $\psi_i$ (light blue) as a result of its interaction with the induced nanoscale electromagnetic potentials and fields (orange). The respective phase shifts are determined, as a function of the lateral positions $x$ and $y$ as well as the time delay $\Delta t$, via line integrals along closed loops in space-time (blue). (Figure design inspired by our publication [67])

Figure 6.1 illustrates the required space-time integration of Eq. (6.1) in an interaction volume that evolves rapidly in time (see also Mohler et al. [67]). For the nearly collimated beam of our experiment, electrons travel at constant velocity along approximately straight trajectories parallel to the $z$ direction. Thus, we assume an incoming electron wave function $\Psi_{\mathrm{i}}(x, y, \Delta t)$ with an initially flat phase front $\Phi_{\mathrm{AB}}(x, y, \Delta t) = 0$ (light blue). Provided that there is a temporal overlap at the sample between the

optical excitation and the electron pulse, the latter probes the induced electromagnetic fields and potentials in proximity of the nanostructures. After passage through the relevant interaction volume (center), the exit electron wave function obtains a spatially-modulated phase map $\Delta\Phi_{\mathrm{AB}}(x, y, \Delta t)$, depending on its arrival time $\Delta t$ with respect to the excitation field. For each delay time and lateral position, $\Delta\Phi_{\mathrm{AB}}(x, y, \Delta t)$ is calculated by evaluating the closed space-time integral around the area spanned by a path 2 along the $z$ direction at $x$ and $y$ and a selected reference path 1. The contributions associated with the two minor parts, connecting the parallel trajectories along the $z$ direction, vanish because there are no fields and potentials long before and long after the arrival of the excitation pulse.

## 6.2 Electron-THz Interaction at a Beam-Splitting Interface

For application of this framework to our experiment, we decompose the optical response of our wavy nanostructures into far-field contributions with macroscopic dimensions and the nanophotonic near-field components that occur within the unit cells. Under long-wavelength terahertz excitation, the macroscopic far-field response of our wavy nanostructures mimics in first-order approximation a wire grid polarizer (see [162] and Figure 6.2 (a)). In the applied long-wavelength regime, the fine details of the nanoscale substructures represent sub-wavelength-scale features and are therefore not directly encoded in the generated far-field radiation, neither in reflection nor in transmission. Owing to this loss of high spatial frequency information in the freely propagating terahertz waves [140], the macroscopic quantum-mechanical effects on the electron wave function can be calculated by modeling the wavy nanostructured array as an ultrathin, homogeneous beam splitter of unknown reflectivity. In this conceptual description of a medium's optical far-field response, the explicit shape and arrangement of the nanoscale building blocks remain concealed while their collective effects are accounted for by effective complex reflection and transmission coefficients $r_0 e^{i\varphi_\mathrm{r}}$ and $t_0 e^{i\varphi_\mathrm{t}}$, respectively.

The incident THz pulses are composed by a superposition of plane waves with polarization in the $x$-$z$-plane. For the sake of simplicity, the analytical calculation provided below is illustrated for a single frequency but its generalization to THz pulses is straightforward on the basis of the principle of superposition. Benefiting from the gauge invariance of physical observables in quantum mechanics, the electromagnetic fields of plane waves in free space can be reduced to a function of the vector potential, whereas the contribution of the scalar potential can be set to zero in Coulomb gauge [67]:

$$\vec{E} = -\frac{\partial \vec{A}}{\partial t} \qquad \text{and} \qquad \vec{B} = \nabla \times \vec{A} \tag{6.2}$$

Consequently, the space-time integral of Eq. (6.1) in the applied plane wave approximation reduces to a line integral merely involving the incident, reflected and transmitted magnetic vector potentials:

$$\Phi_{\mathrm{AB}} = -\frac{e}{\hbar} \oint \vec{A} \cdot d\vec{s} \tag{6.3}$$

The exclusive dependence of such electron phase shifts on the magnetic vector potential of the optical excitation is in analogy to attosecond streaking experiments [163], where the generated photoelectrons are subject to a net momentum transfer determined by the time of birth of the electrons in relation to the vector potential of the interacting NIR laser pulse. In contrast to attosecond streaking, for which the electric field of the laser pulse is applied along the direction of electron motion resulting in a longitudinal momentum transfer, the following analysis of the optically-induced phase shifts at a

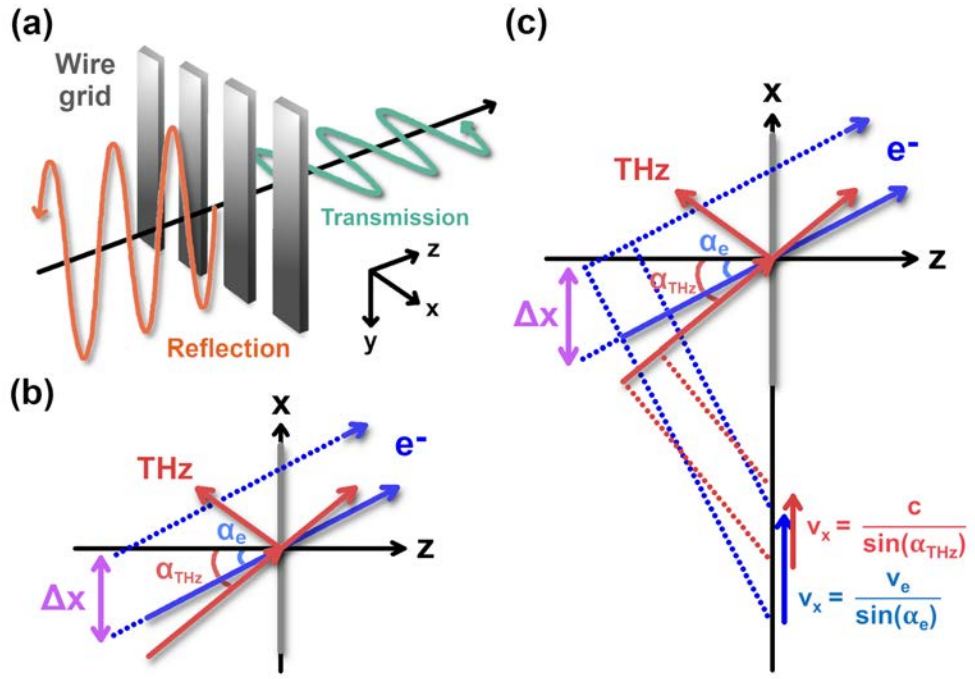


**Figure 6.2: Electron-terahertz interaction at a planar beam splitter of arbitrary splitting ratio.** **(a)** Nanoscale grating acting as a wire grid polarizer. **(b)** At this beam-splitting interface (gray), incident plane waves (orange), composing our THz pulses with linear polarization in the $x$-$z$-plane and impinging on the interface at an angle $\alpha_{\mathrm{THz}}$, interact with a collimated electron beam. The electrons travel along parallel trajectories (blue) with an angle of incidence $\alpha_{\mathrm{e}}$, whereby the lateral spacing between the two depicted electron paths, employed in the following for illustrating the required space-time integration, is abbreviated by $\Delta x$. **(c)** Independently of the splitting ratio of the material under investigation, the THz-induced deflection of the electron beam can be suppressed for matched velocities of the electron and THz radiation along the interface.

symmetry-breaking interface aims at predicting deflections rather than accelerations or decelerations of the electron beam. For general applicability, we define the incident, reflected and transmitted electromagnetic waves for arbitrary angles of incidence and beam-splitting properties of the nanostructures. The incident plane wave, impinging on the interface at an angle $\alpha_{\mathrm{THz}}$ (see Fig. 6.2 (b)), and its related reflected wave are represented in the region $z \leq 0$ by these magnetic vector potentials:

$$\begin{pmatrix} A_z^{\mathrm{in}} \\ A_x^{\mathrm{in}} \end{pmatrix} = \begin{pmatrix} -sin(\alpha_{\mathrm{THz}}) \\ \cos(\alpha_{\mathrm{THz}}) \end{pmatrix} \frac{E_0}{\omega} cos(\omega t - ksin(\alpha_{\mathrm{THz}})x - kcos(\alpha_{\mathrm{THz}})z) \tag{6.4}$$

$$\begin{pmatrix} A_z^{\mathrm{ref}} \\ A_x^{\mathrm{ref}} \end{pmatrix} = -r_0 \begin{pmatrix} sin(\alpha_{\mathrm{THz}}) \\ \cos(\alpha_{\mathrm{THz}}) \end{pmatrix} \frac{E_0}{\omega} cos(\omega t - ksin(\alpha_{\mathrm{THz}})x + kcos(\alpha_{\mathrm{THz}})z + \varphi_{\mathrm{r}}) \tag{6.5}$$

Here, $t$ is time, $\omega$ is the angular frequency, $E_0$ is the electric field amplitude and $k$ is the wave number. Under the chosen sign convention [164], as commonly applied in thin film optics, the reflected light at a perfect mirror interface is correctly expressed by $r_0 = 1$ and $\varphi_{\mathrm{r}} = 0$ since the optical phase shift of $\pi$ is already encoded in the assumed directions (i.e. amplitudes) of the electric field vectors. The complementing transmitted wave in the region $z > 0$ is expressed by:

$$\begin{pmatrix} A_z^{\mathrm{trans}} \\ A_x^{\mathrm{trans}} \end{pmatrix} = t_0 \begin{pmatrix} -sin(\alpha_{\mathrm{THz}}) \\ \cos(\alpha_{\mathrm{THz}}) \end{pmatrix} \frac{E_0}{\omega} cos(\omega t - ksin(\alpha_{\mathrm{THz}})x - kcos(\alpha_{\mathrm{THz}})z + \varphi_{\mathrm{t}}) \tag{6.6}$$

The phase shift imprinted on the electron wave function is now evaluated via Eq. (6.3) for all three contributions separately. Parallel electron trajectories are traced through the oscillating electromagnetic cycles assuming an incident angle $\alpha_e$ and constant electron velocity $v_e$:

$$\begin{pmatrix} z \\ x \end{pmatrix} = \begin{pmatrix} cos(\alpha_e) \\ \sin(\alpha_e) \end{pmatrix} v_e(t - \Delta t) + \begin{pmatrix} -sin(\alpha_e) \\ cos(\alpha_e) \end{pmatrix} cos(\alpha_e)\Delta x \tag{6.7}$$

Our reference trajectory, intersecting the beam-splitting interface at $x = 0$, defines the electron arrival time $\Delta t$ at the nanostructures, whereas the corresponding arrival times $\Delta t + \tau$ for the remaining parallel trajectories depend on the respective spatial distances $\Delta x$ from this reference path as follows:

$$v_e \cdot \tau = sin(\alpha_e) \cdot \Delta x \tag{6.8}$$

We let the resulting line integrals converge by assuming a slowly-decreasing terahertz field strength at $\pm\infty$, which is a valid assumption for our experimental setting with picosecond THz pulses. With the reduced Planck constant $\hbar$, the elementary charge $e$, $\beta = v_e/c$ and an electron beam diameter much smaller than the terahertz wavelength, the THz-induced phase shifts of the electron wave function resulting from the incident, reflected and transmitted waves can be approximated as follows [67]:

$$\Delta\Phi_{AB}^{in} = \frac{eE_0}{\hbar\omega}\left[\frac{sin(\alpha_{THz} - \alpha_e)}{1 - \beta cos(\alpha_{THz} - \alpha_e)}\right] cos(\omega\Delta t)(sin(\alpha_e) - \beta sin(\alpha_{THz}))\Delta x \tag{6.9}$$

$$\Delta\Phi_{AB}^{ref} = +r_0\frac{eE_0}{\hbar\omega}\left[\frac{sin(\alpha_{THz} + \alpha_e)}{1 + \beta cos(\alpha_{THz} + \alpha_e)}\right] cos(\omega\Delta t + \varphi_r)(sin(\alpha_e) - \beta sin(\alpha_{THz}))\Delta x \tag{6.10}$$

$$\Delta\Phi_{AB}^{trans} = -t_0\frac{eE_0}{\hbar\omega}\left[\frac{sin(\alpha_{THz} - \alpha_e)}{1 - \beta cos(\alpha_{THz} - \alpha_e)}\right] cos(\omega\Delta t + \varphi_t)(sin(\alpha_e) - \beta sin(\alpha_{THz}))\Delta x \tag{6.11}$$

In general, these THz-induced phase shifts are linear functions of $\Delta x$ and can therefore lead to global beam deflections, as observed in experiments with metals or dielectrics [130,165]. Interestingly, for specific combinations of angles fulfilling the condition of velocity matching, defined by Eq. (3.2), all three contributions to the overall phase shifts and the corresponding global deflections vanish independently of $\Delta t$ and the beam splitting properties of the interface. For these specific geometrical configurations with matched velocity components along the interface (see Fig. 6.2 (c)), the entire spatially-extended electron beam experiences the same physics and consequently relative phase shifts between parallel electron trajectories do not arise. In particular for the experiment's collinear geometry, with co-propagating electrons and an excitation wave vector at normal incidence ($\alpha_e = \alpha_{THz} = 0$), neither relative phase shifts nor global deflections arise from this electromagnetic wave background.

This conclusion for velocity-matched settings [67] holds as long as the optical response of the ultrathin material under investigation does not deviate from the behavior of conventional materials as far as the equality of the angles of incidence, reflection and transmission is concerned. For more sophisticated materials than our wavy sample, however, an intentional design of nanoscale building blocks to generate exotic reflection or transmission properties [166,167] may indeed cause some deflection. Such specific designs with extraordinary combinations of angles involved, for which the condition of velocity matching can no longer be fulfilled simultaneously for all three contributions to the overall phase shift of the electron wave function, require a reassessment of Eqs. (6.9) to (6.11) in order to determine any non-vanishing beam deflections and thereby the most suitable experimental configuration.

In summary, the effective beam-splitting aspects of an ultrathin nanostructured material exposed to collimated, long-wavelength electromagnetic radiation can at most lead to global beam deflections while the Bragg spot intensities remain insensitive to such macroscopic interactions. For our applied collinear geometry at normal incidence, any such macroscopic effects cancel out completely, even if potential quantum contributions are considered. The experimentally-observed global Bragg pattern motion results exclusively from mesoscopic resonances of the supporting structures (see Chapter 3).

## 6.3 Structure-Specific Sub-Unit-Cell Dynamics

Equipped with the presented characterization of the global beam deflections, the focus will now be placed on the nanostructure-specific, sub-unit-cell dynamics and the changes they may inflict on the time-resolved Bragg spot intensities (see Mohler at al. [67]). A thorough characterization of the initiated nanoscale dynamics and the inflicted changes on the diffraction patterns requires a quantum-mechanical approach to describe the interference of electron de Broglie waves that spread coherently over multiple unit cells. While the shape of the nanostructure itself is not altered by the optical excitation, dynamical diffraction effects may arise from the spatio-temporal quantum phases imprinted on the electron wave function as a result of the electrodynamics around the nanostructures.

Previously reported methods to simulate quantum-mechanical laser-electron interactions at nanostructures include analytical methods [168] and hybrid approaches with a Maxwell-Schrödinger framework [169]. The approach presented in this thesis (see Fig. 6.3 (a)) is based on a phase-object-approximation for exploring the THz-electron interactions on a nanoscale [67]. In analogy to the previous calculation for the plane-wave background, the derivation of the phase shifts originating from the nanoscale features is based on Eq. (6.1). On the microscopic dimensions of the unit cell, however, we obtain the time-dependent and structure-specific electromagnetic fields no longer analytically but numerically from finite-difference time-domain (FDTD) simulations. Applicable to a wide range of different nanostructure designs, FDTD approaches are grid-based differential methods for simulating complex electrodynamic systems by numerically evaluating time-dependent Maxwell's equations. To arrive at the desired phase shifts of the electron wave function via Eq. (6.1), the numerically-determined electromagnetic fields have to be transformed into the associated potential four-vector (see also Mohler et al. [67]), whose magnetic and electric components are related to the fields as follows:

$$\vec{E} = -\nabla\varphi - \frac{\partial\vec{A}}{\partial t} \qquad \text{and} \qquad \vec{B} = \nabla \times \vec{A} \tag{6.12}$$

By exploiting the collinear geometry of the experiment, for which all unit cells experience locally the same physics in space and time, the FDTD calculations can be restricted to a single unit cell with periodic boundary conditions perpendicular to the direction of propagation. Taking advantage of the gauge invariance and the vector identity $\nabla \times (\nabla \times \vec{A}) = \nabla(\nabla \cdot \vec{A}) - \nabla^2\vec{A}$, the favored Coulomb gauge $\nabla \cdot \vec{A} = 0$ maps these relations into a total of four Poisson equations, one for the electric scalar potential and one for each component of the magnetic vector potential, respectively (see Mohler et al. [67]):

$$\nabla \cdot \vec{E} = -\Delta\varphi - \frac{\partial(\nabla \cdot \vec{A})}{\partial t} = -\Delta\varphi \tag{6.13}$$

$$\nabla \times \vec{B} = \nabla(\nabla \cdot \vec{A}) - \Delta\vec{A} = -\Delta\vec{A} \tag{6.14}$$

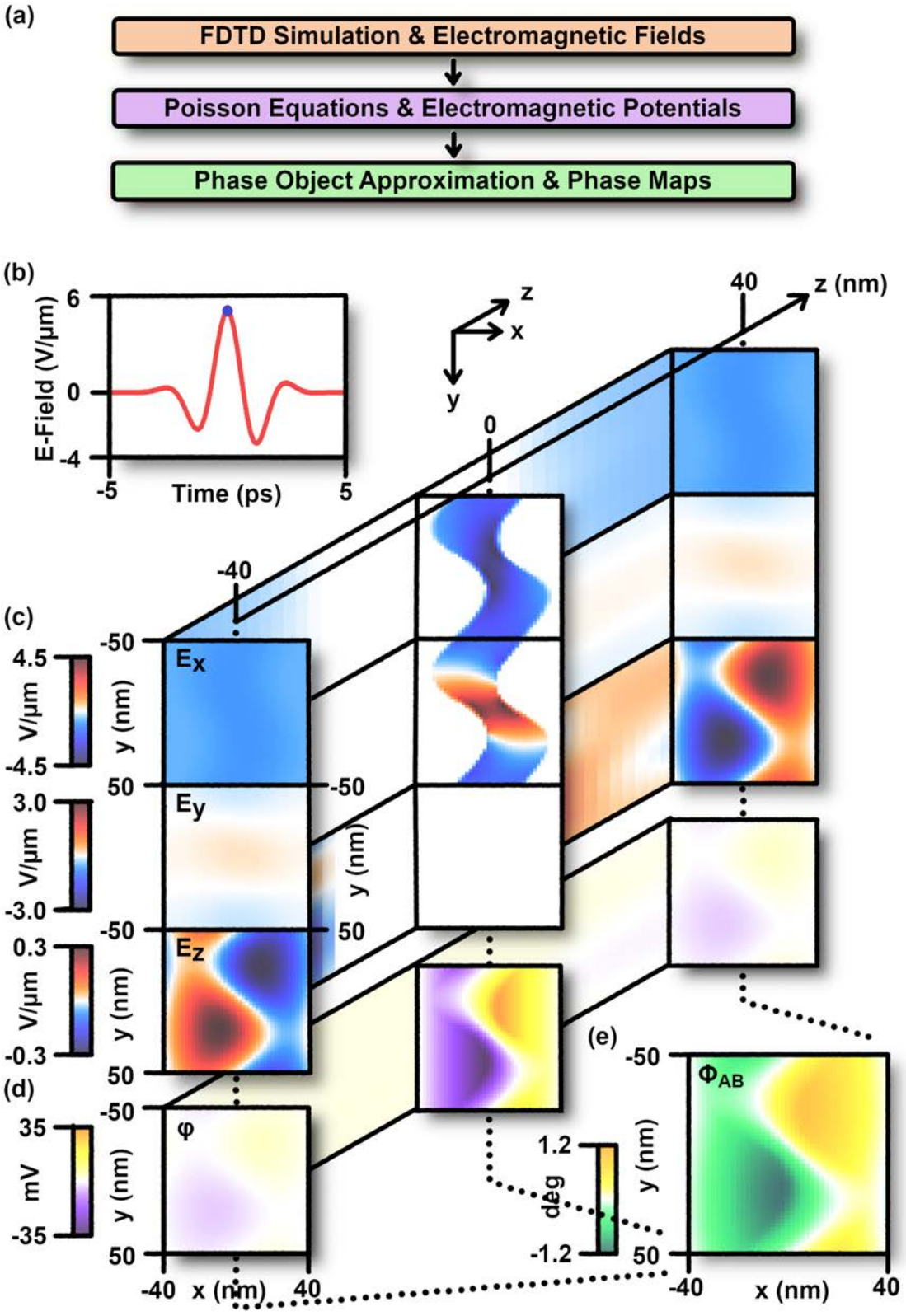


**Figure 6.3: Nanoscale electric fields and scalar potential.** **(a)** Outline of the proposed theoretical framework. **(b)** Temporal profile of the optical excitation at the position of the sample (red). Selected point in time for the displayed electric fields and scalar potential (blue dot). **(c)** 3D electric field distributions around our wavy nanostructure (close-up view along *z*), as obtained from FDTD simulations of a single unit cell with periodic boundary conditions. For saving memory, we use a wave with a frequency of 35 THz, of which the wavelength is still 100 times larger than the unit cell. In this regime, the field enhancement is wavelength independent [146]. Gold is approximated as a perfect metal. **(d)** Corresponding electric scalar potential in Coulomb gauge. **(e)** Phase map imprinted on the electron wave function as a result of the nanoscale THz-electron interaction.

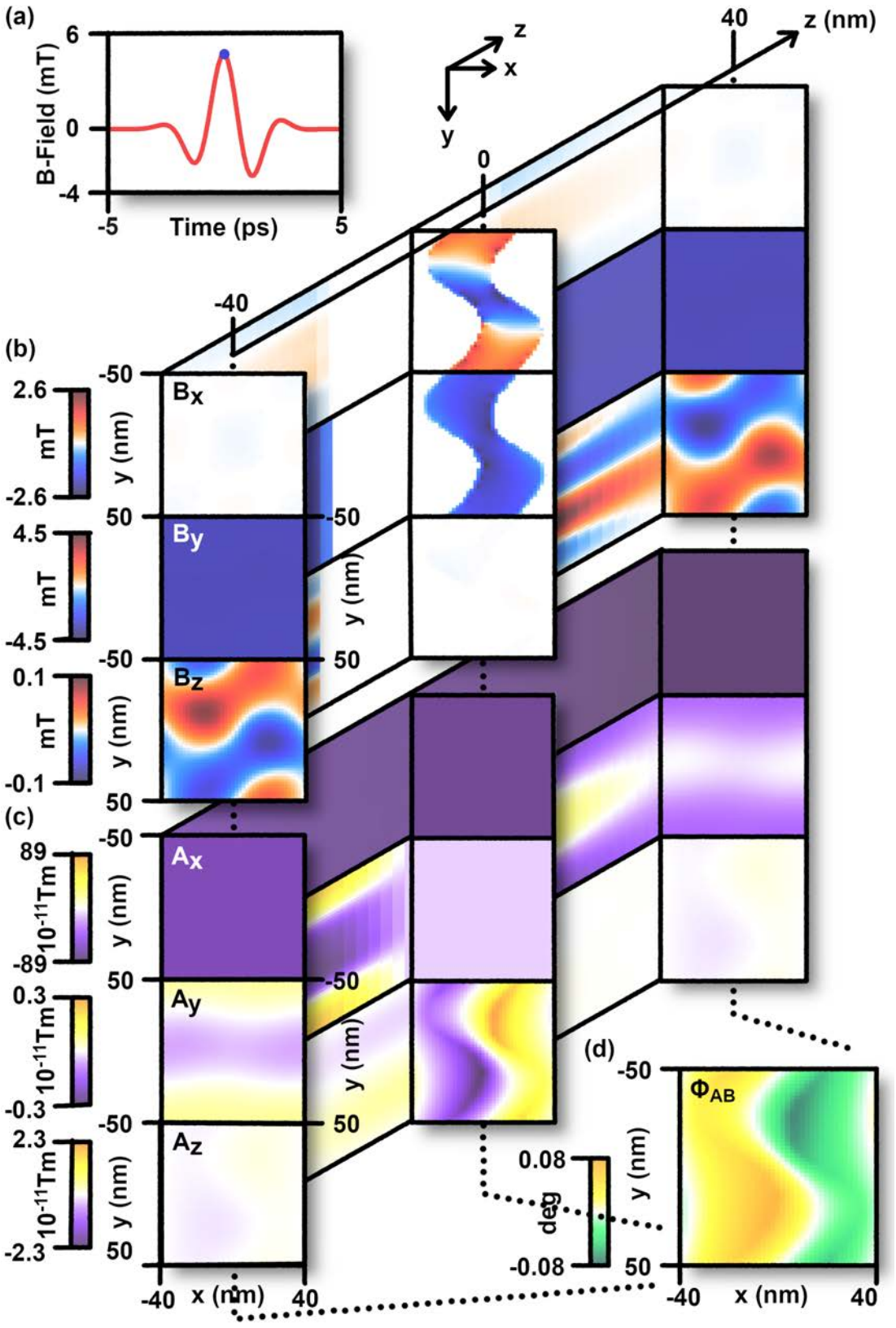


**Figure 6.4: Nanoscale magnetic fields and vector potential.** **(a)** Temporal profile of the optical excitation at the position of the sample (red). Selected point in time for the displayed magnetic fields and vector potential (blue dot). **(b)** 3D magnetic field distributions around our wavy nanostructure (close-up view along *z*), as obtained from FDTD simulations of a single unit cell with periodic boundary conditions. For saving memory, we use a wave with a frequency of 35 THz, of which the wavelength is still 100 times larger than the unit cell. Gold is approximated as a perfect metal. **(c)** Corresponding magnetic vector potential in Coulomb gauge. **(d)** Phase map imprinted on the electron wave function as a result of the nanoscale THz-electron interaction.

To obtain the time-dependent potential four-vector $A_\mu$ as a function of space and time, all four Poisson equations are solved iteratively by applying the finite difference method with periodic boundary conditions perpendicular to the direction of electron and THz propagation. The incoming THz pulse is polarized along the $x$ direction and modeled based on the cosine-like temporal profile in Fig. 5.3 (c), as retrieved from the measured global beam deflection (see Chapter 3). At the depicted instance in time (blue dot in Fig. 6.3 (b)), the electric near fields (see Fig. 6.3 (c)) point predominantly towards negative $x$ but have an additional periodic component along $y$ that arises from the wavy nature of our nanostructures (see also Mohler et al. [67]). Induced surface charges counteract the incident electric field inside the conducting material whereas field enhancement arises in the gap. For retrieval of the scalar potential in the 3D simulation volume, simple Dirichlet boundary conditions are applied along the direction of propagation since there exist no electric charges far away from the nanostructures. As a result of the THz-induced momentary charge separation, a gradient of the scalar potential emerges (see Fig. 6.3 (d)), predominantly along the polarization direction of the excitation wave. The corresponding electric fields induced inside the metal are canceled by the time derivative of the magnetic vector potential $A_x$. The retrieved scalar potential $\varphi$ provides the basis for calculating delay-dependent phase maps $\Phi_{AB}$ (see Fig. 6.3 (e)), according to Fig. 6.1 and accounting for the electric contributions.

In contrast to freely-propagating electromagnetic waves, electric and magnetic near-field components confined to sub-wavelength dimensions can also exist rather independently of each other [140]. Depending on the specific light-matter interaction under investigation, one type of near field can be more dominant than the other one, which necessitates a detailed assessment of both electric and magnetic contributions. Gold has a vanishing terahertz magnetic susceptibility, but dynamical currents almost perfectly cancel the magnetic fields inside the wavy structures (see Fig. 6.4 (b)). Consequently, the potentials and fields in our experiment cannot be produced by any electrostatic and/or magnetostatic experiment and the diffraction experiment explores a purely dynamical setting.

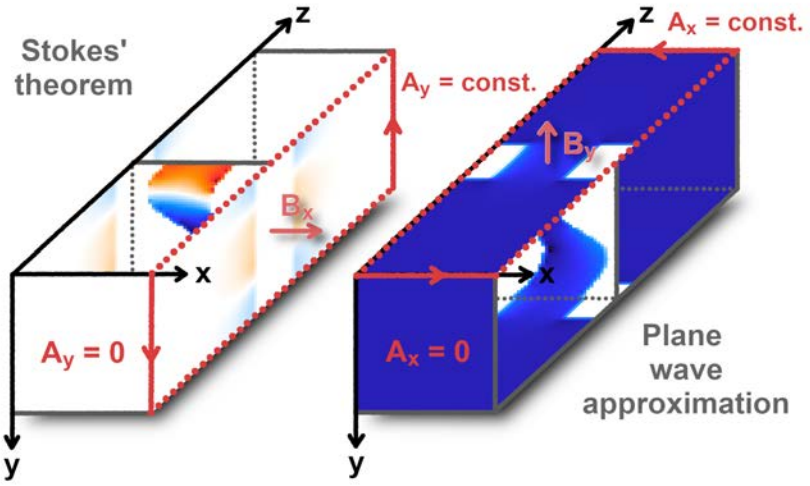


**Figure 6.5: Boundary conditions for retrieval of the vector potential as obtained from the Kelvin-Stokes theorem in combination with a plane wave approximation in the far field ($A_z = 0$).**

For retrieval of the magnetic vector potential via Eq. (6.14), the necessary boundary conditions are calculated by applying Kelvin-Stokes theorem in combination with a plane wave approximation far away from the nanostructures (see Fig. 6.5), which is compatible with our macroscopic description as a beam-splitting material (see previous paragraphs). For metamaterials, typically structured on dimensions much smaller than the excitation wavelength, the vector potential in the far field merely remains a function of the $z$ coordinate and the plane wave approach delivers a suitable approximation.

Without infringing the applied Coulomb gauge, the boundary condition at minimum $z$ can be set to zero for a time step of reference, while the application of the Kelvin-Stokes theorem serves for defining the upper boundary in the direction of propagation. According to the Kelvin-Stokes theorem, the line integral of a vector field (i.e. the vector potential) around a loop enclosing a certain surface is identical to integrating the curl of this vector field (i.e. the magnetic field) over the enclosed area. For our periodically-arranged nanostructured array, the two loops of choice (see Fig. 6.5) for determination of $A_x$ and $A_y$, respectively, follow exactly the periodic boundaries in $x$ and $y$ direction. In this way, the periodicity of the nanostructured array and its dynamics causes a cancellation of the dashed parts of the trajectories while the line integrals at minimum $z$ equal zero, owing to the vanishing vector potentials at this location. Thus, the only residual non-vanishing contributions to the two line integrals (i.e. the vector potentials at maximum $z$ times the dimension of the unit cell) allows for retrieval of the far-field boundary conditions for $A_x$ and $A_y$ from the related surface integrals over the enclosed magnetic fields. The lower boundaries for all remaining time steps $\delta t$ in the plane wave approximation can be determined from $A_{x,y} = -\int_0^{\delta t} E_{x,y} \cdot dt$. Whenever such a plane wave approximation is not applicable, the simulated region can always be chosen large enough to cover the entire optical pulse so that the vanishing far fields at the boundaries justify simple Dirichlet boundary conditions.

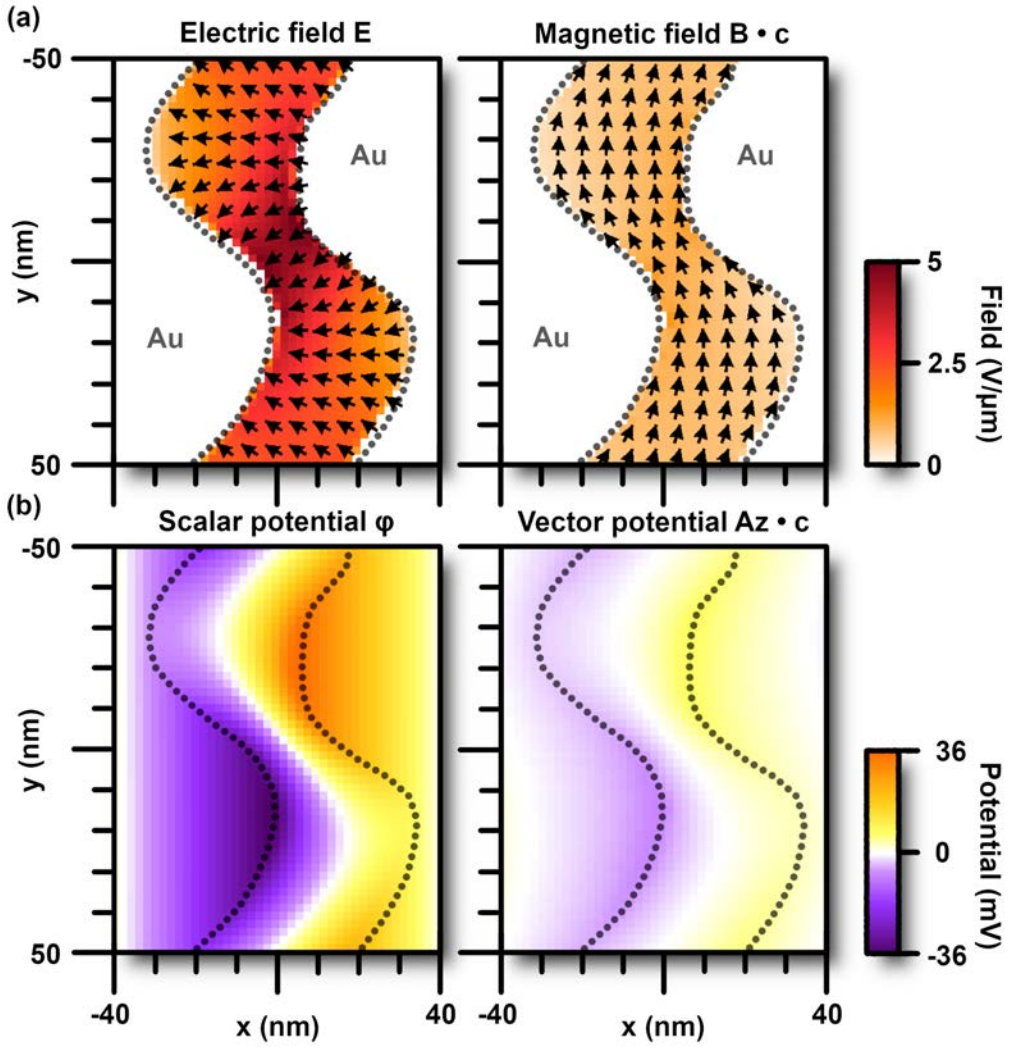


**Figure 6.6: Electromagnetic fields and potentials.** **(a)** Time-dependent electric field vectors at the example of $\Delta t = 0$ fs. **(b)** Magnetic field vectors. **(c)** Electric scalar potential. **(d)** Magnetic vector potential component along the propagation direction, all in Coulomb gauge. The speed of light is abbreviated as $c$. (Figure design inspired by Mohler et al. [67])

In summary, even conducting materials are still subject to light-induced phenomena, despite the very low penetration depth of optical radiation into metal. These light-induced phenomena include magnetic and electric near fields arising from optically-induced currents and momentary charge separations. Here, our wavy nanostructures favor electric over magnetic field enhancement. While the peak electric field enhancement amounts to a factor of ~5 in the gap where adjacent gold rods come closest (see Fig. 6.6 (a)), only minor magnetic field enhancement (see Fig. 6.6 (b)) is observed in this long-wavelength regime. This break in symmetry is transferred to the corresponding potentials (see Figs. 6.6 (c) and (d)) and electron phase shifts, whereby electrically-induced and magnetically-induced phase shifts additionally show a different dependence on the velocity of the electrons. Consequently, opposing electric and magnetic contributions do no longer entirely cancel each other, as it would be the case for global deflection effects induced by freely-propagating laser pulses or in velocity-matched settings at homogeneous interfaces (see previous paragraphs). Thus, such sub-unit-cell dynamics are expected to reveal themselves in form of dynamical changes in time-resolved diffraction patterns.

## 6.4 Sub-Excitation-Cycle and Centrosymmetry-Violating Bragg Spot Dynamics

To elucidate the impact of THz-induced collective electronic motion on Bragg spot intensities, a phase-object approximation is applied. For our electron pulses of sub-100-fs duration and electron transit times through the nanostructures' near field of $t_{\mathrm{trans}} < 0.6$ fs, the electrons capture time-frozen snapshots of the THz-excited electrodynamics. Thus, a direct link is established between the time-dependent electromagnetic potentials inside the sample and the delay-dependent phase shifts [67], imprinted on the electron wave function in dependence of the electrons' velocity and their lateral position with respect to the nanoscale building blocks. For modeling the THz-excited nanostructures, the delay-dependent phase maps, accounting for the electromagnetic interaction, are combined with a stationary absorption mask, representing the physical structures, and a Gaussian distribution for incorporating the finite coherence length of the electron beam (see Fig. 6.7 (a)). Given a velocity-matched setting, the underlying FDTD and finite difference calculations, yielding the electromagnetic fields and potentials, can be restricted to a single unit cell with periodic boundary conditions. This simplification, however, can no longer be maintained for modeling the amplitude and phase of the electron wave function, including its coherence properties, and the subsequent Fourier transform.

In diffraction, the number of unit cells employed for the Fourier transform defines the accessible spatial resolution, the coherence length of the electron beam determines the width of the diffraction peaks and the THz-induced phase shifts manifest themselves as relative intensity changes of individual Bragg spots. For illustration purposes, the THz-inflicted intensity changes are depicted as 2D diffraction patterns (see Fig. 6.7 (b)) and associated line scans (see Fig. 6.7 (c)), both illustrating dynamic intensities which oscillate back and forth between the higher-order Bragg spots during half a cycle of the optical excitation. In this way, transient asymmetries arise in the time-resolved diffraction patterns as striking features of a dynamical system, clearly violating the centrosymmetric characteristics of static diffraction patterns as the absolute square of the Fourier transform of a real-valued object [67].

The oscillations in Bragg spot intensities also show a clear correlation with the electrodynamics, induced inside the sample at the time of electron transit, as long as the electron probe pulses are reliably compressed to sufficiently sub-excitation-cycle duration. Interestingly, the position of the Bragg spots is left unaffected by these sub-unit-cell dynamics owing to the periodicity of the nanostructured array

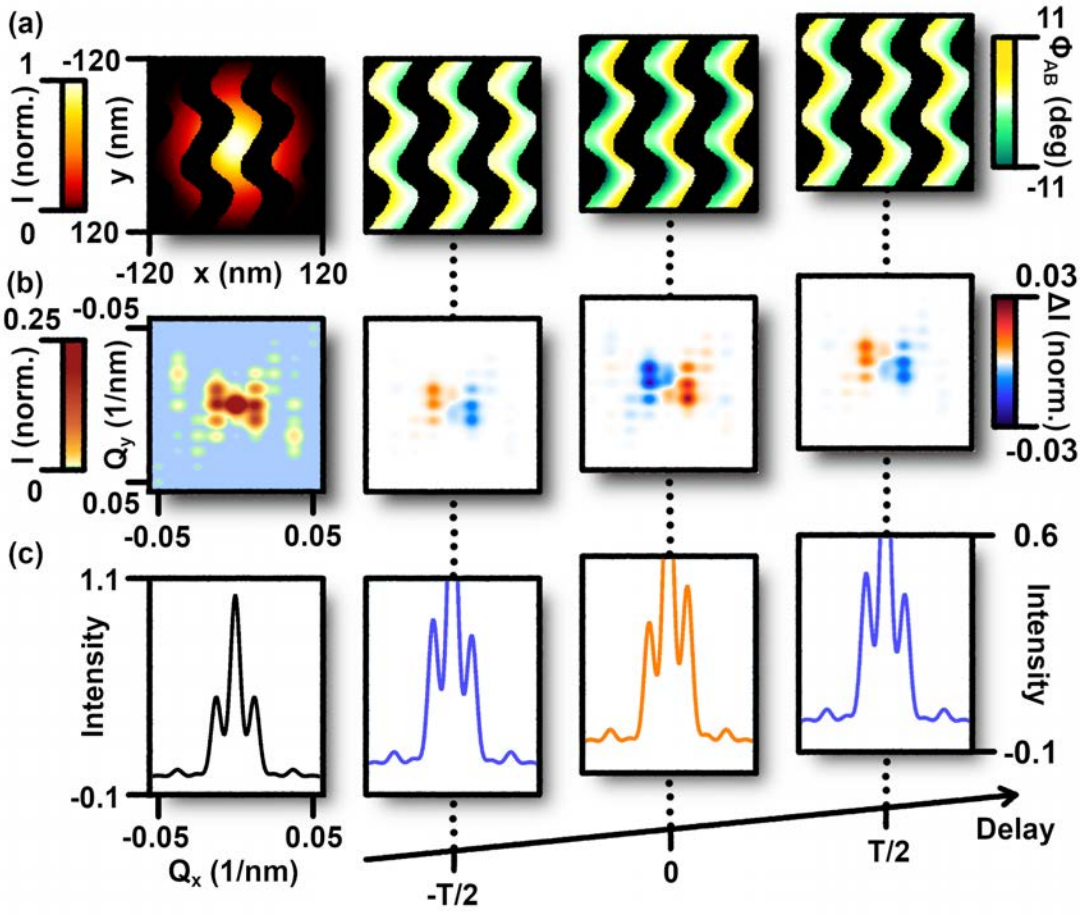


**Figure 6.7: Theoretical prediction of optically-induced electron phase shifts and sub-cycle Bragg spot dynamics.** The stationary results are depicted as reference in the very left column, while the sub-cycle dynamics, captured at three selected THz-electron time delays, are displayed on the right. **(a)** A stationary absorption mask defines the positions and shapes of the nanoscale structures while the electron-THz interaction is accounted for by an electron phase map (close-up views). For display purposes, the analyzed and depicted phase shifts result from an approximately 10 times larger field strength of the simulated incident THz radiation than experimentally applied. **(b)** 2D static diffraction pattern derived via Fourier transform and the optically-induced relative intensity changes. **(c)** Line scans, generated from the 2D data via integration along the *y* direction, visualize the relative sub-cycle intensity changes of the higher-order Bragg spots, leading to a transient asymmetry of the whole diffraction patterns in synchrony to the optical excitation. The duration of the excitation cycle is abbreviated as *T*.

and the velocity-matched configuration, for which all unit cells experience the same physics. The magnitude of the predicted dynamical intensity changes of individual Bragg spots strongly depends on the incident terahertz field strength, the polarization of the excitation and the explicit shape of the nanostructures under interrogation. Moreover, the different velocity dependence of magnetically-induced and electrically-induced electron phase shifts (see Eq. (6.1)) bears the potential to distinguish these two individual contributions from each other.

By scanning the electron-terahertz time delay, the single-cycle characteristics of the optical excitation emerge in the dynamical intensity changes of individual Bragg spots. Simulations, accounting for the combined impact of magnetic and electric contributions in the case of time-compressed electron pulses at energies of 75 keV, are depicted in Fig. 6.8 as solid lines. They reproduce the experimentally-captured Bragg spot intensities (raw data as faint dots and smoothed data as dark dots) and their evolution in synchrony to the shape of the terahertz excitation field, thereby linking the observed violation of centrosymmetry back to the excitation-induced electromagnetic potentials (see Fig. 6.7).

Only the absolute degree of asymmetry is approximately 3-5 times higher in the experiment as compared to the calculations, attributed to our neglect of non-normal wall directions, the specific refractive index of nanostructured gold, additional field enhancements from surface roughness and uncertainties in determining our structure's thickness along $z$ (see also Mohler et al. [67]).

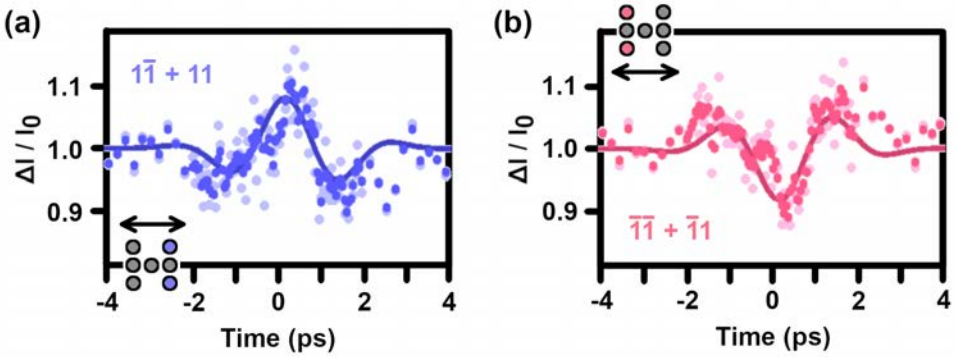


**Figure 6.8: Comparison with experimental data. (a)** Measured relative Bragg spot intensity (bright dots, raw data; blue dots, smoothed) of $1\bar{1}$ and 11 in comparison to numerical simulations (solid line) as a function of electron-terahertz delay time. **(b)** Measured relative Bragg spot intensity of $\overline{11}$ and $\bar{1}1$ (bright dots, raw data; red dots, smoothed) in comparison to numerical simulations (solid line) as a function of electron-terahertz delay time. Centrosymmetry-violating Bragg spot dynamics emerge in both experimental observations and theoretical predictions. (Figure inspired by our publication [67])

In summary, the reported experimental results and simulations establish a clear quantum-mechanical picture of electron-nanostructure interaction in the presence of dynamical electromagnetic excitation fields at frequencies approaching those of light. The observation of time-dependent Bragg spot intensities synchronous with the THz-induced electromagnetic potentials demonstrates that ultrashort few-electron pulses, if made shorter than half a cycle of the excitation period, can non-invasively capture the nanophotonic response of a nanostructured material with sub-wavelength and sub-excitation-cycle precision in space and time. By further optimizing this proof-of-concept experimental setup in terms of signal-to-noise ratio, a detailed assessment of individual Bragg spot intensities should become feasible and, supported by our presented theoretical framework, deliver two-dimensional and structure-specific information about the transient field distributions within the sample.

## 6.5 Influence of Non-Local and Local Electromagnetic Fields

A one-dimensional simplification can help to elucidate the observed dynamics in even more detail (see Fig. 6.9). To this end, we neglect our nanostructures' local curvatures and approximate them as a grid of linear wires under long-wavelength, non-resonant excitation (see also Mohler et al. [67]). The far field of the incoming terahertz pulse can be neglected because it does not affect the final diffraction pattern, neither the Bragg spot positions nor the Bragg spot intensities (see previous discussion). After subtraction of this plane-wave background, we obtain the induced electromagnetic near fields as illustrated in Figs. 6.9 (a,b). Under long-wavelength excitation, the electric and magnetic fields are approximately constant in the gaps and imprint linear phase shifts onto an incoming plane electron wave (blue lines). In a semi-classical picture, the electrons traversing the fields in the gaps are classically affected by the locally-acting Lorentz force and quantum mechanically experience spatially-dependent phase shifts of the electron wave function resulting in tilted wave fronts [161]. For an optically-excited grating structure, however, it is not enough to merely consider the fields inside the gaps to correctly predict the electromagnetically-induced phase shifts of the electron wave

function. The induced fields inside the metal structures themselves might not be directly encountered by the electrons but they still shape the corresponding potential landscape and thereby also the optically-induced electron phase shifts, which have to satisfy the principle of continuity. For this reason, continuous phase shifts over the entire extension of the electron beam are evaluated whereas the low penetration depth of the electron pulses into the metal structures is subsequently accounted for by an additional absorption mask in our applied phase-object approximation. Electrons traversing the induced fields inside the metal structures (red dashed boxes in Figs. 6.9 (a,b)) would experience wave front tilts of opposite direction in comparison to the gaps, which directly maps the periodicity of the induced near fields into periodic phase distributions. After inclusion of the structure-specific absorption mask, effective phase jumps $\Delta\Phi$ arise between the upper and lower edges of the gold rods.

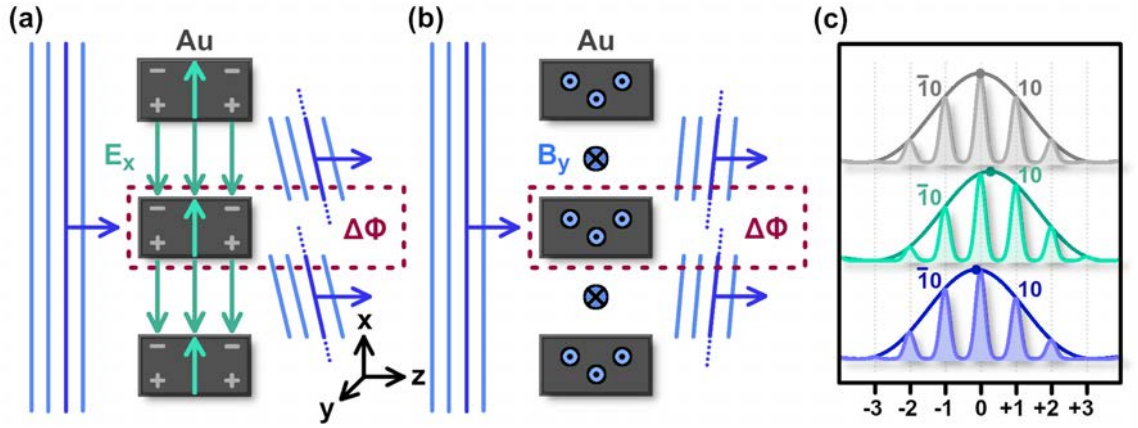


**Figure 6.9: One-dimensional model of our wavy nanostructures. (a)** Electron de Broglie waves and electric field $E_x$ in and around the gold rods after subtraction of the plane-wave background. The phase shifts $\Delta\phi$ account for the fields in the enclosed areas. **(b)** Magnetic fields $B_y$ and their weaker phase shift $\Delta\phi$ with opposite sign. **(c)** Corresponding one-dimensional diffraction patterns for no excitation (top), electric-only effects (middle) and magnetic-only contributions (bottom). Dots, centers of the diffraction envelopes. (Figure design inspired by Mohler et al. [67])

The theoretical framework developed in the course of this thesis directly accounts for local as well as non-local electromagnetic fields via their combined contributions on shaping the landscape of the electromagnetic potentials. By attributing physical consequences to electromagnetic potentials in this way, beyond being a convenient mathematical artifice, the principle of locality can be maintained [160, 161]. As a non-local alternative to the presented space-time line integrals associated with the electromagnetic potentials, the optically-induced phase shifts can also be mathematically derived via space-time area integrals of the enclosed electric and magnetic fields [160, 170, 171]:

$$\Phi_{\mathrm{AB}} = \frac{e}{\hbar}\oint A_\mu dx^\mu = -\frac{e}{2\hbar}\int F_{\mu\nu}dx^\mu \wedge dx^\nu = \frac{e}{\hbar}\int F \tag{6.15}$$

which are written in terms of the Faraday 2-form

$$F = -\frac{1}{2}F_{\mu\nu}dx^\mu \wedge dx^\nu = (E_x dx + E_y dy + E_z dz) \wedge dt + B_x dy \wedge dz + B_y dz \wedge dx + B_z dx \wedge dy \tag{6.16}$$

and the Faraday tensor $F_{\mu\nu}$ defined as follows:

$$F_{\mu\nu} = \partial_\mu A_\nu - \partial_\nu A_\mu = \begin{pmatrix} 0 & E_x/c & E_y/c & E_z/c \\ -E_x/c & 0 & -B_z & B_y \\ -E_y/c & B_z & 0 & -B_x \\ -E_z/c & -B_y & B_x & 0 \end{pmatrix} \tag{6.17}$$

An application of this framework to our 1D approximation yields opposing magnetically-induced and electrically-induced phase shifts of the electron wave function. A break in symmetry, with electric field enhancement dominating the magnetic one for our nanostructured array under long-wavelength excitation, causes net Bragg spot intensity changes to appear in diffraction (see Fig. 6.9 (c)). These violations of centrosymmetry in Bragg diffraction result from delay-dependent shifts of the envelope function with respect to stationary Bragg spot positions, complying with our observations at $\Delta t = 0$ (see Fig. 5.5), where the measured Bragg spots locate at the original position but with asymmetric intensities. In a way, the experiment at $\Delta t = 0$ mimics the unequal diffraction intensities produced by a blazed diffraction grating in optics, but here in a dynamical setting and with changes caused by purely quantum-mechanical effects according to Eq. (6.1) rather than by shaping a physical structure [67].

## 6.6 Analogy with Conventional Aharonov-Bohm Experiments

This proof-of-concept nanodiffraction study is primarily driven by the objective to establish ultrashort electron pulses as suitable probes for interferometrically revealing nanophotonic dynamics with sub-excitation-cycle time resolution since this opens up the intriguing possibility of implementing time-resolved electron interferometry of optically-excited materials at ultimate space-time resolution (i.e. picometer de Broglie wavelength and attosecond pulse duration) in a transmission electron microscope in the future. In addition to such practical applications, our experimental setting, in combination with the presented theoretical framework, further delivers an appealing toolbox for addressing rather fundamental questions of quantum mechanics, such as the principle of locality and the significance of electromagnetic potentials beyond being a convenient mathematical artifice [160, 161]. In this context, asymmetric Bragg spot intensities induced by the presence of electromagnetic potentials also emerge as key signatures of conventional Aharonov-Bohm settings that aim at identifying phase shifts resulting exclusively from non-local electromagnetic fields [160, 172]. Highlighting the significance of electromagnetic potentials for maintaining the principle of locality, Yakir Aharonov and David Bohm predicted for example the imprint of relative phase shifts on electrons traveling along trajectories that enclose the static magnetic field of a long solenoid, even without local exposure to the field itself. While such magnetostatic phase shifts have been confirmed by experiments [172, 173], discussions are still ongoing for dynamical settings [170, 174, 175], in which electric and magnetic fields are highly interlinked and potentials become a function of space and time.

Our experimental evidence of centrosymmetry-violating Bragg spot dynamics (see Fig. 6.8), arising at frequencies approaching those of light as a result of the combined impact of both local and non-local electromagnetic excitation fields (see Fig. 6.9), now indicates that electromagnetic potentials are of equally high significance in highly dynamical settings as in static ones. In the one-dimensional picture of our optically-excited nanostructured array, the transient asymmetry of Bragg spot intensities is attributed to a shift of the diffraction pattern's envelope function over stationary Bragg spot positions. In this regard, our THz-induced diffraction setting is complementary to an array of magnetic solenoids as a periodic version of the standard Aharonov-Bohm experiment. There, the electron wave obtains a ladder of phase steps [172] that, by shifting the Bragg spot positions underneath a stationary envelope function [176], results in asymmetric intensity changes comparable to our case. Thus, electron interferometry equipped with our THz-compressed electron pulses holds promising potential as a valuable technology for capturing electron phase shifts at $10^9$ times higher frequencies than accessible in previous experimental investigations of the Aharonov-Bohm effect [177, 178] and thereby for shining new light on these fundamental quantum-mechanical questions in highly dynamical settings.

# 7

# Conclusions and Outlook

*"Nothing happens until something moves."*

*– quote by Albert Einstein*

It is the spirit of this quote by Albert Einstein that guided our journey through the wide-ranging arsenal of modern imaging technologies, promoting the advance from mere static matter characterization towards the examination of a sample's dynamic behavior in light-matter interactions. As overarching feature, uniting the described experimental toolbox of different imaging modalities, specific interactions and transitions were triggered in the specimens under investigation via the well-controlled interplay with electromagnetic radiation, whereby the subsequent relaxation processes allowed for close examination of the samples' characteristic transient states [19, 67]. By harnessing such optically-induced dynamics, the information yield about the samples could substantially be increased beyond the knowledge about their mere stationary physical properties. The constant quest for novel microscopic and diffractive imaging techniques and applications, capable of studying the ultrafast electromagnetic responses of various materials with ever better precision in space and time, was illustrated in this thesis at the examples of dual-comb coherent anti-Stokes Raman scattering (CARS) microscopy (see Chapter 2) and electron diffraction of nanophotonic waveforms (see Chapter 5).

In the wake of this on-going journey towards high-precision microscopic and diffractive imaging in space and time, the previous chapters of this thesis illustrated, for example: (1) how series of time-frozen snapshots can reveal ultrafast dynamics up to light wave frequencies (see Chapters 2 and 5), (2) how pulsed laser systems can serve as powerful broadband light sources for boosting nonlinear molecular spectroscopy and microscopy (see Chapter 2), (3) how optical cycles are harnessed to time-compress electron pulses for ultrafast diffractive imaging applications (see Chapter 3), (4) how multi-keV electrons can complement photons for investigations on nanoscale dimensions (see Chapter 4) or (5) how optically-induced sub-unit-cell dynamics in nanostructured arrays relate to sub-excitation-cycle Bragg spot dynamics in time-resolved electron diffraction (see Chapters 5 and 6). Embedded in the context of capturing specific transient states of matter, a special category of repetitive techniques was invoked, namely pump-probe approaches [2, 13–17], which are predestined for examining highly-reversible processes as emerging in vibrational spectroscopy applications (see Chapter 2) or sub-excitation-cycle electrodynamics in nanophotonic materials (see Chapter 5).

The respective optically-induced dynamics under investigation primarily defined the preferred nature of probing pulses. Dual-comb CARS spectroscopy and microscopy harness exclusively femtosecond laser pulses to unveil the chemical composition of irradiated liquid and solid samples via their characteristic vibrational frequencies (see Chapter 2 and Mohler et al. [19]). To supplement purely optical pump-probe approaches, terahertz-compressed electron pulses (see our publication [32]) were invoked in Chapter 5 to probe optically-triggered dynamics in nanophotonic materials with a time window substantially shorter than one oscillation cycle of the optical excitation (see Mohler et al. [67]).

## 7.1 Dual-Comb Raman Spectroscopy and Microscopy Applications

The broadband and high-resolution CARS spectra presented in Chapter 2 clearly demonstrate that two synchronized femtosecond laser sources, operating at around 1-GHz pulse repetition frequency, can constitute the basis for a versatile Raman spectroscopy tool (see also Mohler et al. [19]), offering chemical specificity in a non-invasive and label-free manner. High-quality dual-comb CARS spectra of various liquid samples (see Fig. 7.1 (a)) were obtained with refresh rates of the interferograms in the few kHz-range and a ten-fold enhanced duty-cycle in comparison to a previous study with a 100-MHz system [17]. A heterodyne detection scheme was shown to boost the signal-to-noise ratio and thereby to mitigate the detrimental effects of the reduced pulse energies, resulting from the ten-fold increase in pulse repetition frequency. In addition, proof-of-principle investigations of microscale polystyrene beads (see Fig. 7.1 (b)), obtained with an epi-directed 100-MHz dual-comb Raman scheme, illustrated the prospect of extending dual-comb CARS from liquid phase spectroscopy to hyperspectral microscopy of solid samples, which renders the presented approach a very versatile tool for vibrational spectroscopy and microscopy applications alike. Consequently, broadband dual-comb CARS schemes are expected to meet all prerequisites to complement other Raman spectroscopy approaches on their enterprise of delivering chemical specificity in a wide range of different applications (see Fig. 7.1 (c)).

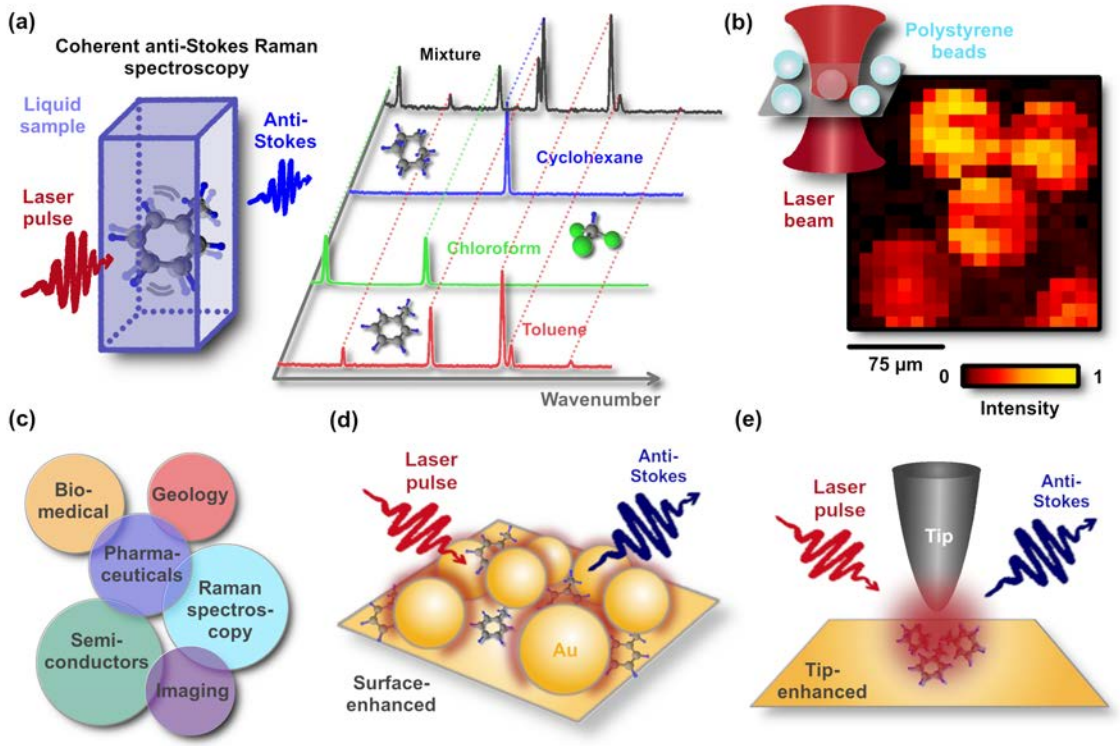


**Figure 7.1: Dual-comb Raman spectroscopy and microscopy applications.** **(a)** Demonstrated dual-comb Raman spectroscopy at 1-GHz pulse repetition frequency revealing the chemical composition of liquid samples. **(b)** Proof-of-principle demonstration of dual-comb Raman microscopy at the example of microscale polystyrene beads. **(c)** Scope of Raman spectroscopy applications. **(d)** Concept of surface-enhanced coherent anti-Stokes Raman scattering (CARS). **(e)** Concept of tip-enhanced CARS.

Offering non-destructive analysis of chemical structures via molecular fingerprinting (see Fig. 7.1 (a)) as well as spectroscopic imaging on microscopic length scales (see Fig. 7.1 (b)), the versatile and convenient usage of Raman measurements covers an extensive scope of intriguing application areas ranging from biomedical imaging over mineral identification in geology all the way to quality assessment of semiconductors (see Fig. 7.1 (c) and [179]). While many of these intriguing possibilities yet remain

to be explored for the specific technologies of dual-comb CARS spectroscopy and microscopy in the future, others have already been tackled in the meantime. After our first successful demonstration of dual-comb Raman spectroscopy at 1-GHz laser repetition frequency in 2017 [19], subsequent advances in the instrumental design and application regime of dual-comb Raman spectrometers included the implementations of a high-throughput label-free particle analyzer in 2018 [106], of surface-enhanced Raman spectroscopy (SERS) in 2018 [107] and of a sophisticated scheme for further enhancing the duty-cycle by rapidly adjusting the cavity length of one of the two frequency combs in 2020 [180]. In particular, the successful demonstration of surface-enhanced Raman spectroscopy [107] (concept depicted in Fig. 7.1 (d)) holds promising potential for applying the dual-comb scheme in the context of high-precision imaging, since the related technique of tip-enhanced Raman spectroscopy [84] (concept depicted in Fig. 7.1 (e)) unites a substantial boost in sensitivity with nanoscale spatial resolution.

As the interaction of light and matter on nanoscale dimensions and the engineering of novel nanophotonic materials [70, 72, 140, 149, 150] evolved into topics of quickly increasing scientific interest and technological relevance, the demand for suitable technologies, capable of reliably investigating the properties of metallic nanostructures and their characteristic nanoscale confinement of electromagnetic waves, arose. Even though near-field methods, such as tip-enhanced Raman spectroscopy, can surpass the diffraction limit of light by confining the region of interaction to nanoscale dimensions, electron microscopes, owing to the ultrashort de Broglie wavelength [48], are capable of exceeding the resolution accessible in optical microscopy by far [4, 5]. Moreover, the well-defined interaction of nanoscale electromagnetic fields with the elementary charge of free electrons in a microscopy or diffractive imaging setting can serve as a probing method that is non-invasive, not entangled with the excitation and does not distort the near fields and dynamics inside the structures [67].

## 7.2 Electron Nanodiffraction with THz-Compressed Electron Pulses

Collective electronic motion in nanophotonic materials is typically triggered in a highly reversible manner on time scales faster than a single cycle of light, rendering field-sensitive analysis tools indispensable in addition to the required nanoscale spatial precision. For this reason, the constant flux of free electrons in standard electron microscopy and diffractive imaging settings had to be replaced in this thesis by trains of time-compressed electron pulses with sub-excitation-cycle duration in order to investigate optically-induced electrodynamics in nanomaterials from a fundamental perspective. Sub-100-fs electron probe pulses were reliably generated at the position of the sample via the preceded interaction of free electrons with single-cycle terahertz (THz) pulses at a thin metal film (details in Chapter 3 and in our publication [32]). In addition, multiple experimental challenges had to be tackled as a result of the applied electron energies of 75 keV, which facilitate efficient electron pulse compression but are also untypically high for small-angle electron nanodiffraction experiments [51].

In our unusual regime with THz-compressed few-electron pulses probing nanostructured materials (see also Mohler et al. [67]), diffraction angles are very tiny, long-term stability is required for achieving a sufficiently high signal-to-noise ratio, the partial coherence of the electron beam imposes substantial constraints on the visibility of the diffraction pattern and the compensation for stray magnetic fields becomes indispensable (see Chapter 4). For these reasons, our time-compressed electron probe pulses were first applied in a static diffraction setting (see Fig. 4.5) in order to assess the quality of the sample's nanoscale architecture, to evaluate the achievable signal-to-noise ratio and to obtain a reliable reference for identifying dynamical changes in the subsequent time-resolved study. Equipped with the static diffraction results presented in Chapter 4, the first application of THz-compressed electron pulses in a

pump-probe electron diffraction scheme was subsequently reported and free electrons were established as suitable probes for non-invasively revealing electrodynamics in nanophotonic materials (see Fig. 7.2 (a) and refer to Chapter 5 for details). Here, the initiated sub-excitation-cycle electrodynamics in a 2D THz-excited nanostructured array became evident from the observation of centrosymmetry-violating Bragg diffraction in synchrony to the electromagnetic near-field oscillations.

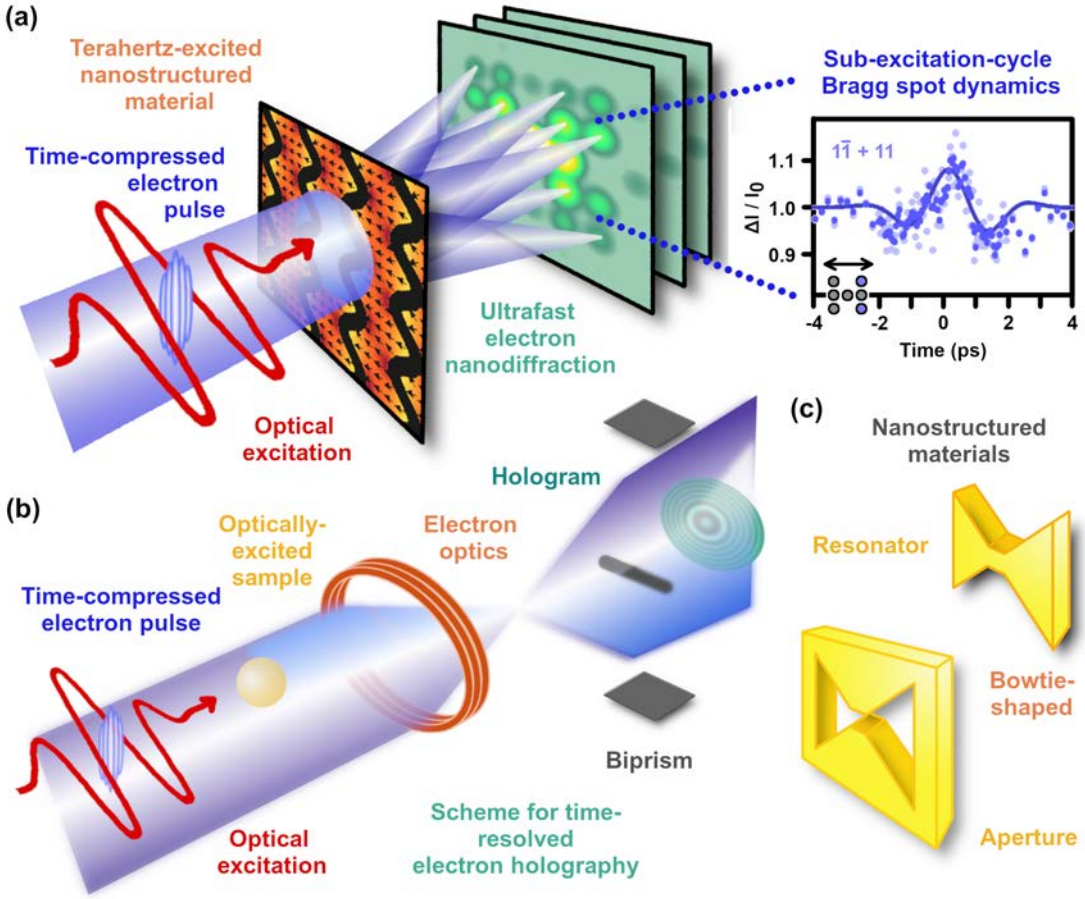


**Figure 7.2: Investigations of nanophotonic materials via THz-compressed electron pulses.** **(a)** Ultrafast electron nanodiffraction and sub-excitation-cycle Bragg spot dynamics (figure design inspired by Mohler et al. [67]). **(b)** Proposed scheme for time-resolved electron holography applications. **(c)** Nanophotonic materials with interesting optical responses for investigating Babinet's principle.

The reported space-time phase integrals (see Chapter 6) provide a simple yet all-embracing framework for tracing the measured sub-excitation-cycle Bragg spot dynamics back to quantum-mechanical phase shifts of the electron wave function and the THz-induced structure-specific electromagnetic potentials. In combination, our experimental and theoretical results imply that the functionality of nanophotonic and optical processes can be revealed in a distortion-free manner via electron-interferometric techniques, such as diffractive imaging and ultrafast holography (concept see Fig. 7.2 (b)), on the basis of the optical field cycles in space and time. For this purpose, usual optical or scanning probes can be replaced with free-space beam electrons at sub-nanometer de Broglie wavelength. Our experimental and theoretical concepts are widely applicable, independently of the explicit shape of the nanoscale architecture. When elucidating the prospect of future experiments, the developed theoretical framework can serve as a valuable tool for predicting the expected electron-holographic effects of almost any light-nanostructure interaction in all dimensions of space and time [67].

## 7.3 Nanophotonic Materials and Babinet's Principle

Such theoretical frameworks can considerably guide the development process of novel flat and lightweight nanophotonic materials with extraordinary optical responses. The required compliance with symmetry constraints additionally allows for the identification of the most relevant parameters and consequently for a valuable reduction in the number of design variables, which have to be addressed during the optimization procedure. For optically-thin materials exhibiting close to perfect conductivity, the dual behavior of complementary metallic nanostructures, as described by Babinet's principle [181,182], can be exploited for this purpose. For our presented concept of optically-induced electron nanodiffraction, Babinet's principle even has a two-folded impact on the time-resolved diffraction data by linking both the static diffraction patterns as well as the electromagnetic near fields of complementary structures. The insights delivered by Babinet's principle are illustrated in the following at the example of a bowtie-shaped aperture in a thin metal foil (see Fig. 7.3) and its complementary metallic resonator (see Fig. 7.4) under illumination with complementary electromagnetic fields.

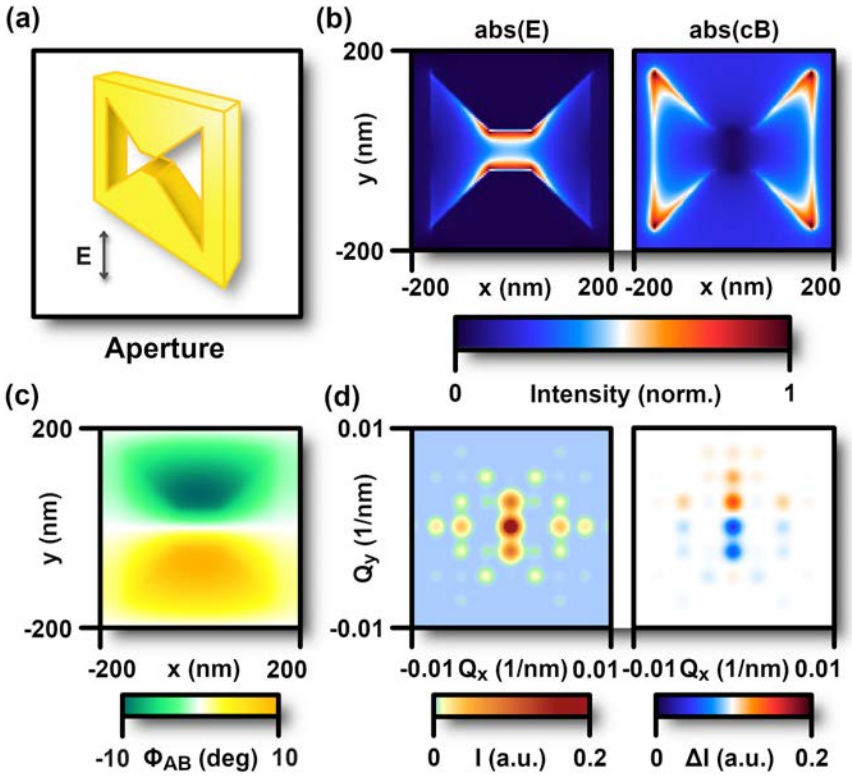


**Figure 7.3: Babinet's principle at the example of a 2D nanostructured array comprising bowtie-shaped apertures.** **(a)** Bowtie-shaped apertures in a conducting 20-nm-thin Au film, which is supported by a SiN membrane of 50 nm in thickness. **(b)** Predicted electric and magnetic near-field distributions under resonant excitation. For display purposes, the colormap is adapted to the normalized values of electric and magnetic fields, respectively. **(c)** Corresponding overall phase map imprinted on the electron wave function. **(d)** Static electron diffraction pattern and optically-induced changes in Bragg spot intensities.

By comparing the static electron diffraction patterns of these two complementary structures (see left panel in Fig. 7.3 (d) versus Fig. 7.4 (d)) it becomes obvious that they are mainly identical apart from their zero-order Bragg spot intensities, which reflect the respective surface ratios of transparent versus metallic regions. An intuitive explanation for the equality of the higher-order Bragg spot intensities for complementary structures can be derived from the valuable insight that the sum of the two interference patterns has to reproduce the undisturbed beam. This implies that any diffracted components need to be of identical amplitudes and opposite phases in order to deliver the required

cancellation [183]. Thus, experimental assessment of the diffraction pattern of a nanostructured array directly allows for predicting the characteristic Bragg spot intensities of its complementary analogue.

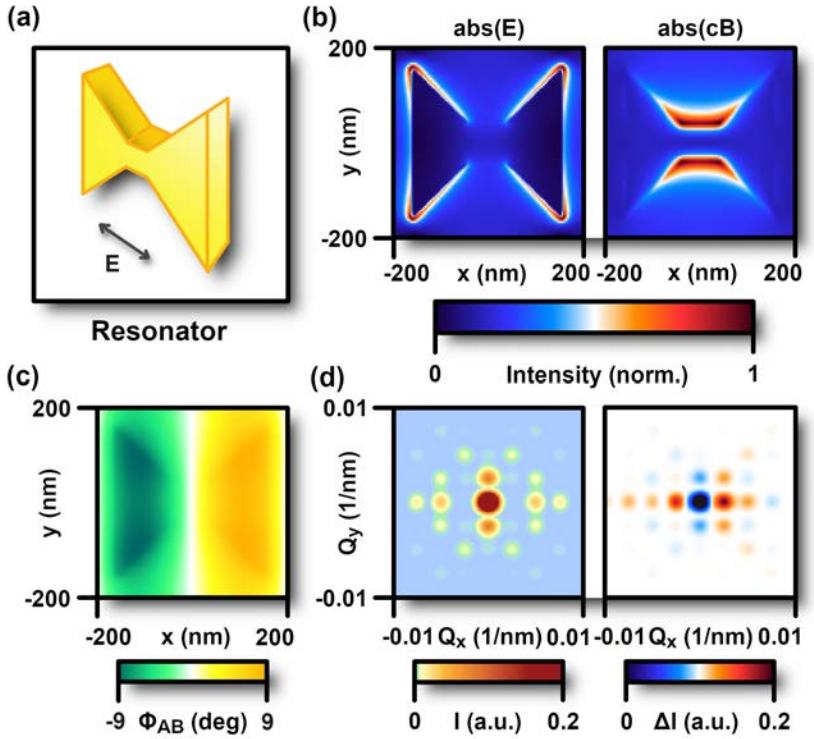


**Figure 7.4: Babinet's principle at the example of a 2D nanostructured array comprising bowtie-shaped resonators.** **(a)** Bowtie-shaped resonators (20 nm in thickness) deposited on a SiN membrane of 50 nm in thickness. **(b)** Predicted electric and magnetic near-field distributions under resonant excitation. For display purposes, the colormap is adapted to the normalized values of electric and magnetic fields, respectively. **(c)** Overall phase map imprinted on the electron wave function. **(d)** Static electron diffraction pattern and optically-induced changes in Bragg spot intensities (normalization identical to Fig. 7.3).

In addition to the nanoscale architecture, Babinet's principle also provides valuable information about the second component of our applied phase-object approximation, namely the nanoscale near fields. Babinet's principle applied to electromagnetism [181, 182] relates electric and magnetic near fields in complementary nanostructured materials. When being illuminated by complementary waves, similar features are expected to arise for our bowtie-shaped resonators and their inverse analogues, however with interchanged electric and magnetic field distributions (Fig. 7.3 (b) versus Fig. 7.4 (b)). As discussed for the THz-based electron pulse characterization in Chapter 3, electric hot spots emerge in the center of resonantly-excited bowtie-shaped apertures (see Fig. 7.3 (b)), whereas induced currents running through the conductive bridge of bowtie-shaped antennas [182] result in complementary magnetic field enhancement (see Fig. 7.4 (b)). As electrically-induced phase shifts typically exceed the impact of magnetic fields on the electron wave function, the applicability of Babinet's principle to highly-conductive metasurfaces offers the intriguing possibility to indirectly assess the less dominant magnetic near fields by measuring the electric ones of their inverse analogues [184].

## 7.4 Fourier Transform Methods for Phase Retrieval

These optical near fields can be mapped into sub-excitation-cycle Bragg spot dynamics via our theoretical framework, which will now be complemented by outlining the inverse procedure: Spatiotemporal information about the electromagnetic fields and potentials, present in the sample at the time of

electron transit, may also be recovered from the experimentally accessible time-resolved diffraction data provided that the signal-to-noise ratio is high enough. The direct retrieval of the sample's nanoscale architecture and its electromagnetic response via an inverse Fourier transform is hindered though since only the modulus of the diffraction pattern can be measured [185] while the additionally required phase information is not delivered by typical UED experiments. When dispensing with any sophisticated schemes for experimentally detecting these Fourier phases, as applied in electron holography applications [64, 65], algorithmic phase retrieval can serve as an attractive alternative.

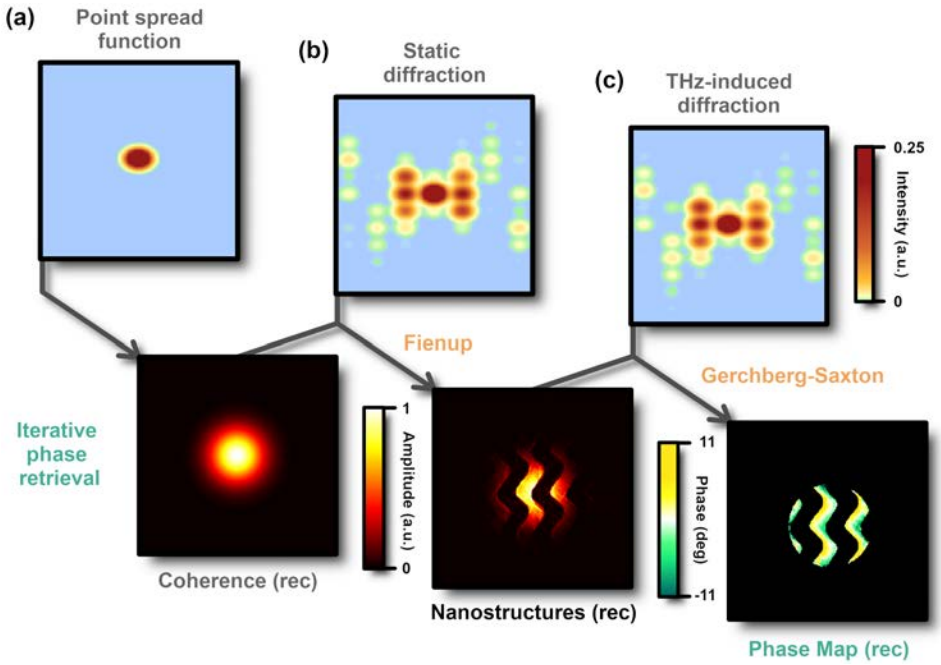


**Figure 7.5: Proposed three-step algorithm for iterative phase retrieval.** Structural and electromagnetic information can successively be extracted from a close examination of the point spread function, static electron diffraction data at high enough signal-to-noise ratio and the time-resolved Bragg spot dynamics.

In this context, a three-step process is proposed to successively retrieve the desired structural and electromagnetic information by harnessing all available experimental tools for measuring the point spread function as well as the static and optically-induced diffraction patterns: (1) The point spread function is independent of the sample's geometry but represents a measure for the coherence length of the electrons. Assuming a Gaussian-shaped point spread function, the inverse Fourier transform of the focused beam profile can yield an estimate of the coherence properties (see Fig. 7.5 (a)). (2) For retrieval of the nanoscale architecture from the static diffraction pattern (see Fig. 7.5 (b)), the approach of James R. Fienup [186] can be harnessed, which allows for reconstruction of an object (i.e. the absorption mask of our nanostructures) from the known modulus of its Fourier transform (i.e. the static electron diffraction pattern). By iteratively performing Fourier transform steps, structural information of the sample can be recovered based on all known constraints: non-negativity, periodicity, points of support limited by the coherence length and compliance with the given static diffraction pattern. (3) Finally, the optically-induced phase shift of the electron wave function can be retrieved according to the iterative Gerchberg-Saxton algorithm [187] by harnessing the recovered nanoscale architecture together with the optically-induced diffraction pattern (see Fig. 7.5 (c)). During the series of Fourier transform steps, the known magnitudes in both real and Fourier space are constantly replaced by the original input values, causing the calculated phases to gradually converge to the desired phase map.

Special care must be taken when applying these iterative phase retrieval procedures due to the potential existence of local minima, which may prohibit the successful convergence in some cases [188]. For

example, the modulus of the Fourier transform is insensitive to any translation of the object in the transverse direction. Besides, the higher-order Bragg spot intensities of a static diffraction pattern obtained from opaque structures are identical to the ones generated by holes of the same shape and size according to Babinet's principle [183], leaving the zero-order intensity as the only decisive feature. However, there exist several adaptions of the original algorithms to efficiently suppress the appearance of twin images and to avoid stagnation of the iterative processes [188]. After successful retrieval of the optically-induced electron phase shifts $\Phi_{\mathrm{AB}}$, the final remaining processing step concerns the extraction of the electromagnetic potentials. If time-resolved diffraction data is obtained for two different electron energies, electric and magnetic contributions to the overall electron phase shifts $\Phi_{\mathrm{AB}}(x,y)$ can be distinguished from each other based on their different velocity dependence:

$$\Phi_{\mathrm{AB}}(x,y) = \frac{e}{\hbar}\int_{t_1,z_1}^{t_2,z_2} A_\mu dx^\mu = \frac{e}{\hbar v_\mathrm{e}}\int_{z_1}^{z_2}\varphi dz - \frac{e}{\hbar}\int_{z_1}^{z_2} A_z dz = \frac{1}{v_\mathrm{e}}\Phi_{\mathrm{el}}(x,y) - \Phi_{\mathrm{mag}}(x,y) \tag{7.1}$$

Here, $e$ is the elementary charge, $\hbar$ is the Planck constant and $v_\mathrm{e}$ is the electron velocity. Based on the retrieved phase shifts of the electron wave function, spatially-resolved information about the scalar potential $\varphi(x,y)$ and the vector potential $A_z(x,y)$, projected along the propagation direction of the electrons, can be extracted for the optically-illuminated 2D nanostructured array under investigation:

$$\varphi(x,y) = \frac{\hbar}{e}\Phi_{\mathrm{el}}(x,y)\frac{1}{\Delta z} \qquad \text{and} \qquad A_z(x,y) = \frac{\hbar}{e}\Phi_{\mathrm{mag}}(x,y)\frac{1}{\Delta z} \tag{7.2}$$

Thus, high-quality time-resolved diffraction data promises to deliver tracking of structure-specific electromagnetic potentials in proximity of optically-excited nanostructures in space and time.

## 7.5 Perspectives

Broadband dual-comb CARS schemes at high repetition frequencies (see Mohler et al. [19]) are expected to meet all prerequisites to complement other Raman spectroscopy approaches on their enterprise of enriching optical microscopy in a label-free manner with chemical specificity for a wide range of different applications. For investigating ultrafast dynamics on nanoscale or atomic dimensions, femtosecond laser pulses can be replaced by optically-compressed electron probe pulses (see our publication [32]). Our concept of ultrafast electron nanodiffraction (see Mohler et al. [67]) is widely applicable, independently of the explicit architecture of the sample, and attosecond electron pulses [29, 108, 129, 189] will allow us in the future to investigate sub-light-cycle electrodynamics in various nanophotonic materials at wavelengths down to the visible or even ultraviolet range of the optical spectrum. The number of electrons per pulse, the transverse beam coherence and the electron pulse duration typically represent interlinked parameters in real-world applications but modern ultrafast electron microscopes and table-top diffraction apparatuses provide ample possibilities for optimization according to the intended application. In this way, time-resolved electron interferometry and microscopy can complement optical spectroscopy and microscopy regarding high-precision examination of the fastest dynamics defining our microscale, nanoscale and atomic world. The presented advance from studies of femtosecond atomic motions to sub-cycle electrodynamics opens up exciting new vistas for elucidating some of the most fundamental physics involved in light-matter interactions, such as the dynamic Aharonov-Bohm effect, as well as for characterizing the functionality of novel nanophotonic materials and devices on its ultrashort intrinsic time scales, the cycles of light.

# Bibliography


[1] C. L. Evans and X. S. Xie. Coherent anti-Stokes Raman scattering microscopy: Chemical imaging for biology and medicine. *Annual Review of Analytical Chemistry*, 1:883–909, 2008.

[2] A. H. Zewail. Four-dimensional electron microscopy. *Science*, 328:187–193, 2010.

[3] W. Wieser, B. R. Biedermann, T. Klein, C. M. Eigenwillig, and R. Huber. Multi-Megahertz OCT: High quality 3D imaging at 20 million A-scans and 4.5 GVoxels per second. *Optics Express*, 18:14685–14704, 2010.

[4] P. E. Batson, N. Dellby, and O. L. Krivanek. Sub-ångstrom resolution using aberration corrected electron optics. *Nature*, 418:617–620, 2002.

[5] W. J. Huang, J. M. Zuo, B. Jiang, K. W. Kwon, and M. Shim. Sub-ångström-resolution diffractive imaging of single nanocrystals. *Nature Physics*, 5:129–133, 2009.

[6] F. Krausz and M. I. Stockman. Attosecond metrology: From electron capture to future signal processing. *Nature Photonics*, 8:205–213, 2014.

[7] P. Baum and F. Krausz. Capturing atomic-scale carrier dynamics with electrons. *Chemical Physics Letters*, 683:57–61, 2017.

[8] B. G. Saar, C. W. Freudiger, J. Reichman, C. M. Stanley, G. R. Holtom, and X. S. Xie. Video-rate molecular imaging in vivo with stimulated Raman scattering. *Science*, 330:1368–1370, 2010.

[9] M. C. Potter, B. Wyble, C. E. Hagmann, and E. S. McCourt. Detecting meaning in RSVP at 13 ms per picture. *Attention, Perception & Psychophysics*, 76:270–279, 2014.

[10] E. Gelderblom, H. Vos, F. Mastik, T. Faez, Y. Luan, T. Kokhuis, A. van der Steen, D. Lohse, N. Jong, and M. Versluis. Brandaris 128 ultra-high-speed imaging facility: 10 years of operation, updates, and enhanced features. *Review of Scientific Instruments*, 83:103706, 2012.

[11] I. Coddington, N. Newbury, and W. Swann. Dual-comb spectroscopy. *Optica*, 3:414–426, 2016.

[12] I. Pupeza, M. Huber, M. Trubetskov, W. Schweinberger, S. A. Hussain, C. Hofer, K. Fritsch, M. Poetzlberger, L. Vamos, E. Fill, T. Amotchkina, K. V. Kepesidis, A. Apolonski, N. Karpowicz, V. Pervak, O. Pronin, F. Fleischmann, A. Azzeer, M. Žigman, and F. Krausz. Field-resolved infrared spectroscopy of biological systems. *Nature*, 577:52–59, 2020.

[13] Ahmed H. Zewail. Femtochemistry: Atomic-scale dynamics of the chemical bond. *Journal of Physical Chemistry A*, 104:5660–5694, 2000.

[14] A. Stolow, A. E. Bragg, and D. M. Neumark. Femtosecond time-resolved photoelectron spectroscopy. *Chemical Reviews*, 104:1719–1758, 2004.

[15] E. Goulielmakis, Z.-H. Loh, A. Wirth, R. Santra, N. Rohringer, V. S. Yakovlev, S. Zherebtsov, T. Pfeifer, A. M. Azzeer, M. F. Kling, S. R. Leone, and F. Krausz. Real-time observation of valence electron motion. *Nature*, 466:739–743, 2010.

[16] M. Eisele, T. L. Cocker, M. A. Huber, M. Plankl, L. Viti, D. Ercolani, L. Sorba, M. S. Vitiello, and R. Huber. Ultrafast multi-terahertz nano-spectroscopy with sub-cycle temporal resolution. *Nature Photonics*, 8:841–845, 2014.

[17] T. Ideguchi, S. Holzner, B. Bernhardt, G. Guelachvili, N. Picqué, and T. W. Hänsch. Coherent Raman spectro-imaging with laser frequency combs. *Nature*, 502:355–358, 2013.

[18] P. Baum. On the physics of ultrashort single-electron pulses for time-resolved microscopy and diffraction. *Chemical Physics*, 423:55–61, 2013.

[19] K. J. Mohler, B. J. Bohn, M. Yan, G. Mélen, T. W. Hänsch, and N. Picqué. Dual-comb coherent Raman spectroscopy with lasers of 1-GHz pulse repetition frequency. *Optics Letters*, 42:318–321, 2017.

[20] B. J. Siwick, J. R. Dwyer, R. E. Jordan, and R. J. D. Miller. Ultrafast electron optics: Propagation dynamics of femtosecond electron packets. *Journal of Applied Physics*, 92:1643–1648, 2002.

[21] T. Salditt and M. Osterhoff. X-ray focusing and optics. In *Nanoscale Photonic Imaging*, pages 71–124. Springer International Publishing, 2020.

[22] R. F. Egerton. *Physical principles of electron microscopy.* Springer US, 2005.

[23] G. M. Vanacore, I. Madan, and F. Carbone. Spatio-temporal shaping of a free-electron wave function via coherent light-electron interaction. *La Rivista del Nuovo Cimento*, 43:567–597, 2020.

[24] P. Baum and A. Zewail. Femtosecond diffraction with chirped electron pulses. *Chemical Physics Letters*, 462:14–17, 2008.

[25] A. Gliserin, A. Apolonski, F. Krausz, and P. Baum. Compression of single-electron pulses with a microwave cavity. *New Journal of Physics*, 14:073055, 2012.

[26] M. Gao, Y. Jiang, G. H. Kassier, and R. J. D. Miller. Single shot time stamping of ultrabright radio frequency compressed electron pulses. *Applied Physics Letters*, 103:033503, 2013.

[27] M. Kozák, J. McNeur, K. J. Leedle, H. Deng, N. Schönenberger, A. Ruehl, I. Hartl, J. S. Harris, R. L. Byer, and P. Hommelhoff. Optical gating and streaking of free electrons with sub-optical cycle precision. *Nature Communications*, 8:14342, 2017.

[28] P. Baum and A. H. Zewail. Attosecond electron pulses for 4D diffraction and microscopy. *PNAS*, 104:18409–18414, 2007.

[29] M. Kozák, N. Schönenberger, and P. Hommelhoff. Ponderomotive generation and detection of attosecond free-electron pulse trains. *Physical Review Letters*, 120:103203, 2018.

[30] M. V. Tsarev, D. Ehberger, and P. Baum. High-average-power, intense THz pulses from a LiNbO3 slab with silicon output coupler. *Applied Physics B*, 122:30, 2016.

[31] C. Kealhofer, W. Schneider, D. Ehberger, A. Ryabov, F. Krausz, and P. Baum. All-optical control and metrology of electron pulses. *Science*, 352:429–433, 2016.

[32] D. Ehberger, K. J. Mohler, T. Vasileiadis, R. Ernstorfer, L. Waldecker, and P. Baum. Terahertz compression of electron pulses at a planar mirror membrane. *Physical Review Applied*, 11:024034, 2019.

[33] M. P. Blakeley, S. S. Hasnain, and S. V. Antonyuk. Sub-atomic resolution X-ray crystallography and neutron crystallography: Promise, challenges and potential. *IUCrJ*, 2:464–474, 2015.

[34] F. M. Huang and N. I. Zheludev. Super-resolution without evanescent waves. *Nano Letters*, 9:1249–1254, 2009.

[35] L. Schermelleh, R. Heintzmann, and H. Leonhardt. A guide to super-resolution fluorescence microscopy. *Journal of Cell Biology*, 190:165–175, 2010.

[36] S. J. Sahl, S. W. Hell, and S. Jakobs. Fluorescence nanoscopy in cell biology. *Nature Reviews Molecular Cell Biology*, 18:685–701, 2017.

[37] E. Betzig and J. K. Trautman. Near-field optics: Microscopy, spectroscopy, and surface modification beyond the diffraction limit. *Science*, 257:189–195, 1992.

[38] M. G. L. Gustafsson. Surpassing the lateral resolution limit by a factor of two using structured illumination microscopy. *Journal of Microscopy*, 198:82–87, 2000.

[39] S. W. Hell. Nanoscopy with focused light (Nobel lecture). *Angewandte Chemie International Edition*, 54:8054–8066, 2015.

[40] E. Betzig. Single molecules, cells, and super-resolution optics (Nobel lecture). *Angewandte Chemie International Edition*, 54:8034–8053, 2015.

[41] M. J. Rust, M. Bates, and X. Zhuang. Sub-diffraction-limit imaging by stochastic optical reconstruction microscopy (STORM). *Nature Methods*, 3:793–796, 2006.

[42] F. J. Giessibl. Advances in atomic force microscopy. *Rev. Mod. Phys*, 75:949–983, 2003.

[43] P. de Boer, J. P. Hoogenboom, and B. N. G. Giepmans. Correlated light and electron microscopy: Ultrastructure lights up! *Nature Methods*, 12:503–513, 2015.

[44] L. Bragg. *The diffraction of X-rays by crystals.* Elsevier Publishing Company, 1967.

[45] C. J. Davisson and L. H. Germer. Reflection of electrons by a crystal of nickel. *PNAS*, 14:317–322, 1928.

[46] R. J. D. Miller. Femtosecond crystallography with ultrabright electrons and X-rays: Capturing chemistry in action. *Science*, 343:1108–1116, 2014.

[47] M. von Laue. *Concerning the detection of X-ray interferences.* Elsevier Publishing Company, 1967.

[48] L. de Broglie. *The wave nature of the electron.* Elsevier Publishing Company, 1929.

[49] G. P. Thomson and A. Reid. Diffraction of cathode rays by a thin film. *Nature*, 119:890–890, 1927.

[50] A. H. Zewail. 4D ultrafast electron diffraction, crystallography, and microscopy. *Annual Review of Physical Chemistry*, 57:65–103, 2006.

[51] B. McMorran, J. D. Perreault, T. A. Savas, and A. Cronin. Diffraction of 0.5keV electrons from free-standing transmission gratings. *Ultramicroscopy*, 106:356–364, 2006.

[52] S. Lahme, C. Kealhofer, F. Krausz, and P. Baum. Femtosecond single-electron diffraction. *Structural Dynamics*, 1:034303, 2014.

[53] T. E. Weirich, X. Zou, R. Ramlau, A. Simon, G. L. Cascarano, C. Giacovazzo, and S. Hovmöller. Structures of nanometre-size crystals determined from selected-area electron diffraction data. *Acta Crystallographica Section A*, 56:29–35, 2000.

[54] A. Ryabov and P. Baum. Electron microscopy of electromagnetic waveforms. *Science*, 353:374–377, 2016.

[55] T. L. Cocker, V. Jelic, M. Gupta, S. J. Molesky, J. A. J. Burgess, G. D. L. Reyes, L. V. Titova, Y. Y. Tsui, M. R. Freeman, and F. A. Hegmann. An ultrafast terahertz scanning tunnelling microscope. *Nature Photonics*, 7:620–625, 2013.

[56] V. Westphal, S. O. Rizzoli, M. A. Lauterbach, D. Kamin, R. Jahn, and S. W. Hell. Video-rate far-field optical nanoscopy dissects synaptic vesicle movement. *Science*, 320:246–249, 2008.

[57] S. A. Jones, S.-H. Shim, J. He, and X. Zhuang. Fast, three-dimensional super-resolution imaging of live cells. *Nature Methods*, 8:499–505, 2011.

[58] D. A. G. Deacon, L. R. Elias, J. M. J. Madey, G. J. Ramian, H. A. Schwettman, and T. I. Smith. First operation of a free-electron laser. *Physical Review Letters*, 38:892–894, 1977.

[59] L. Waldecker, R. Bertoni, and R. Ernstorfer. Compact femtosecond electron diffractometer with 100keV electron bunches approaching the single-electron pulse duration limit. *Journal of Applied Physics*, 117:044903, 2015.

[60] R. Bormann, S. Strauch, S. Schäfer, and C. Ropers. An ultrafast electron microscope gun driven by two-photon photoemission from a nanotip cathode. *J. Appl. Phys.*, 118:173105, 2015.

[61] G. Mourou and S. Williamson. Picosecond electron diffraction. *Applied Physics Letters*, 41:44–45, 1982.

[62] F. J. García de Abajo and V. Di Giulio. Optical excitations with electron beams: Challenges and opportunities. *ACS Photonics*, 8:945–974, 2021.

[63] B. Barwick, D. J. Flannigan, and A. H. Zewail. Photon-induced near-field electron microscopy. *Nature*, 462:902–906, 2009.

[64] H. Lichte, P. Formanek, A. Lenk, M. Linck, C. Matzeck, M. Lehmann, and P. Simon. Electron holography: Applications to materials questions. *Annual Review of Materials Research*, 37:539–588, 2007.

[65] M. R. McCartney and D. J. Smith. Electron holography: Phase imaging with nanometer resolution. *Annual Review of Materials Research*, 37:729–767, 2007.

[66] K. Müller, F. F. Krause, A. Béché, M. Schowalter, V. Galioit, S. Löffler, J. Verbeeck, J. Zweck, P. Schattschneider, and A. Rosenauer. Atomic electric fields revealed by a quantum mechanical approach to electron picodiffraction. *Nature Communications*, 5:5653, 2014.

[67] K. J. Mohler, D. Ehberger, I. Gronwald, C. Lange, R. Huber, and P. Baum. Ultrafast electron diffraction from nanophotonic waveforms via dynamical Aharonov-Bohm phases. *Science Advances*, 6:eabc8804, 2020.

[68] H. Ihee, V. A. Lobastov, U. M. Gomez, B. M. Goodson, R. Srinivasan, C.-Y. Ruan, and A. H. Zewail. Direct imaging of transient molecular structures with ultrafast diffraction. *Science*, 291:458–462, 2001.

[69] B. J. Siwick, J. R. Dwyer, R. E. Jordan, and R. J. D. Miller. An atomic-level view of melting using femtosecond electron diffraction. *Science*, 302:1382–1385, 2003.

[70] A. V. Kildishev, A. Boltasseva, and V. M. Shalaev. Planar photonics with metasurfaces. *Science*, 339, 2013.

[71] X. Ni, Z. J. Wong, M. Mrejen, Y. Wang, and X. Zhang. An ultrathin invisibility skin cloak for visible light. *Science*, 349:1310–1314, 2015.

[72] M. Khorasaninejad and F. Capasso. Metalenses: Versatile multifunctional photonic components. *Science*, 358, 2017.

[73] N. Dudovich, D. Oron, and Y. Silberberg. Single-pulse coherently controlled nonlinear Raman spectroscopy and microscopy. *Nature*, 418:512–514, 2002.

[74] C. W. Freudiger, W. Min, B. G. Saar, S. Lu, G. R. Holtom, C. He, J. C. Tsai, J. X. Kang, and X. S. Xie. Label-free biomedical imaging with high sensitivity by stimulated Raman scattering microscopy. *Science*, 322:1857–1861, 2008.

[75] C. H. Camp Jr and M. T. Cicerone. Chemically sensitive bioimaging with coherent Raman scattering. *Nature Photonics*, 9:295–305, 2015.

[76] D. Polli, V. Kumar, C. M. Valensise, M. Marangoni, and G. Cerullo. Broadband coherent Raman scattering microscopy. *Laser & Photonics Reviews*, 12:1800020, 2018.

[77] K. Hashimoto, V. R. Badarla, A. Kawai, and T. Ideguchi. Complementary vibrational spectroscopy. *Nature Communications*, 10:4411, 2019.

[78] A. Schliesser, N. Picqué, and T. W. Hänsch. Mid-infrared frequency combs. *Nature Photonics*, 6:440–449, 2012.

[79] J. Haas and B. Mizaikoff. Advances in mid-infrared spectroscopy for chemical analysis. *Annual Review of Analytical Chemistry*, 9:45–68, 2016.

[80] H. Timmers, A. Kowligy, A. Lind, F. C. Cruz, N. Nader, M. Silfies, G. Ycas, T. K. Allison, P. G. Schunemann, S. B. Papp, and S. A Diddams. Molecular fingerprinting with bright, broadband infrared frequency combs. *Optica*, 5:727–732, 2018.

[81] T. Udem, R. Holzwarth, and T. W. Hänsch. Optical frequency metrology. *Nature*, 416:233–237, 2002.

[82] P. Kukura, D. W. McCamant, and R. A. Mathies. Femtosecond stimulated Raman spectroscopy. *Annual Review of Physical Chemistry*, 58:461–488, 2007.

[83] P. L. Stiles, J. A. Dieringer, N. C. Shah, and R. P. Van Duyne. Surface-enhanced Raman spectroscopy. *Annual Review of Analytical Chemistry*, 1:601–626, 2008.

[84] R. M. Stöckle, Y. D. Suh, V. Deckert, and R. Zenobi. Nanoscale chemical analysis by tip-enhanced Raman spectroscopy. *Chemical Physics Letters*, 318:131–136, 2000.

[85] K. P. Knutsen, B. M. Messer, R. M. Onorato, and R. J. Saykally. Chirped coherent anti-Stokes Raman scattering for high spectral resolution spectroscopy and chemically selective imaging. *Journal of Physical Chemistry B*, 110:5854–5864, 2006.

[86] S. Karpf, M. Eibl, W. Wieser, T. Klein, and R. Huber. A time-encoded technique for fibre-based hyperspectral broadband stimulated Raman microscopy. *Nature Communications*, 6:6784, 2015.

[87] S. T. Cundiff and J. Ye. Colloquium: Femtosecond optical frequency combs. *Reviews of Modern Physics*, 75:325–342, 2003.

[88] C. Gohle, B. Stein, A. Schliesser, T. Udem, and T. W. Hänsch. Frequency comb Vernier spectroscopy for broadband, high-resolution, high-sensitivity absorption and dispersion spectra. *Physical Review Letters*, 99:263902, 2007.

[89] N. Picqué and T. W. Hänsch. Frequency comb spectroscopy. *Nature Photonics*, 13:146–157, 2019.

[90] N. Picqué and T. W. Hänsch. Photon-level broadband spectroscopy and interferometry with two frequency combs. *PNAS*, 117:26688, 2020.

[91] S. A. Diddams, D. J. Jones, J. Ye, S. T. Cundiff, J. L. Hall, J. K. Ranka, R. S. Windeler, R. Holzwarth, T. Udem, and T. W. Hänsch. Direct link between microwave and optical frequencies with a 300THz femtosecond laser comb. *Physical Review Letters*, 84:5102–5105, 2000.

[92] M. J. Thorpe, K. D. Moll, R. J. Jones, B. Safdi, and J. Ye. Broadband cavity ringdown spectroscopy for sensitive and rapid molecular detection. *Science*, 311:1595–1599, 2006.

[93] S. A. Diddams, L. Hollberg, and V. Mbele. Molecular fingerprinting with the resolved modes of a femtosecond laser frequency comb. *Nature*, 445:627–630, 2007.

[94] J. Mandon, G. Guelachvili, and N. Picqué. Fourier transform spectroscopy with a laser frequency comb. *Nature Photonics*, 3:99–102, 2009.

[95] F. Keilmann, C. Gohle, and R. Holzwarth. Time-domain mid-infrared frequency-comb spectrometer. *Optics Letters*, 29:1542–1544, 2004.

[96] B. Bernhardt, A. Ozawa, P. Jacquet, M. Jacquey, Y. Kobayashi, T. Udem, R. Holzwarth, G. Guelachvili, T. W. Hänsch, and N. Picqué. Cavity-enhanced dual-comb spectroscopy. *Nature Photonics*, 4:55–57, 2010.

[97] R. B. Jin and R. Shimizu. Extended Wiener-Khinchin theorem for quantum spectral analysis. *Optica*, 5:93–98, 2018.

[98] M. Cui, M. Joffre, J. Skodack, and J. P. Ogilvie. Interferometric Fourier transform coherent anti-Stokes Raman scattering. *Optics Express*, 14:8448–8458, 2006.

[99] K. Hashimoto, M. Takahashi, T. Ideguchi, and K. Goda. Broadband coherent Raman spectroscopy running at 24,000 spectra per second. *Scientific Reports*, 6:21036, 2016.

[100] A. Laubereau, D. von der Linde, and W. Kaiser. Direct measurement of the vibrational lifetimes of molecules in liquids. *Physical Review Letters*, 28:1162–1165, 1972.

[101] M. Greve, B. Bodermann, H. R. Telle, P. Baum, and E. Riedle. High-contrast chemical imaging with gated heterodyne coherent anti-Stokes Raman scattering microscopy. *Applied Physics B*, 81:875–879, 2005.

[102] T. H. S. Bican, H. W. Schrötter, and V. M. Grošev. The Raman spectrum of toluene vapour. *Journal of Raman Spectroscopy*, 26:787–790, 1995.

[103] E. O. Potma, C. L. Evans, and X. S. Xie. Heterodyne coherent anti-Stokes Raman scattering (CARS) imaging. *Optics Letters*, 31:241–243, 2006.

[104] K. Kim and W. T. King. Infrared intensities in chloroforma. *The Journal of Chemical Physics*, 80:978–982, 1984.

[105] K. B. Wiberg and A. Shrake. A vibrational study of cyclohexane and some of its isotopic derivatives — I: Raman and infrared spectra and assignments of cyclohexaae and cyclohexane-d12. *Spectrochimica Acta Part A: Molecular Spectroscopy*, 27:1139–1151, 1971.

[106] T. Ideguchi, T. Nakamura, S. Takizawa, M. Tamamitsu, S. Lee, K. Hiramatsu, V. Ramaiah-Badarla, J.-w. Park, Y. Kasai, T. Hayakawa, S. Sakuma, F. Arai, and K. Goda. Microfluidic single-particle chemical analyzer with dual-comb coherent Raman spectroscopy. *Optics Letters*, 43:4057–4060, 2018.

[107] M. Yan, L. Zhang, Q. Hao, X. Shen, X. Qian, H. Chen, X. Ren, and H. Zeng. Surface-enhanced dual-comb coherent Raman spectroscopy with nanoporous gold films. *Laser & Photonics Reviews*, 12:1800096, 2018.

[108] Y. Morimoto and P. Baum. Diffraction and microscopy with attosecond electron pulse trains. *Nature Physics*, 14:252–256, 2018.

[109] M. Knoll and E. Ruska. Das Elektronenmikroskop. *Zeitschrift für Physik*, 78:318–339, 1932.

[110] W. Gao, C. Addiego, H. Wang, X. Yan, Y. Hou, D. Ji, C. Heikes, Y. Zhang, L. Li, H. Huyan, T. Blum, T. Aoki, Y. Nie, D. G. Schlom, R. Wu, and X. Pan. Real-space charge-density imaging with sub-ångström resolution by four-dimensional electron microscopy. *Nature*, 575:480–484, 2019.

[111] M. Aidelsburger, F. O. Kirchner, F. Krausz, and P. Baum. Single-electron pulses for ultrafast diffraction. *PNAS*, 107:19714–19719, 2010.

[112] H. Busch. Über die Wirkungsweise der Konzentrierungsspule bei der Braunschen Röhre. *Archiv für Elektrotechnik*, 18:583–594, 1927.

[113] D. Kreier, D. Sabonis, and P. Baum. Alignment of magnetic solenoid lenses for minimizing temporal distortions. *Journal of Optics*, 16:075201, 2014.

[114] S. A. Hilbert, C. Uiterwaal, B. Barwick, H. Batelaan, and A. H. Zewail. Temporal lenses for attosecond and femtosecond electron pulses. *PNAS*, 106:10558–10563, 2009.

[115] M. T. Hassan, J. S. Baskin, B. Liao, and A. H. Zewail. High-temporal-resolution electron microscopy for imaging ultrafast electron dynamics. *Nature Photonics*, 11:425–430, 2017.

[116] A. Gahlmann, S. T. Park, and A. H. Zewail. Ultrashort electron pulses for diffraction, crystallography and microscopy: Theoretical and experimental resolutions. *Physical Chemistry Chemical Physics*, 10:2894–2909, 2008.

[117] G. Sciaini and R. J. D. Miller. Femtosecond electron diffraction: Heralding the era of atomically resolved dynamics. *Reports on Progress in Physics*, 74:096101, 2011.

[118] A. Feist, N. Bach, N. R. da Silva, T. Danz, M. Möller, K. E. Priebe, T. Domröse, J. G. Gatzmann, S. Rost, J. Schauss, S. Strauch, R. Bormann, M. Sivis, S. Schäfer, and C. Ropers. Ultrafast transmission electron microscopy using a laser-driven field emitter: Femtosecond resolution with a high coherence electron beam. *Ultramicroscopy*, 176:63–73, 2017.

[119] T. van Oudheusden, P. L. E. M. Pasmans, S. B. van der Geer, M. J. de Loos, M. J. van der Wiel, and O. J. Luiten. Compression of subrelativistic space-charge-dominated electron bunches for single-shot femtosecond electron diffraction. *Physical Review Letters*, 105:264801, 2010.

[120] J. Hoffrogge, J. P. Stein, M. Krüger, M. Förster, J. Hammer, D. Ehberger, P. Baum, and P. Hommelhoff. Tip-based source of femtosecond electron pulses at 30 keV. *Journal of Applied Physics*, 115:094506, 2014.

[121] J. C. Williamson, M. Dantus, S. B. Kim, and A. H. Zewail. Ultrafast diffraction and molecular structure. *Chemical Physics Letters*, 196:529–534, 1992.

[122] G. H. Kassier, K. Haupt, N. Erasmus, E. G. Rohwer, H. M. von Bergmann, H. Schwoerer, S. M. M. Coelho, and F. D. Auret. A compact streak camera for 150 fs time resolved measurement of bright pulses in ultrafast electron diffraction. *Review of Scientific Instruments*, 81:105103, 2010.

[123] C. T. Hebeisen, R. Ernstorfer, M. Harb, T. Dartigalongue, R. E. Jordan, and R. J. D Miller. Femtosecond electron pulse characterization using laser ponderomotive scattering. *Optics Letters*, 31:3517–3519, 2006.

[124] R. P. Chatelain, V. R. Morrison, C. Godbout, and B. J. Siwick. Ultrafast electron diffraction with radio-frequency compressed electron pulses. *Applied Physics Letters*, 101:081901, 2012.

[125] R. Li, C. Tang, Y. Du, W. Huang, Q. Du, J. Shi, L. Yan, and X. Wang. Experimental demonstration of high quality MeV ultrafast electron diffraction. *Review of Scientific Instruments*, 80:083303, 2009.

[126] P. Musumeci, J. T. Moody, C. M. Scoby, M. S. Gutierrez, and M. Westfall. Laser-induced melting of a single crystal gold sample by time-resolved ultrafast relativistic electron diffraction. *Applied Physics Letters*, 97:063502, 2010.

[127] F. O. Kirchner, A. Gliserin, F. Krausz, and P. Baum. Laser streaking of free electrons at 25 keV. *Nature Photonics*, 8:52–57, 2014.

[128] G. M. Vanacore, I. Madan, G. Berruto, K. Wang, E. Pomarico, R. J. Lamb, D. McGrouther, I. Kaminer, B. Barwick, F. Javier García de Abajo, and F. Carbone. Attosecond coherent control of free-electron wave functions using semi-infinite light fields. *Nature Communications*, 9:2694, 2018.

[129] K. E. Priebe, C. Rathje, S. V. Yalunin, T. Hohage, A. Feist, S. Schäfer, and C. Ropers. Attosecond electron pulse trains and quantum state reconstruction in ultrafast transmission electron microscopy. *Nature Photonics*, 11:793–797, 2017.

[130] D. Ehberger, A. Ryabov, and P. Baum. Tilted electron pulses. *Physical Review Letters*, 121:094801, 2018.

[131] T. Young. The Bakerian lecture. On the theory of light and colours. *Proceedings of the Royal Society of London*, 1:63–67, 1832.

[132] A. Einstein. Über einen die Erzeugung und Verwandlung des Lichtes betreffenden heuristischen Gesichtspunkt. *Annalen der Physik*, 322:132–148, 1905.

[133] G. Möllenstedt and H. Düker. Beobachtungen und Messungen an Biprisma-Interferenzen mit Elektronenwellen. *Zeitschrift für Physik*, 145:377–397, 1956.

[134] C. Jönsson. Electron diffraction at multiple slits. *American Journal of Physics*, 42:4–11, 1974.

[135] M.A. VanHove, W. H. Weinberg, and C.-M. Chan. *Low-energy electron diffraction*. Springer-Verlag Berlin Heidelberg, 1986.

[136] D. R. Smith, J. B. Pendry, and M. C. K. Wiltshire. Metamaterials and negative refractive index. *Science*, 305:788–792, 2004.

[137] W. Withayachumnankul and D. Abbott. Metamaterials in the terahertz regime. *IEEE Photonics Journal*, 1:99–118, 2009.

[138] N. Yu and F. Capasso. Flat optics with designer metasurfaces. *Nature Materials*, 13:139–150, 2014.

[139] S. Xiao, V. P. Drachev, A. V. Kildishev, X. Ni, U. K. Chettiar, H.-K. Yuan, and V. M. Shalaev. Loss-free and active optical negative-index metamaterials. *Nature*, 466:735–738, 2010.

[140] J. Pendry. Manipulating the near field with metamaterials. *Optics & Photonics News*, 15:32–37, 2004.

[141] F. O. Kirchner, S. Lahme, F. Krausz, and P. Baum. Coherence of femtosecond single electrons exceeds biomolecular dimensions. *New Journal of Physics*, 15:063021, 2013.

[142] A.-K. Raab. Detection of single-electron wavepackets and their statistics for ultrafast electron diffraction. *Bachelor's thesis, Technische Universität München*, 2018.

[143] M. Wegener and S. Linden. Shaping optical space with metamaterials. *Physics Today*, 63:32–36, 2010.

[144] H.-T. Chen, J. F. O'Hara, A. J. Taylor, R. D. Averitt, C. Highstrete, M. Lee, and W. J. Padilla. Complementary planar terahertz metamaterials. *Optics Express*, 15:1084–1095, 2007.

[145] N. Rotenberg and L. Kuipers. Mapping nanoscale light fields. *Nature Photonics*, 8:919–926, 2014.

[146] A. Novitsky, A. M. Ivinskaya, M. Zalkovskij, R. Malureanu, P. U. Jepsen, and A. V. Lavrinenko. Non-resonant terahertz field enhancement in periodically arranged nanoslits. *Journal of Applied Physics*, 112:074318, 2012.

[147] A. F. Koenderink, A. Alù, and A. Polman. Nanophotonics: Shrinking light-based technology. *Science*, 348:516–521, 2015.

[148] L. Novotny. From near-field optics to optical antennas. *Physics Today*, 64:47–52, 2011.

[149] E. Maguid, I. Yulevich, D. Veksler, V. Kleiner, M. L. Brongersma, and E. Hasman. Photonic spin-controlled multifunctional shared-aperture antenna array. *Science*, 352:1202–1206, 2016.

[150] M. Sivis, M. Taucer, G. Vampa, K. Johnston, A. Staudte, A. Y. Naumov, D. M. Villeneuve, C. Ropers, and P. B. Corkum. Tailored semiconductors for high-harmonic optoelectronics. *Science*, 357:303–306, 2017.

[151] G. H. Yuan and N. I. Zheludev. Detecting nanometric displacements with optical ruler metrology. *Science*, 364:771–775, 2019.

[152] P. Lodahl, S. Mahmoodian, S. Stobbe, A. Rauschenbeutel, P. Schneeweiss, J. Volz, H. Pichler, and P. Zoller. Chiral quantum optics. *Nature*, 541:473–480, 2017.

[153] P. Baum, D.-S. Yang, and A. H. Zewail. 4D visualization of transitional structures in phase transformations by electron diffraction. *Science*, 318:788–792, 2007.

[154] T. L. Cocker, D. Peller, P. Yu, J. Repp, and R. Huber. Tracking the ultrafast motion of a single molecule by femtosecond orbital imaging. *Nature*, 539:263–267, 2016.

[155] A. Polman, M. Kociak, and F. J. García de Abajo. Electron-beam spectroscopy for nanophotonics. *Nature Materials*, 18:1158–1171, 2019.

[156] D. Kreier. Ultrafast single-electron diffraction at 100 keV and investigation of carbon-nanotube dynamics. *PhD thesis, Ludwig-Maximilians-Universität München*, 2015.

[157] W. Schneider, A. Ryabov, C. Lombosi, T. Metzger, Z. Major, J. A. Fülöp, and P. Baum. 800-fs, 330-µJ pulses from a 100-W regenerative Yb:YAG thin-disk amplifier at 300 kHz and THz generation in LiNbO3. *Optics Letters*, 39:6604–6607, 2014.

[158] S. Weinberg. *Lectures on quantum mechanics*. Cambridge University Press, Cambridge, 2015.

[159] Wolfgang Nolting. *Theoretical physics 6: Quantum mechanics - basics*. Springer International Publishing, 2017.

[160] Y. Aharonov and D. Bohm. Significance of electromagnetic potentials in the quantum theory. *Physical Review*, 115:485–491, 1959.

[161] H. Batelaan and A. Tonomura. The Aharonov-Bohm effects: Variations on a subtle theme. *Physics Today*, 62, 2009.

[162] M. Xu, H. P. Urbach, D. K. G. de Boer, and H. J. Cornelissen. Wire-grid diffraction gratings used as polarizing beam splitter for visible light and applied in liquid crystal on silicon. *Optics Express*, 13:2303–2320, 2005.

[163] R. Kienberger, E. Goulielmakis, M. Uiberacker, A. Baltuska, V. Yakovlev, F. Bammer, A. Scrinzi, Th. Westerwalbesloh, U. Kleineberg, U. Heinzmann, M. Drescher, and F. Krausz. Atomic transient recorder. *Nature*, 427:817–821, 2004.

[164] E. Hecht and K. Lippert. *Optik*. De Gruyter, Berlin, Boston, 2018.

[165] Y. Morimoto and P. Baum. Attosecond control of electron beams at dielectric and absorbing membranes. *Physical Review A*, 97:033815, 2018.

[166] N. Yu, P. Genevet, M. A. Kats, F. Aieta, J.-P. Tetienne, F. Capasso, and Z. Gaburro. Light propagation with phase discontinuities: Generalized laws of reflection and refraction. *Science*, 334:333–337, 2011.

[167] A. Díaz-Rubio, V. S. Asadchy, A. Elsakka, and S. A. Tretyakov. From the generalized reflection law to the realization of perfect anomalous reflectors. *Science Advances*, 3:e1602714, 2017.

[168] I. Madan, G. M. Vanacore, E. Pomarico, G. Berruto, R. J. Lamb, D. McGrouther, T. T. A. Lummen, T. Latychevskaia, F. J. García de Abajo, and F. Carbone. Holographic imaging of electromagnetic fields via electron-light quantum interference. *Science Advances*, 5:eaav8358, 2019.

[169] N. Talebi. Schrödinger electrons interacting with optical gratings: Quantum mechanical study of the inverse Smith-Purcell effect. *New Journal of Physics*, 18:123006, 2016.

[170] D. Singleton and E. C. Vagenas. The covariant, time-dependent Aharonov–Bohm effect. *Physics Letters B*, 723:241–244, 2013.

[171] M. Bright, D. Singleton, and A. Yoshida. Aharonov-Bohm phase for an electromagnetic wave background. *The European Physical Journal C*, 75:446, 2015.

[172] M. Becker, G. Guzzinati, A. Béché, J. Verbeeck, and H. Batelaan. Asymmetry and non-dispersivity in the Aharonov-Bohm effect. *Nature Communications*, 10:1700, 2019.

[173] A. Tonomura, N. Osakabe, T. Matsuda, T. Kawasaki, J. Endo, S. Yano, and H. Yamada. Evidence for Aharonov-Bohm effect with magnetic field completely shielded from electron wave. *Physical Review Letters*, 56:792–795, 1986.

[174] B. Barwick and H. Batelaan. Aharonov-Bohm phase shifts induced by laser pulses. *New Journal of Physics*, 10:083036, 2008.

[175] S. R. Choudhury and S. Mahajan. Direct calculation of time varying Aharonov-Bohm effect. *Physics Letters A*, 383:2467–2471, 2019.

[176] G. Pozzi, C. Boothroyd, A. Tavabi, E. Yucelen, R. Dunin-Borkowski, S. Frabboni, and G. C. Gazzadi. Experimental realization of the Ehrenberg-Siday thought experiment. *Applied Physics Letters*, 108:083108, 2016.

[177] L. Marton, J. A. Simpson, and J. A. Suddeth. An electron interferometer. *Review of Scientific Instruments*, 25:1099–1104, 1954.

[178] F. G. Werner and D. R. Brill. Significance of electromagnetic potentials in the quantum theory in the interpretation of electron interferometer fringe observations. *Physical Review Letters*, 4:344–347, 1960.

[179] R. S. Das and Y. K. Agrawal. Raman spectroscopy: Recent advancements, techniques and applications. *Vibrational Spectroscopy*, 57:163–176, 2011.

[180] R. Kameyama, S. Takizawa, K. Hiramatsu, and K. Goda. Dual-comb coherent Raman spectroscopy with near 100% duty cycle. *ACS Photonics*, 2020.

[181] F. Falcone, T. Lopetegi, M. A. G. Laso, J. D. Baena, J. Bonache, M. Beruete, R. Marqués, F. Martín, and M. Sorolla. Babinet principle applied to the design of metasurfaces and metamaterials. *Physical Review Letters*, 93:197401, 2004.

[182] M. Hrtoň, A. Konečná, M. Horák, T. Šikola, and V. Křápek. Plasmonic antennas with electric, magnetic and electromagnetic hot spots based on Babinet's principle. *Physical Review Applied*, 13:054045, 2020.

[183] W. Zinth and U. Zinth. *Optik. Lichtstrahlen, Wellen, Photonen.* Oldenbourg Verlag München, 2009.

[184] A. Bitzer, A. Ortner, H. Merbold, T. Feurer, and M. Walther. Terahertz near-field microscopy of complementary planar metamaterials: Babinet's principle. *Optics Express*, 19:2537–2545, 2011.

[185] J. R. Fienup. Phase retrieval algorithms: A comparison. *Applied Optics*, 21:2758–2769, 1982.

[186] J. R. Fienup. Reconstruction of an object from the modulus of its Fourier transform. *Optics Letters*, 3:27–29, 1978.

[187] R. W. Gerchberg and W. O. Saxton. A practical algorithm for the determination of phase from image and diffraction plane pictures. *Optik*, 35:237–246, 1972.

[188] J. R. Fienup and C. C. Wackerman. Phase-retrieval stagnation problems and solutions. *J. Opt. Soc. Am. A*, 3:1897–1907, 1986.

[189] S. V. Yalunin, A. Feist, and C. Ropers. Tailored high-contrast attosecond electron pulses for coherent excitation and scattering. *arXiv*, 2103.10921, 2021.

# List of Figures

# Acknowledgments

The results presented in this thesis would not have been possible without the support and encouragement of many people, whom I would like to thank in the following:

First of all, I would like to express my gratitude towards **Prof. Dr. Ferenc Krausz** for accepting me as a PhD candidate in his world-leading research group and for kindly agreeing to supervise this thesis. Thank you very much for offering me the excellent opportunity to pursue such fascinating research projects in an outstanding international research environment. Your visionary way of thinking together with your general enthusiasm about physics has always been inspiring for me.

Second, I would like to thank **Prof. Dr. Thomas Udem** for his sincere interest in my research projects and in particular for offering to review this thesis. The appreciation which you show for students at all levels of their scientific careers is truly exceptional.

As far as the presented experimental results on **dual-comb CARS spectroscopy** are concerned, I would like to gratefully acknowledge the following support:

A special thank you goes to **Prof. Dr. Theodor Hänsch** and **Dr. Nathalie Picqué** for introducing me to dual-comb spectroscopy and for kindly providing me with access to their excellent research facilities and state-of-the-art experimental equipment, constituting the valuable basis for the successful performance of the frequency-comb-based measurements. **Dr. Bernhard Bohn**, I could not have asked for a more skillful and supportive colleague than you to work with me on the two dual-comb CARS setups. **Dr. Kana Iwakuni**, it was a true pleasure to have such a kind, loyal and talented person as you in the same research group. Kana and Bernhard, thank you for a memorable time at the MPQ! **Prof. Dr. Bart Kuyken**, thank you for always willingly sharing your expertise on frequency combs and academic research in general with me. **Dr. Ming Yan**, thank you for introducing me to dual-comb Raman spectroscopy. **Dr. Zaijun Chen** and **Dr. Pei-Ling Luo**, thank you for your friendly behavior at all times. **Prof. Dr. Thomas Udem, Prof. Dr. Randolf Pohl, Dr. Simon Holzner, Dr. Arthur Hipke, Dr. Annkatrin Sommer** and **Dr. Hanieh Fattahi**, thank you very much for your warm welcome at the MPQ and all your valuable advice, which helped me to find my way around at the institute as well as to steer my PhD studies in the right direction.

Concerning the presented results on **terahertz-based electron pulse compression and electron diffraction of nanophotonic waveforms**, I would like to express my sincere gratitude towards:

First of all, my immediate adviser **Prof. Dr. Peter Baum** for entrusting me with this exciting research project, which turned out to be as fascinating and multifaceted as challenging. Thank you for sharing your general curiosity about science with me, for introducing me to the interesting realm of single electron pulses and also for letting me contribute my own ideas whenever deciding on subsequent directions of this project. **Dr. Dominik Ehberger**, thank you for many insightful scientific discussions and in particular for sharing your great knowledge about electron pulse generation and compression with me. **Dr. Andrey Ryabov**, we had started our ambitious projects roughly at the same time and I could not have wished for a better ending than succeeding simultaneously with you. Thank you for your supportive behavior at all times! **Prof. Dr. Maxim Tsarev**, our occasional scientific discussions have always been as enjoyable as insightful for me. **Ann-Kathrin Raab**, you were definitely one

of the most helpful, dedicated and talented bachelor students, who I have met so far, and you just deserve the best for your future destinations. **Sonja Tauchert** and **Johannes Thurner**, we might share the unfortunate destiny of having to graduate during the Covid-19 pandemic but there will hopefully soon be a happy ending for all three of us. Moreover, I would like to thank all current and former members of AG Baum who I had the pleasure to work with, including **Dr. Mikhail Volkov, Dr. Yuya Morimoto, Dr. Bo-Han Chen, David Nabben** and **Eruthuparna Ramachandran**.

Additionally, I would like to thank our scientific collaborators. Thank you **Dr. Ralph Ernstorfer, Dr. Lutz Waldecker** and **Dr. Thomas Vasileiadis** in Berlin for sharing your sophisticated electron source design with us. Moreover, my special thanks go to **Prof. Dr. Rupert Huber, Imke Gronwald** and **Dr. Christoph Lange** at the university of Regensburg for their truly dedicated work on manufacturing and optimizing the wavy nanostructures for our electron diffraction experiment. Thank you **Dr. Alexander Apolonskiy** for kindly providing the laboratory space for setting up the optical diffraction setup. Besides, all these challenging research activities would not have been possible without the reliable support from the **mechanical workshop lead by Rolf Oehm** as well as **administrative assistance by Klaus Franke**. Furthermore, I would like to thank everyone who contributed to the pleasant working atmosphere on the second floor of the LMU building, in particular **Christina, Theresa, Gaia, Cristina, Tobias, Maxi, Stephan, Philipp** and **Marcel**.

During my PhD studies I further benefited a lot from the **excellent training**, which I had been very lucky to receive as a bachelor and master student: My sincere thanks in this regard go to **Prof. Dr. Robert Huber** and his outstanding team, including **Dr. Thomas Klein, Dr. Wolfgang Wieser, Dr. Matthias Eibl** and **Prof. Dr. Sebastian Karpf**, who did not only most willingly share their great scientific expertise with me but first and foremost provided me with an inspiring working atmosphere where young students can feel highly encouraged, appreciated and trusted. **Prof. James G. Fujimoto**, the research experience in your biomedical imaging group at the Massachusetts Institute of Technology (Cambridge/USA) with my very first scientific publications and conference contributions will always remain one of my most memorable experiences in academia. Thank you very much to all of you for your kind support and career advice over many years!

Last but not least, I would like to thank **my parents, my sister Karolin, my aunt Mary, my cousin Miriam, my cousin Philip, my extended family** as well as **my closest friends**, who might not have contributed that much scientifically to this work but whose emotional support cannot be valued high enough. **Elisabeth, Katharina, Melanie, Katrin, Kathrin, Victoria, Judith, Laura, Anne** and my little friend **Maja**, our long-term friendship has enriched my life in so many different ways. Thank you for your constant interest in my research activities even though most of you have never signed up for this roller-coaster life of PhD students yourselves!

# Data Archiving

The experimental raw data, evaluation files, and original figures of this thesis are stored on the Data Archive Server of the Laboratory for Attosecond Physics at the Max Planck Institute of Quantum Optics:

**/afs/ipp-garching.mpg.de/mpq/lap/publication_archive**

Raw data of all figures as well as detailed information about the performed data processing are stored relative to this root folder at:

**/Theses/2021/Mohler, Kathrin (PhD)**

Here, the content is organized according to the chapters of this thesis with separate subfolders for each of the individual figures.